Ludwig-Maximilians-University of Munich
Department of Physics
Elementary Particle Physics

Master Thesis

Development of STRAW-b: Strings for Absorption length in Water for Future Neutrino Telescope in Deep Pacific Ocean

Ruohan Li

12.October 2020

Ludwig-Maximilians-Universität München

Fakulität für Physik

Elementarteilchenphysik

Masterarbeit

Entwicklung von STRAW-b: Strings für die Absorptionslänge in Wasser für ein zukünftiges Neutrino-Teleskop im tiefen Pazifik

Ruohan Li

12.Oktober 2020

Supervisor: Prof.Dr. Elisa Resconi (TUM)
Supervisor: PD Dr. Alexander Mann (LMU)

Abstract

Multi-messenger astronomy observes astrophysical objects and interprets signals from "messengers" including electromagnetic radiation, cosmic rays, neutrinos, and gravitational waves, which are generated by different astrophysical processes. The field of neutrino astronomy has made especially significant advances over recent years, thanks to the properties of neutrinos — its interaction with cosmic medium is weaker compared to photons, and more detectable compared to gravitational waves.

The high-energy neutrino detection is based on an important infrastructure named large-scaled neutrinos telescope. It consists of kilometre-cubed-scale volume of a transparent medium instrumented with an array of photon-sensitive sensors. This strategy is nearly universal in large-scaled neutrinos telescope design. After the success of IceCube at the South Pole, the Pacific Ocean Neutrino Experiment (P-ONE), which aims for a more in-depth exploration of the south neutrino sky, is under design.

In this thesis, I contribute to the development of an optical sensor array which enables a new exploration of a deep-sea environment in the Northern Pacific Ocean, and its feasibility of hosting a new large-scaled neutrino telescope — STRings for Absorption length in Water (STRAW) detector and its upgrade (STRAW-b). This array, which is arranged in a specific geometric configuration to imitate P-ONE single string, is equipped with various light detectors and environment sensors and can quantify optical properties of the deep-sea water at a depth of 2.6 km in the Cascadia Basin. The focus of this experiment is to characterise the absorption and scattering properties of oceanic water, as well as background radiation from radioactive ^{40}K and bioluminescence.

After an introduction to STRAW-b geometry and devices, the thesis will enter in the details of the design, assembly, and calibration of the PMT spectrometers — a novel module in STRAW-b to characterise bioluminescent emission. The control software, which is tailored to our hardware is now functional and will be continually improved during the active service period of STRAW-b. The simulation and analysis of STRAW-b is currently in development. At the end of this thesis, the software structure and data acquisition technique are explained.

STRAW — STRAW-b's predecessor — has been operating in the Pacific Ocean since June 2018. Judging from high quality STRAW data and overall improvements on STRAW-b, we believe both experiments will lead us to a deeper understanding of Pacific Ocean environments.

Contents

1 Background

1.1 Neutrino Physics

1.1.1 History of neutrino

Wolfgang Pauli predicted the existence of neutrino in 1930 to explain energy-momentum conservation in beta decay. C. Cowan and F. Reines first detected neutrino in 1965 [1]. In their experiment, anti-electron-neutrinos created in beta decay scattered with protons to produce neutrons and positrons: $\bar{\nu}_e + p = n + e^+$. The positrons quickly annihilated with electrons and generated detectable gamma-rays.

In 1962 L. Lederman, M. Schwartz and J. Steinberger detected muon-neutrino $\bar{\nu}_\mu$ [2]. They used a 15-GeV beam of protons to strike a Beryllium target. This process produced pions, which partially decay into muons and muon-neutrinos. A thick iron shield absorbed all other strongly interacting particles except neutrinos. Finally, the neutrinos were detected in the spark chamber.

After tau leptons were discovered, its corresponding tau neutrino $\bar{\nu}_\tau$ also was expected to be detected. The first detection of $\bar{\nu}_\tau$ was announced in 2000 by DONUT collaboration at Fermilab [3]. They used a strategy similar to the muon-neutrino detection to produce tau-neutrino. An accelerated proton beam hits a tungsten target and produces mesons, which can decay into multiple types of secondary particles. Non-neutrino particles were filtered out by magnets and iron. The neutrino beam passed through nuclear emulsion layers, producing electrically charged particles and leaving visible tracks of several small black dots. Ionised chamber medium was converted to electric signals to be registered on scintillators. After the reconstructions of particle trajectories, tau-neutrinos were identified by those trajectories showing one single "kink", followed by its disappearance for a few millimetres and then a sudden reappearance.

1.1.2 Physics Properties of neutrino

Neutrinos have neither electric charges nor colour charges, so they are weakly interacting. Their massive gauge bosons ($m_W = 80.398 \pm 0.025$ GeV and $m_Z = 91.188 \pm 0.002$ GeV [4]) ultimately suppresses weak interactions.

Early neutrino experiments reveal already its properties and how it could be detected—let neutrinos interact with a nucleon and measure secondary particles. This process could happen via neutral current (NC) [5], mediated by Z^0, in which neutrinos scatter off of nuclei and create a hadronic shower:

$$\nu + N \rightarrow \nu + X \quad \text{(NC)} \tag{1.1.1}$$

The scattered neutrinos usually keep most of its energy, with only a fraction being deposited in induced hadronic showers. Alternatively, it can interact via charged current (CC) mediated by $W^{\pm}$ and create their charged lepton counterparts:

$$\nu_l + N \rightarrow l + X \quad \text{(CC)} \tag{1.1.2}$$

where l stands for leptonic charged counterparts in three flavours: $l = (e, \mu, \tau)$. Charged leptons, carrying most of the initial energy of neutrino, could create Cherenkov radiation if they are faster than the light speed in the medium.

1.1.3 Detection Principle

Large-volume detectors cannot directly detect any neutrinos but only the Cherenkov light emitted by secondary charged particles from NC and CC interactions. The light propagating inside a dielectric medium of refractive index n has speed:

$$c_n = \frac{c}{n}. \tag{1.1.3}$$

As shown in figure 1.1: if a charged particle traverses this the medium, it will cause local polarisation of medium. If its velocity is smaller than the speed of light in that medium (i.e., $v < c_n$), this local disturbance will go back to the equilibrium. However, suppose the particle travels faster than the local speed of light (i.e., $v \geq c_n$). In that case, it will have exited the neighbourhood where the disturbance takes place before polarisation could relax back to equilibrium. This process will leave behind a net polarised matter. The relaxation of matter will then no longer be annihilated but instead result in an emission of electromagnetic waves, i.e., Cherenkov radiation.

The origin of this emission will follow the particle trajectory. However, the photons will be emitted with an angle θ relative to it, which is specific to the particle's velocity and the medium. From geometrical arguments of the particle trajectory, it is:

$$cos(\theta) = \frac{1}{\beta n}, \quad \beta = \frac{v}{c} \tag{1.1.4}$$

The released Cherenkov photons number N_C per unit of length dx per wavelength $d\lambda$ from a charged particle with charge $q = z \cdot e$ can be calculated by equation(in Planck units):

$$\frac{d^2 N_c}{dx d\lambda} = \frac{2\pi\alpha z}{\lambda^2}(1 - \frac{1}{\beta^2 n^2(\lambda)}) \tag{1.1.5}$$

From the $1/\lambda$ dependence, we can see that the intensity is strong in the short wavelength range. Glass, used commonly as a material to build detectors' housing, absorbs the UV-light.

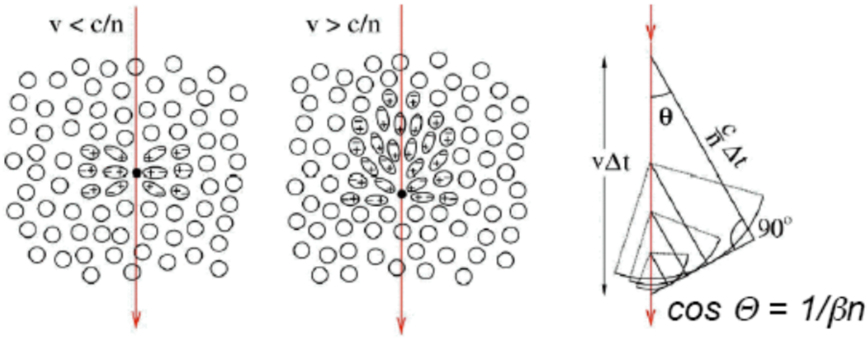

Figure 1.1: schematic illustration of charged particle propagation in medium. left and middle figures show the polarisation behaviour of the medium for particles with velocities smaller and larger than the speed of light in medium c/n. The right figure shows the geometry of relaxation wavefronts and particle propagation axis in $v > c/n$ condition. The figures are adopt from [6].

Considering these two factor, the **significant visible range of light distribute is between 300-600nm**.

The detection of Cherenkov photons is the most basic technique used to detect neutrinos in neutrino telescopes. The construction of neutrino telescopes always follows some common principles:

The photomultiplier tubes encapsulated in pressurised housings compose the optical module to detect the Cherenkov photons. The neutrino's energy and propagation direction can be reconstructed from the amount and the arrival times of the detected photons. Researchers can learn a neutrino's flavour by analysing the light patterns (see 1.5) and the amount of energy measured by the optical modules. The **great depth** of the detector location ensures a shielding from the secondary particles mainly produced by cosmic rays. Placing the detector underground can filter out a large fraction of atmospheric muons. Furthermore, the Earth itself can be used as a shield. In this condition, only neutrinos that have passed through the Earth will count as valid. The shortage of this method is: as the cross-section of neutrinos increases with their energy, earth can eliminate very high-energetic neutrinos, which is a problem. One solution is to let the detector also detect their accompanied muon-induced shower (like what IceTop does to IceCube), which are spatially and temporally correlated with atmospheric neutrino events and can be ruled out in the analysis. This method limits the sensitivity to high-energy astrophysical neutrinos to 20-30 degrees around the telescope's horizon.

The **total volume of the medium** determines the detection capability for high-energy neutrinos. Events created by ultra-high-energy neutrinos can easily extend over several kilometres. However, their energy can only be measured if the event is contained within the detector. The detector material has to be optically transparent (like water or ice) to allow for an undisturbed detection of neutrino-induced photons.

Each of the three neutrino flavours shows a distinct light pattern in the medium. Electron neutrinos create electrons resulting in a compact cascade, as they lose energy very quickly. The muon neutrinos create muons, leaving the tracks in thedetector longer than one kilometre. A tau can create two showers, one on its creation, and a second one on its decay, as the tau has a very short half-live of only $3 \cdot 10^{-13}$ s.

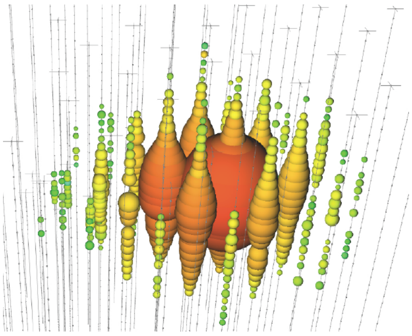

Figure 1.2: Cascade signature (E=1140.8 TeV)

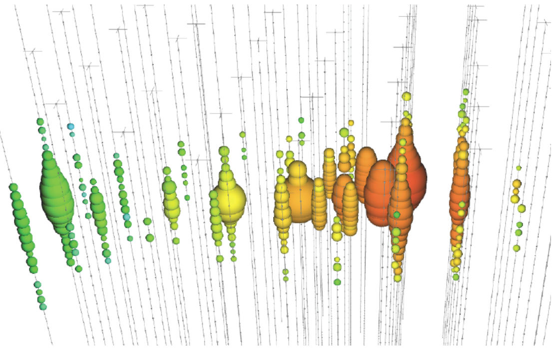

Figure 1.3: Track signature (E=71.4 TeV)

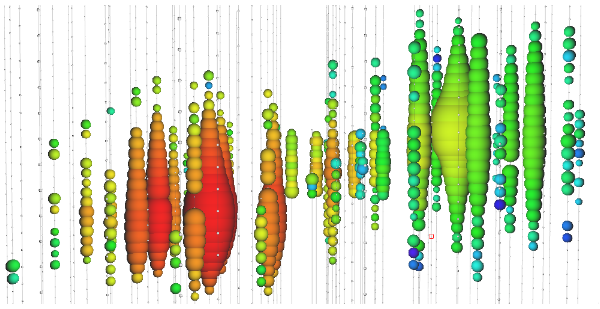

Figure 1.4: Double-bang signature (simulation)

Figure 1.5: Signatures that three different flavours of neutrinos left in the IceCube detector. Every coloured bulb represents a photosensor, the lines are columns of strings. The size of bulb represent detected photons number, the colour gradient represent its arrival time from early (red) to late (blue). The vertical distance between bulbs is around 17 meters [7].

As neutrino events are always scarce and so are opportunities to observe photons generated by them, the background photons from the medium itself should be as low as possible. Natural liquid water reservoirs always have some degree of bioluminescence, and in the case of saltwater, ^{40}K decays.

1.1.4 Neutrino Sources and Background to their Detection

i **Solar Neutrinos** In late 1960s, the first extraterrestrial neutrino source was discovered by Homestake experiment headed by R.Davis [8]. Active stars like sun produce energy by proton fusion in the core:

$$p \to n + e^+ + \nu_e$$

This experiment measured only a third of the expected solar electron neutrinos with the mean energies range $0.4 - 15$ MeV, giving rise to the debate of the famous solar neutrino problem. This inconsistency was finally explained by the theory of neutrino oscillation. Nowadays, experiments based on solar neutrino sources, such as Kamiokande and SNO, aim to determine neutrino properties and mixing parameters precisely.

ii **Supernova Neutrinos** The only supernova neutrino event was detected in 1987 when the star Sanduleak-69202 in the Large Magellanic Cloud turned into the supernova SN1987A. Multiple neutrino detectors, including Kamiokande-II, IMB, Baksan, detected a neutrino burst from the direction of SN1987A several hours before the visible light of the supernova reaches earth [9].

According to theoretical supernova models in which 99% of the energy released from core collapse is radiated away in the form of neutrinos, the estimated count of a total neutrinos is 10^{58} with a total energy of 10^{46} J, i.e., a mean value of some dozens of MeV per neutrino [10]. This value is consistent with the measurement.

Supernova neutrinos offer us a unique possibility of accessing internal conditions of events like supernova explosions. The emission is expected to take the form of bursts lasting several seconds with energies on the order of 10 MeV, with variations depending on initial conditions of the core collapse.

iii **Atmospheric Neutrinos** The primary cosmic radiation consists mainly of protons and helium nuclei. Since both of them are charged, they can be deflected by interstellar magnetic fields or scattered by interstellar medium to generate many secondary particles. All of these effects broaden the cosmic radiation spectrum from 10^3 eV to 10^{16} eV [5]. A better understanding of the ultra-high-energy composition of cosmic rays is a current research topic.

Cosmic rays collide with nuclei in the atmosphere and cause in the forward direction cascades of secondary particles, which can either further interact with atmospheric nuclei or simply decay. The cascades of particles will go on until the available energy is depleted, when cascading will come to a stop. Cascades have specific signatures dependent on the type and energy of incident particles and an energy distribution usually peaks in the GeV regime.

The process mentioned above is the main source of atmospheric neutrinos, which are the by-product of pions and muons' decays [11] in the atmosphere:

$$\begin{aligned} \pi^\pm &\to \mu^\pm + \nu_\mu \\ &\quad \hookrightarrow e^\pm + \nu_e + \nu_\mu \end{aligned}$$

Atmospheric neutrinos are both a signal (of atmospheric neutrino oscillation experiments) and the **dominant background** in the search for astrophysical neutrinos. The flux of atmospheric muon-neutrinos is several magnitudes higher than that of astrophysical neutrinos, and can traverse kilometres in water and ice.

iv **Cosmogenic Neutrino** Cosmogenic neutrinos are created when ultra-high-energy cosmic rays are scattered on the cosmic microwave background [12]. The primary process for producing high energies is the GZK effect. The secondary processes are only relevant for lower energies ($< 10^{15}$ eV). These interactions result in pions, which then decay into neutrinos [13].

$$p + \gamma_{CMB} \rightarrow \Delta^{+} \rightarrow \begin{cases} p + \pi^{0} & \rightarrow 2\gamma \\ n + \pi^{+} & \rightarrow l + \nu_{l} \end{cases} \tag{1.1.6}$$

As cosmogenic neutrinos have the highest energy and propagate to earth without further deflection, they are unique tools to study the universe on the PeV-scale.

v **Relic neutrino** As the universe increasingly expands, weak interaction rates dropped down and became less than the rate of expansion, so that neutrinos decoupled from thermal equilibrium interaction. Due to the expansion of the universe, nowadays, cosmic neutrino has a temperature of around 1.95 K (< 1 meV). These relic neutrinos, still to be detected, could offer an insight into the very early universe.

The energy spectrum in figure 1.6 shows the different energy distribution of abovementioned neutrino sources.

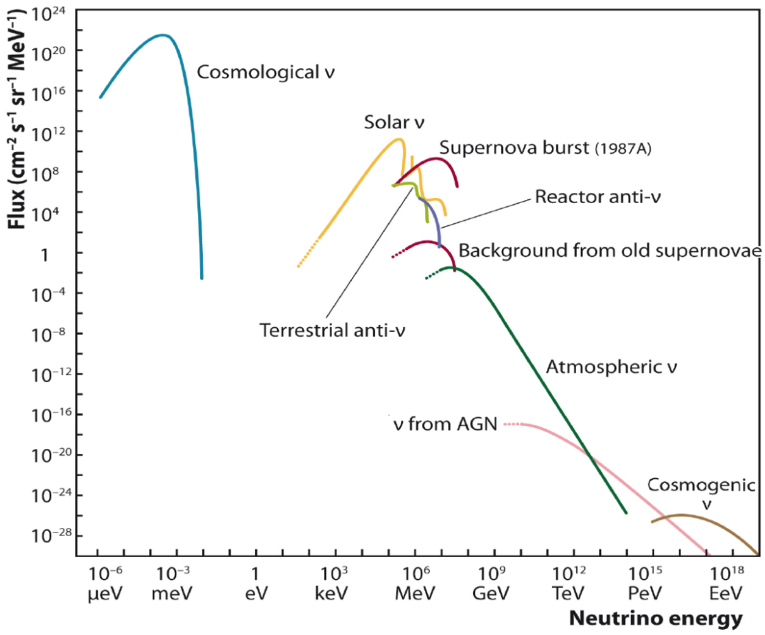

Figure 1.6: Measured and expected fluxes of neutrinos sources. As mentioned in the text: keV to GeV is the domain of underground detectors. The 10 GeV to about 100 PeV neutrinos with their small flux are only measurable by Cherenkov light detectors underwater and in ice [14].

1.1.5 Cosmic Accelerator

The neutrinos with energy larger than 10^{12} eV are considered as high energy neutrinos. Their production is connected with astrophysical acceleration mechanisms within our galaxy and beyond.

Supernova has an extremely compressed core. A rising of electron Fermi energy in its core allows the formation of neutrons and neutrinos. The shock acceleration process via supernova remnants (SNR) is a known acceleration mechanism. It is widely supported because its resulting power spectrum index has consistency with the theoretical model. In the shock accelerations, the kinetic energy of moving plasma is transferred to charged particles. A single particle can be accelerated several times until it can escape the shock front [15].

Pulsars are the rotating neutron stars. Pulsar wind nebulae (PWN) is possibly another accelerator. The magnetic field of pulsars is extremely high so that the charged particles can be magnetically accelerated [16].

Extragalactic accelerators are considered to accelerate cosmic rays and neutrinos beyond the energy of 10^{19} eV. The most likely candidates are active galactic nuclei (AGN). The model of AGNs is a supermassive black hole that accretes matter and emits two relativistic particle jets perpendicular to the accretion disk. Its relativistic electromagnetic emission is capable of accelerating the particles to high and ultra-high energies [17].

2 Large-scale Neutrino Telescopes

2.1 IceCube and other neutrino telescopes

IceCube telescope located at Amundsen-Scott south pole station is designed to observe neutrinos with energies around a few tenths of TeV. As shown in 2.1, over 5160 photosensors called DOMs (digital optical modules) hung on 86 strings were deployed in ice holes between 1450 m to 2450 m below the sea level. Inside each DOM are a large 10" downward-facing photomultiplier tube (PMT) and the read-out electronics. All the instrumentation encapsulated in a glass pressurrized sphere.

The DeepCore — a sub-array of IceCube — is specifically designed for the low-energy neutrino detection. It consists of 8 strings of 60 compactly placed DOMs. This narrow placement of DOM enables the detection of 100 GeV particles with a short absorption length as well as an unambiguous identification of their incidence pattern.

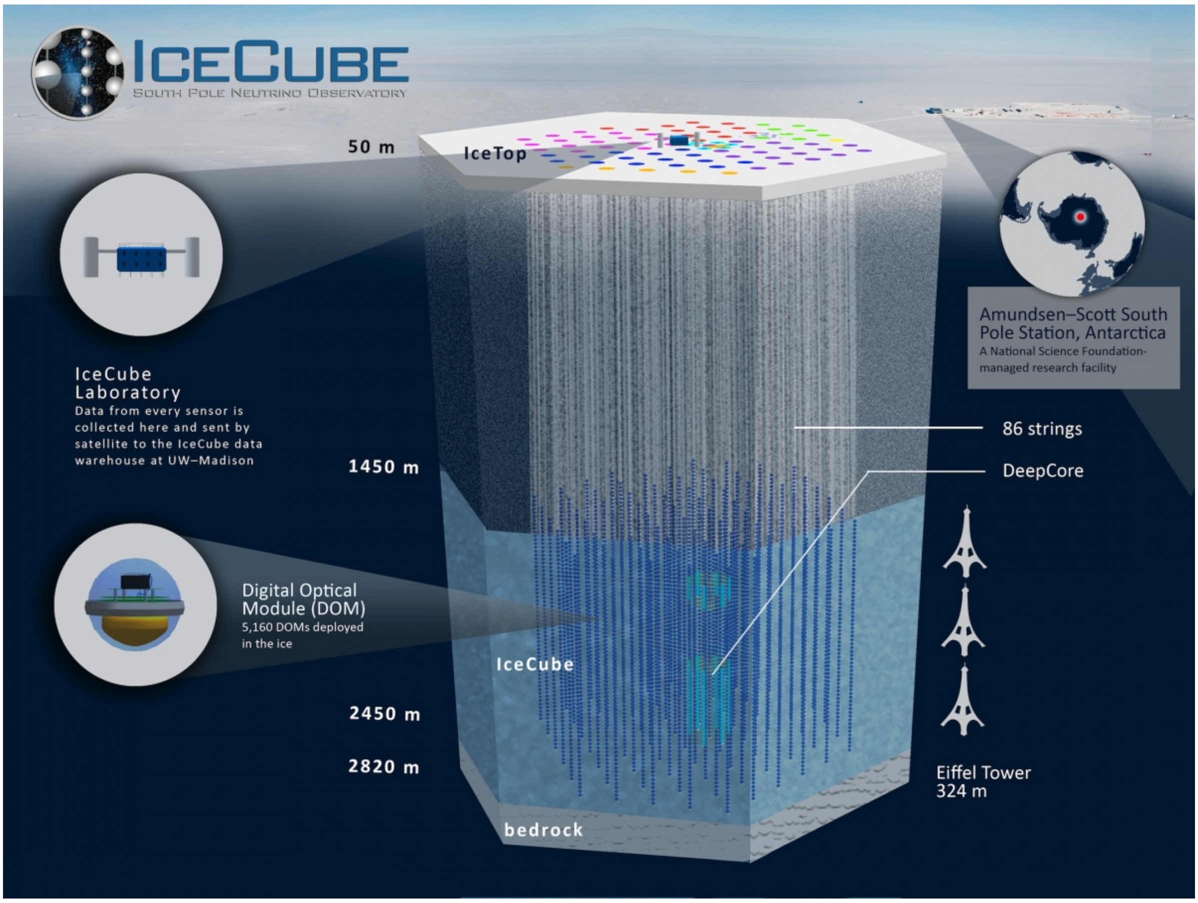

Figure 2.1: Sideview of IceCube with illustration of a DOM[18].

The optical properties of ice can be determined only within an uncertainty of about 10%, which is currently the most unavoidable limitation to, e.g., optimal directional resolution of neutrino induced events. Individual DOM efficiency and angular acceptance are other major systematic uncertainties, which could be better calibrated for superior performances. The new methods and instrumentations are subjects of ongoing studies covered by IceCube-Gen2—IceCube's future upgrade—which will increase the volume from 1 to approximately 10 km^3 [19].

In IceCube, electron neutrino showers and muon neutrino tracks have been observed. The search for the tau double-bang is still ongoing. The first very-high-energy neutrino flux from outer-space was detected in 2013, the result of which was published in Science in November 2013 [20]. In 2017, the first compelling evidence for an association between high energy neutrinos and a known blazar was reported [21]. A radio-bright blazar TXS0506+056 at redshift z = 0.3365 was observed to be flaring up with gamma-rays at an angle of 0.1 degrees from the direction of the high energetic neutrino induced muon track.

Out of hundreds of high-energy astrophysical neutrinos detected by IceCube, only a small number have been traced to astrophysical sources, leading to an open question of where does the bulk of the observed flux originate. A global effort is now forming to fully investigate the high-energy neutrino sky and reveal the most powerful cosmic accelerators in the universe [22]. Participants of this global coalition include the neutrino telescope **KM3NeT** [23], which is being constructed at three different locations in the Mediterranean sea. Each of the three contains 115 detection units and covers a volume of a half km^3. The **Baikal-GVD detector** [24] is under construction in Lake Baikal, Russia. It is planned to have 8 clusters, each one equipped with 8 strings holding 288 optical modules altogether. The project I am currently involved in is **P-ONE** in the Pacific Ocean.

2.2 P-ONE

IceCube's success in observing high-energy neutrinos motivates us to build other large-scale neutrino telescopes. Ocean Networks Canada (ONC), as one of the world's largest oceanographic observatories, provides us with the required infrastructure at a depth of 2660 meters in Cascadia Basin [25], which has been chosen as a base for the Pacific Ocean Neutrino Experiment (P-ONE [26]). With KM3NeT, Baikal-GVD and IceCube-Gen2, as well as P-ONE, the detectable area of astrophysical neutrinos at the highest efficiency covers almost all-sky (as shown in figure 2.2).

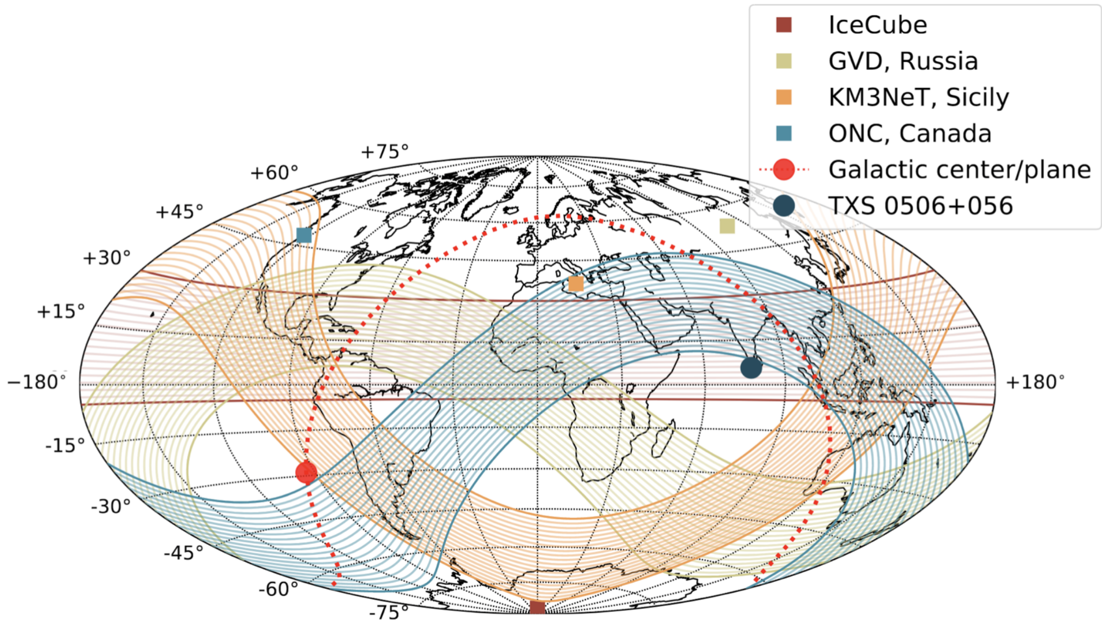

Figure 2.2: Global neutrino telescopes existing and under construction, with their horizontal coverage as color band (bands use the same color as detector marker). In side the coverage high energy neutrinos will not be affected by the Earth absorption [26].

Cascadia Basin has a wide and flat sedimented surface with a temperature below 2 C°. The expected major background for neutrino detection in Basin comes from various organisms that emit bioluminescence. P-ONE will be a system with several cubic kilometers of instrumented volume (see figure 2.3). The detector geometry is being optimized to obtain maximum acceptance of neutrino-induced tracks near the horizon, while the horizontal tracks offer the best angular resolution in a neutrino telescope.

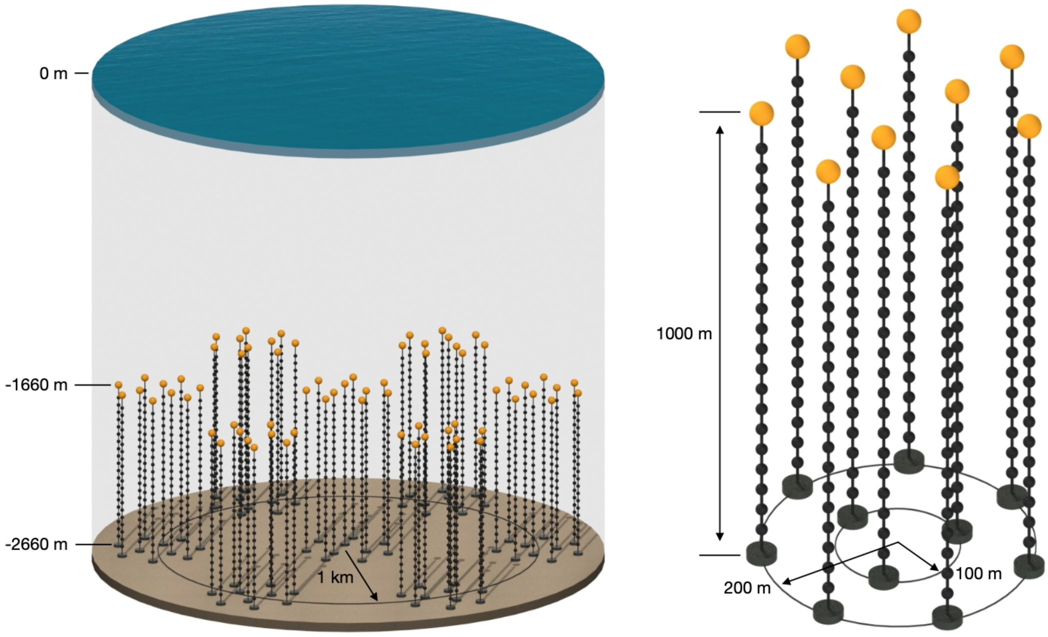

Figure 2.3: Design of P-ONE single segment (right) and complete structure consisting of seven segments (left). The structure is optimised for neutrinos energy above 50 TeV and have high acceptance calculated by the empirical formula: $\int_0^{\infty} A_{eff}(\delta, E_\nu) \cdot E_\nu^{-\gamma} dE_\nu$ [26].

3 STRAW and STRAW-b conception

STRAW stands for "The Strings for absorption length in Water". The STRAW and STRAW-b experiment aim to qualify the deep Pacific Ocean, especially study the optical properties of deep sea water and the bioluminescence [27] [28]. Both are essential to the detector performance.

3.1 STRAW

STRAW is a two-string detector, with 4 optical modules hanging on each string [29]. It has been deployed around June 2018 in Cascadia Basin in collaboration with ONC. The two-string configuration (see 3.1) allows for coverage of distances between two arbitrary modules ranging between 20 m and 100 m. Furthermore, its symmetry allows for a crosscheck of results taken by different sDOMs.

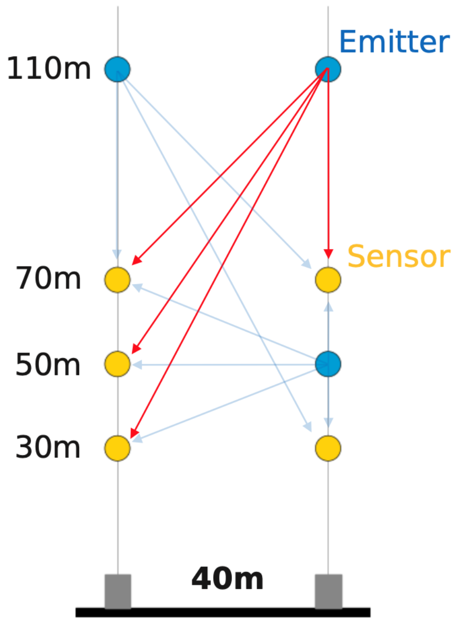

Figure 3.1: Sketch for STRAW two-strings detector [30]: Blue spheres are the light emitters: Precision Optical Calibration Module (POCAM). Yellow spheres are the receivers: STRAW Digital Optical Module (sDOM). Grey squares are the mini junction boxes (MJB), an intermediate signal transfer station. Different lengths between modules make arrived light achieve certain degrees.

The main function of the POCAM [31] is producing nanosecond-scaled, highly isotropic light pulses with central wavelengths at 356, 400, 465, 252 and 605 nm. It uses two different methods to produce light: one is called faster Kapustinsky [32], where light pulses have a fixed time FWHM of 10 ns and $10^9/4\pi$ photons on average; the other is FPGA-driven pulses, which has an FWHM > 40 ns and an adjustable waveform.
The sDOMs measure light pulse and have, in each module, two R12199 PMTs, one of which faces the up-facing hemisphere and the other the bottom-facing hemisphere. Each sDOM has its own local data acquisition (DAQ) device, but synchronised to a central timing system (CTS) inside MJB.
The PMTs in the sDOM are directly connected to the read-out system called TRB3sc, which is developed by GSI Helmholtzzentrum Darmstadt and first used for CERN collider experiments, and a front-end board PaDiWa3. TRB3sc is an integrated system containing a FPGA-platform, TDC (time-to-digital converters)-in-FPGA technology with a 10-ps precision, front-end electronics and a complete set of data acquisition and control software. More description on their functionality is in section 5.1.

(a) CAD cut view of POCAM

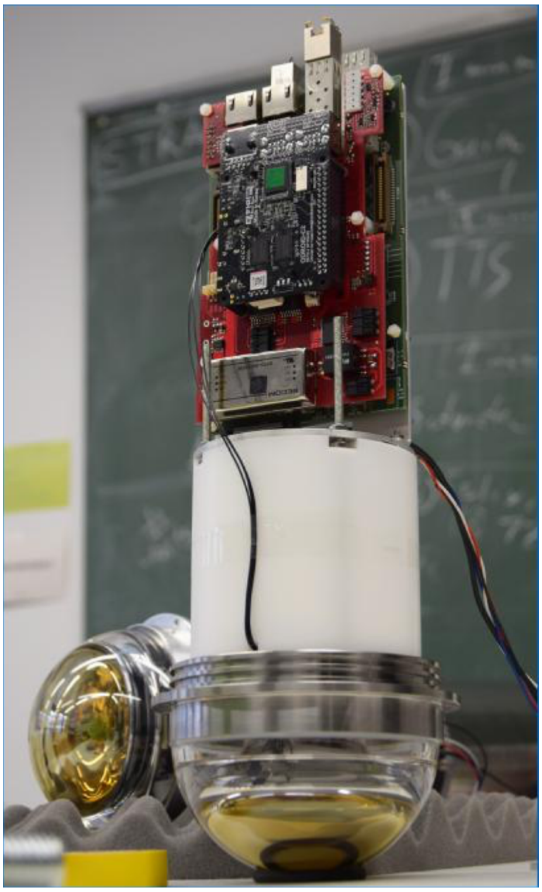

(b) sDOM inside with one hemisphere assembled

Figure 3.2: Two types of optical module used in STRAW experiment [33].

After operating for more than one year, the accumulated data on STRAW has fulfilled the time-span and quantity requirements of a finer analysis. In all obtainable information, attenuation length in deep-sea water (major works are done by Dr. Christian Fruck(TUM) and Andreas Gärtner(University of Alberta)) and features of bioluminescence background (major works are done by I.C.Rea(TUM)) are the most important.

3.1.1 Attenuation length Analysis of STRAW

The POCAM emits 2.5 kHz pulses in STRAW's operation. The average photon number pro detected flasher is 0.0788, which is known as hit-fraction.

We already know the POCAMs emission properties of e.g. frequency and expected photons number. Therefore, we can estimate the detected photon number at each sDOM's location using the equation:

$$N(r) = \frac{N_0}{4\pi r^2} \cdot \exp\left(\frac{-r}{l_{attenuation}}\right) \tag{3.1.1}$$

The attenuation length depends on absorption and scattering length as in:

$$\frac{1}{l_{attenuation}} = \left(\frac{1}{l_{absorption}} + \frac{1}{l_{scattering}}\right) \tag{3.1.2}$$

Which of the two components dominates, varies by medium. In water, the absorption effect outweighs scattering effect, whereas in ice, the opposite is true.

To estimate the detected photon numbers, we have built a simulation model incorporating realistic effects contributing to the deviation of light propagation away from idealisation. In this model, the most important free variable is the attenuation length. Other parameters like POCAM calibration parameter, quantum efficiency of sDOM and threshold efficiency, geometry factors and so on, are known within a given uncertainty. By fitting the model predicted hit-fraction to measured hit-fraction, we can determine the attenuation length. The results of this fitting are shown in figure 3.3:

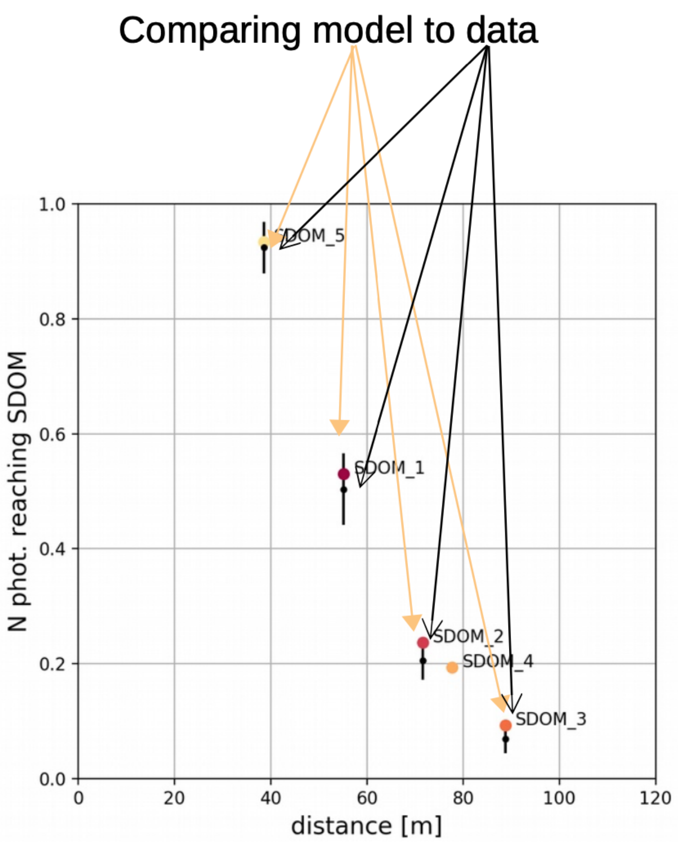

Figure 3.3: POCAM2 measured photon number (hit-fraction) in comparison with simulation. The bigger points are results from modelling. Their colour presents its magnitude of deviation from the measured result (red points have a larger deviation than yellow). Black points and their error bars show measured data. sDOM4's data is not used because of geometry shadow[34].

The simulated data agree with the prediction within their error bars. The data collected from 01/2019 to 05/2020 were analysed and plotted chronologically. During this period, the attenuation length fluctuates little (see 3.4), indicating the data's reliability to a certain extend.

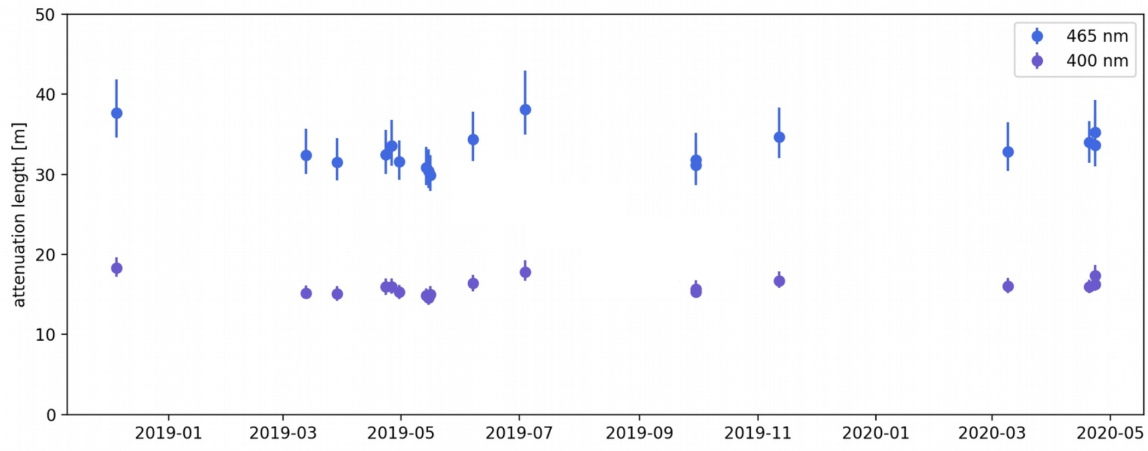

Figure 3.4: the attenuation length results of 465/400 nm light are stable in seasons [34].

We compared the values of attenuation length from different neutrino string experiments (see figure 3.5). The measurements done by other experiments (Baikal, KM3NeT) are differed from different environments and deviate from theory, which is not surprising because the theory model by Smith&Baker [35] assumed an idealised scenario with pure water. Any impurity in the water can lead to transmissibility drop drastically.

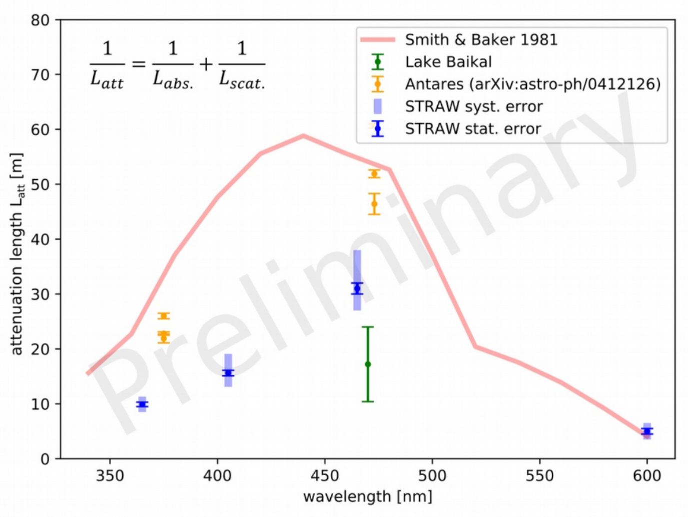

Figure 3.5: The results of the attenuation length in relevant wavelength range. Measured by different neutrino detect string experiments, in comparing with theoretical model by Smith&Baker [35]. From this plot we can see that the water purity in Cascadia site is not as good as Antares, but better than Baikal [34].

3.1.2 Bioluminescence Background Analysis from STRAW

STRAW sDOMs continuously record light background in Cascadia Basin. One can gain an understanding of measurement by simply plotting the intensity-time spectrum or Fourier-transforming its time trace in the long run. The following figure gives an example of typical background measurement on sDOMs.

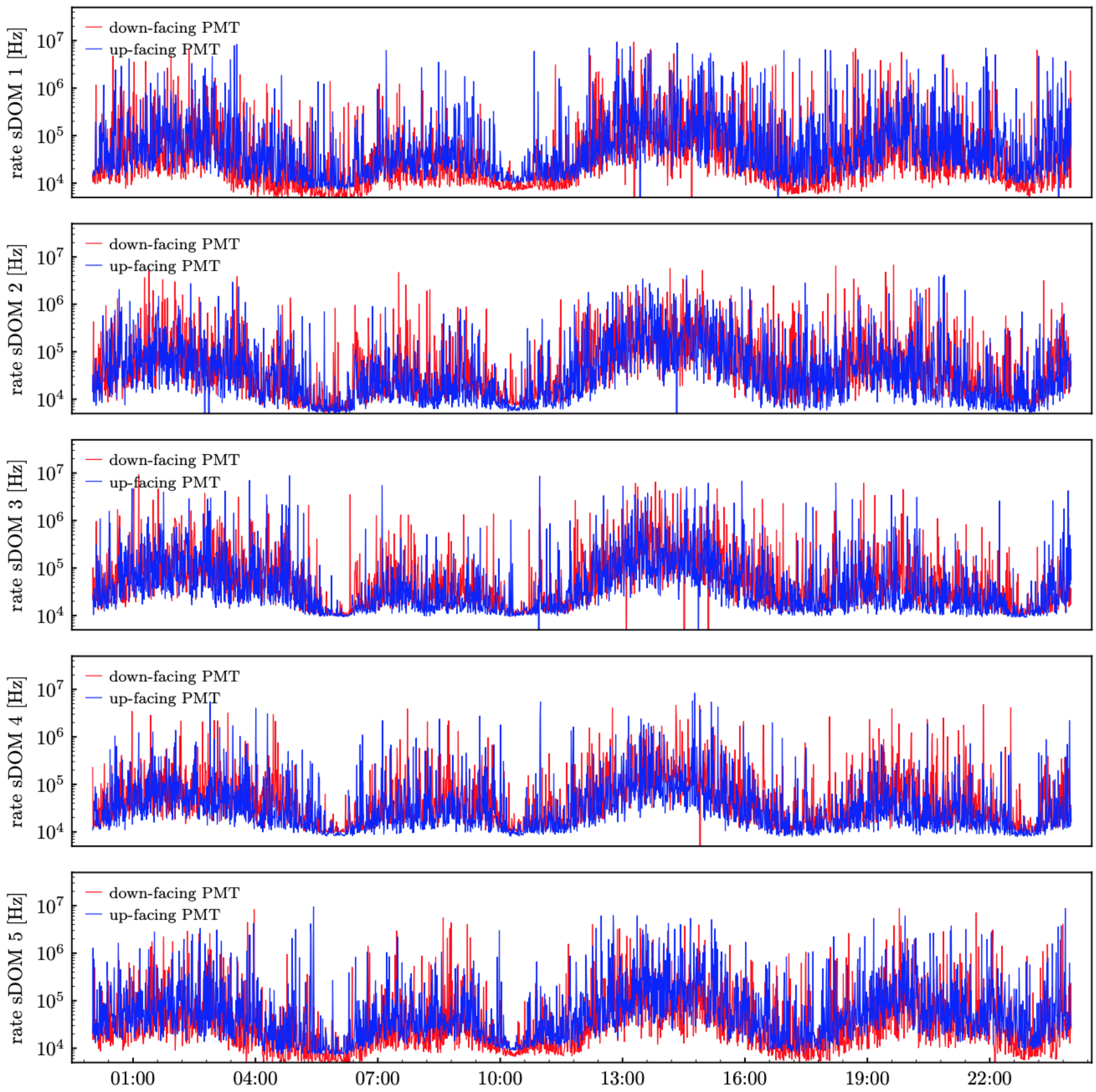

Figure 3.6: One-day dark rates recorded by all 10 PMTs in 5 sDOMs. The rates vary from 10 kHz to 10 MHz [33].

All 5 sDOMs measured similar time-domain intensity patterns on the time scale of the year (as shown in figure 3.6), but different distributions when compared month to month and on a shorter time scale (as shown in figure 3.7). The most likely cause for the rapidly changing background light is bioluminescence caused by deep-sea microorganisms.

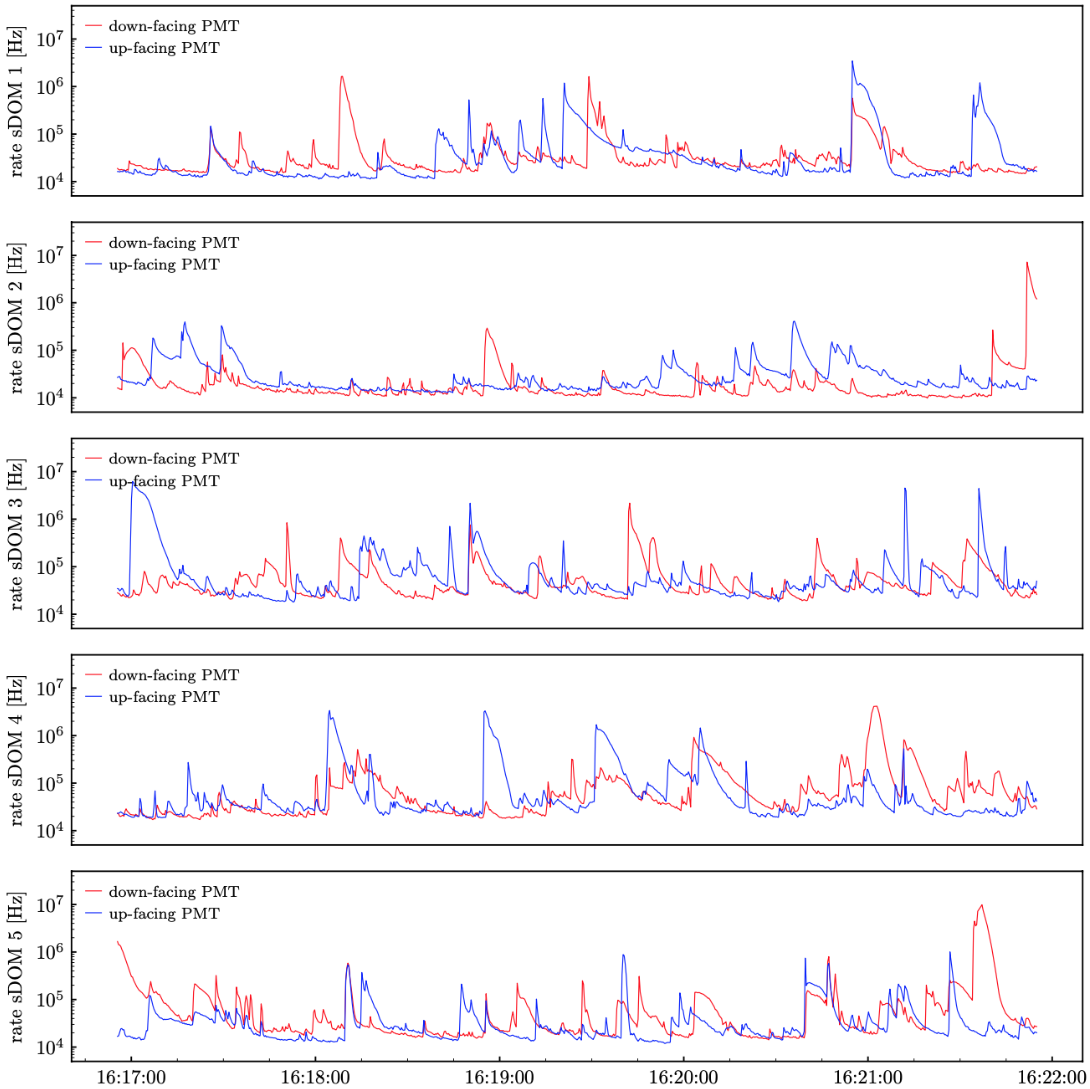

Figure 3.7: The five-minutes dark rates records show fine structure of the flashes. The gamma-distributed pulses indicate they most likely came from bioluminescence [33].

From additional studies, the photon numbers received by the sDOMs correlate strongly with water currents (figure 6.1). Events repeating monthly or daily could be attributed to global environmental changes such as the tides. In contrast, those occurring on a shorter time scale, such as hours or seconds, could be due to local water current turbulence. The turbulence agitates bioluminescent animals and causes their sudden light burst. The turbulence effect will be further investigated in chapter 6.

3.2 STRAW-b conception

STRAW-b is the second path finder for P-ONE. It is a single string hosting 10 modules installed inside spherical glass housings to emulate the structure of the P-ONE string. (see 3.8) Each module has environment sensors and also module-specific instruments fulfilling its unique function.

Instead of using POCAM as light emitters as done in STRAW, we use an integrated ultra-bright Lucifer LED board inside each STRAW-b module to generate white and UV-light. Three cameras commonly used in the field of astronomy are installed inside each spectrometer module to take a snapshot of bioluminescent marine animals.

So far, there is no measurement of the deep-sea bioluminescence emission spectrum. In the past experiments, including STRAW, we only know integrated background photons number, but not their energy distribution. To obtain the spectrum of bioluminescence, we add mini-spectrometers and PMT-spectrometers into STRAW-b design.

Using STRAW, we have measured the attenuation length of the deep-sea water. Both absorption and scattering contribute to attenuation, but the former usually predominates. During STRAW-b experiment, we want to precisely know the scattering length and absorption length separately. For this purpose, we need LiDARs. To accommodate the need of those interested in studying atmospheric muon flux and verifying existed empirical muon rate formula, we also add a muon tracker.

In STRAW-b, we use a longer mooring line ($\sim$ 500 m) than those used in STRAW. This line is closer to the strings composing the large-scale neutrino telescope. This similarity allows us to test whether the string deployment technique is also reliable for the upcoming P-ONE experiment.

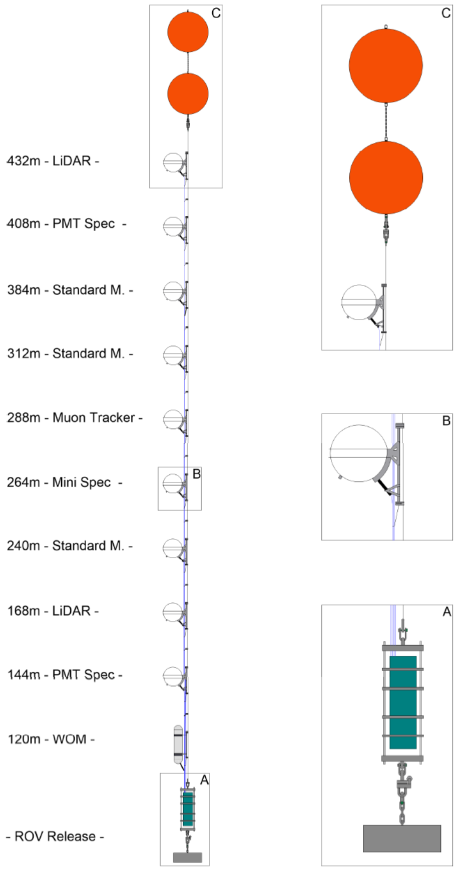

Figure 3.8: sketch for STRAW-b single string detector. It consists of: i. 2x PMT spectrometer; ii. 1x Mini-spectrometer; iii. 1x Muon Tracker; iv. 2x LiDAR; v. The Wavelength shifting Optical Module (WOM) developed by University of Mainz; and the MJB. The image is a courtesy of Christian Spannfellner (TUM).

3.2.1 Standard Module

The standard module is **a set of supporting electronics** shared by all STRAW-b modules. Mounted in each module's lower hemisphere, they supply power, log data, and communicate with specialised measurement instruments in the upper hemisphere.

Apart from this supportive purpose, the standard module itself serves as a hardware testbed for a couple of components and techniques of interest to P-ONE. This is the reason for having several standard modules on STRAW-b's mooring line.

3.2.2 LiDAR

LiDAR (**Li**ght **D**etection **A**nd **R**anging) device within STRAW-b precisely measures on-site optical properties at a single wavelength [36]. Its pulse generator ThorLabs NPL45B operates at 450 nm and produces a light pulse with a duration ranging from 5 to 40 nanosecond. An external trigger can control the pulse width and repetition rate.

Back-scattered light will be collected by a lens and measured by a HAMAMATSU μ-PMT. This type of PMT outputs a digital signal which requires no further amplification or discrimination. Therefore, the read-out of the LiDAR is the light intensity as a function of time (or event distance). The emitter-receiver system, which is mounted on a motorised gimbal stage, can freely rotate in the upper hemisphere. The STRAW-b mooring line has two LiDARs, one of which scans different angles as an emitter and the other as a receiver.

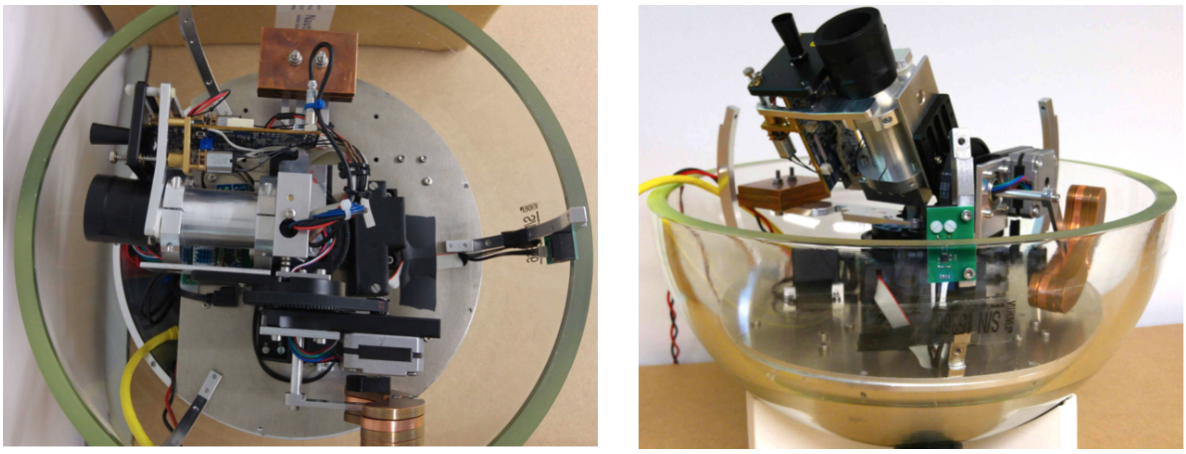

Figure 3.9: LiDAR's gimbal view from above(left) and LiDAR's laser light receiver system point to 60 degree up (right). The images are courtesy of Christian Fruck.

The two LiDAR modules are placed directly above the two PMT-spectrometer modules. A Lucifer board that generates white and UV light is installed on each LiDAR's lower hemisphere. Since its emission spectrum is fully known and covers the entire PMT-spectrometer measurement range, the PMT-spectrometer, if calibrated, allows us to measure the ocean water's absorption in many different wavelength bands.

3.2.3 PMT-spectrometers

The LiDAR, as described above, measures only integrated photon numbers, rather than their energy distribution. To fully access the bioluminescence's spectrum at the Cascadia Basin, two PMT-spectrometer are added. Each PMT-spectrometer hosts 12 PMTs, installed with 11 filters working within a specific wavelength range. Collectively, they are expected to cover the entire emission spectrum of the bioluminescence. The lenses in front of every PMT's focus the incoming light onto the PMTs and limit the field of view. Specially designed 3D-printed symmetrical holding structures align the PMTs to the directions to correct the refraction of the spherical glass.

(a) PMT-spec module view from above (b) PMT-spec module view from the side

Figure 3.10: The images are courtesy of Kilian Holzapfel.

The design, assembly, and calibration of PMT-spectrometers, which this thesis mainly concerns, will be described in later chapters 4 in detailed.

3.2.4 Mini-spectrometer

While the PMT-spectrometers excel in low-light detection, the mini-spectrometers module complements the PMTs with a wide dynamic range. The mini-spectrometers cover exclusively the high-intensity regime, where the PMTs are saturated.

The mini-spectrometer module consists of 5 Hamamatsu C12880MA spectrometers and a low-light astronomy camera. The integration time of a single measurement and the time-window between two measurements can be controlled.

To characterise the dark current produced by internal electronics, we measured it at the temperature between 0 to 35 Celsius with various integration time from 0.1 to 120 milliseconds. The actual measurements will take the dark current on every mini-spectrometer's pixel into account.

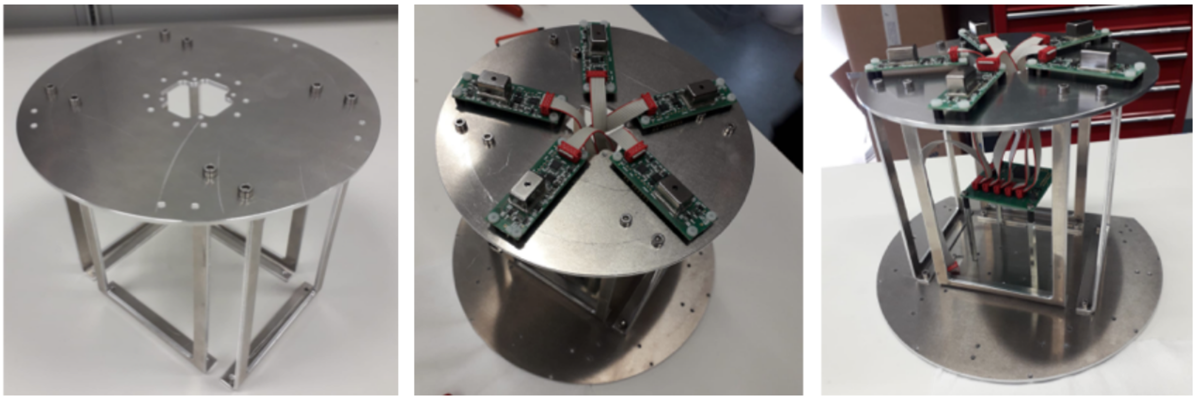

Figure 3.11: Partly assembled mini-spectrometer module. A camera is placed in the centre of five Hamamatsu mini-spectrometers. The five mini-spectrometers are connected to "Brigette" board. The images are courtesy of I.C Rea.

3.2.5 Muon Tracker

The muon tracker module gathers not only the muon rate in the Pacific Ocean [37], but also the approximate incident direction of the muons.

The module consists of two housing boxes. One box is placed above the other with a certain distance (see 3.12). A Teflon frame internally partitions each housing box into 4 square areas, each equipped with a BC-404 plastic scintillator tile. Either box is covered by reflective foil and aluminium plate on both sides, trapping photons for sufficiently long that they reach photosensors after reflections. PM3315-WB-B0 SiPM matrices read out the light output of the scintillators. Every SiPM matrix consists of nine SiPMs connected in a parallel fashion.

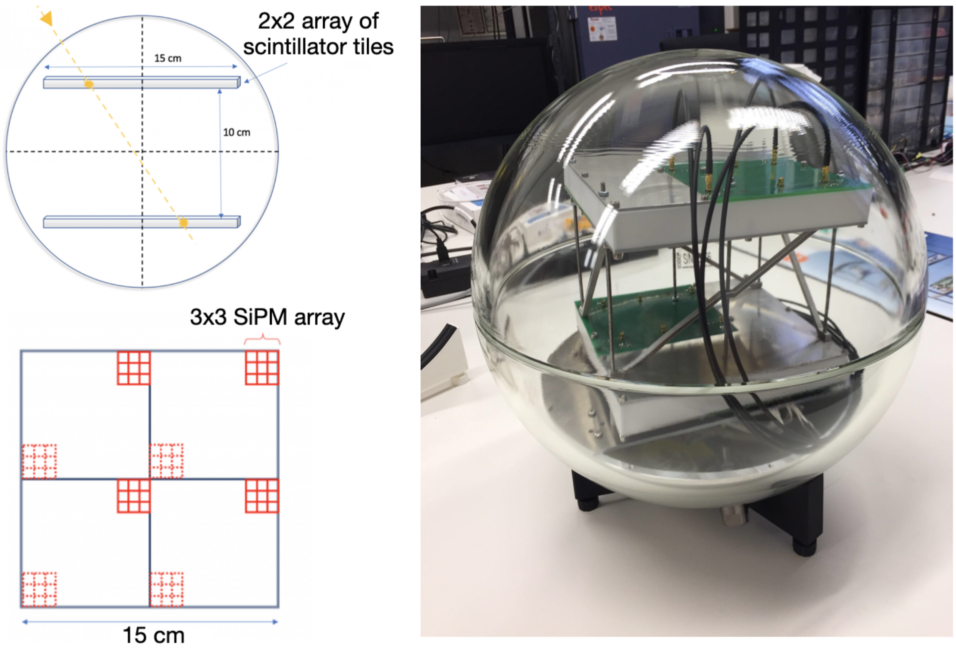

Figure 3.12: Assembled muon tracker module (right) with the dimension of two housing box. The two housing boxes are internally partitioned into 2x2 areas, equipped scintillator tiles. 3x3 SiPM array are sticked to the upper right and lower left corners of each area (left). The images are courtesy of Laura Winter.

3.3 Electronics of STRAW-b

This section explains STRAW-b-specific acronyms, which are based on commonly used abbreviations in the field of electrical engineering. The short explanations of the latter can be referred to the glossary.

The vertical electrical optical cable (VEOC) contains two fibres which transfer data between the modules, and two copper wires which supply power.

The data readout is based on TRB3sc system as is done in STRAW, with the following additional electronics:

- Phobos: an integrated board holding DC-DC converter, digital-to-analog converters (DAC), analog-to-digital converter (ADC) and GPIO pins. The phobos board is used for signal conversion, power supplement and distribution, serves as an interconnection between TRB3sc and Odroid-C2.

- PaDiWa: the front-end electronics of TRB3sc. It is used for signal amplification and discrimination.

- PaDaAdap: PaDiWa adaptor board. It is a simple board that adapts MMCX connectors, which are used on PMTs and SiPMs, to PaDiWa's pin connections.

- Odroid-C2: single-board computer to run the control software and the data acquisition software. It communicates with Phobos board via I2C-connection and GPIO pins.
- Bridgette: six ports SPI multiplexer to connect one camera and five Mini-spectrometer. It is connected with the Phobos board via GPIO ports.
- Media Converter board: It converts the signal from VEOC to a configurable Ethernet switch. In this way, it isolates the TRB3sc from data transmission backbone effect.
- Battery-Powered data logger: It hosts pressure, temperature, humidity, acceleration, and magnetic sensors to record the physical conditions of the modules during the deployment. It is connected to Odroid-C2 via USB port.

The following figure 3.13 and 3.14 show both schematically drawing and real manufacture of STRAW-b electronics.

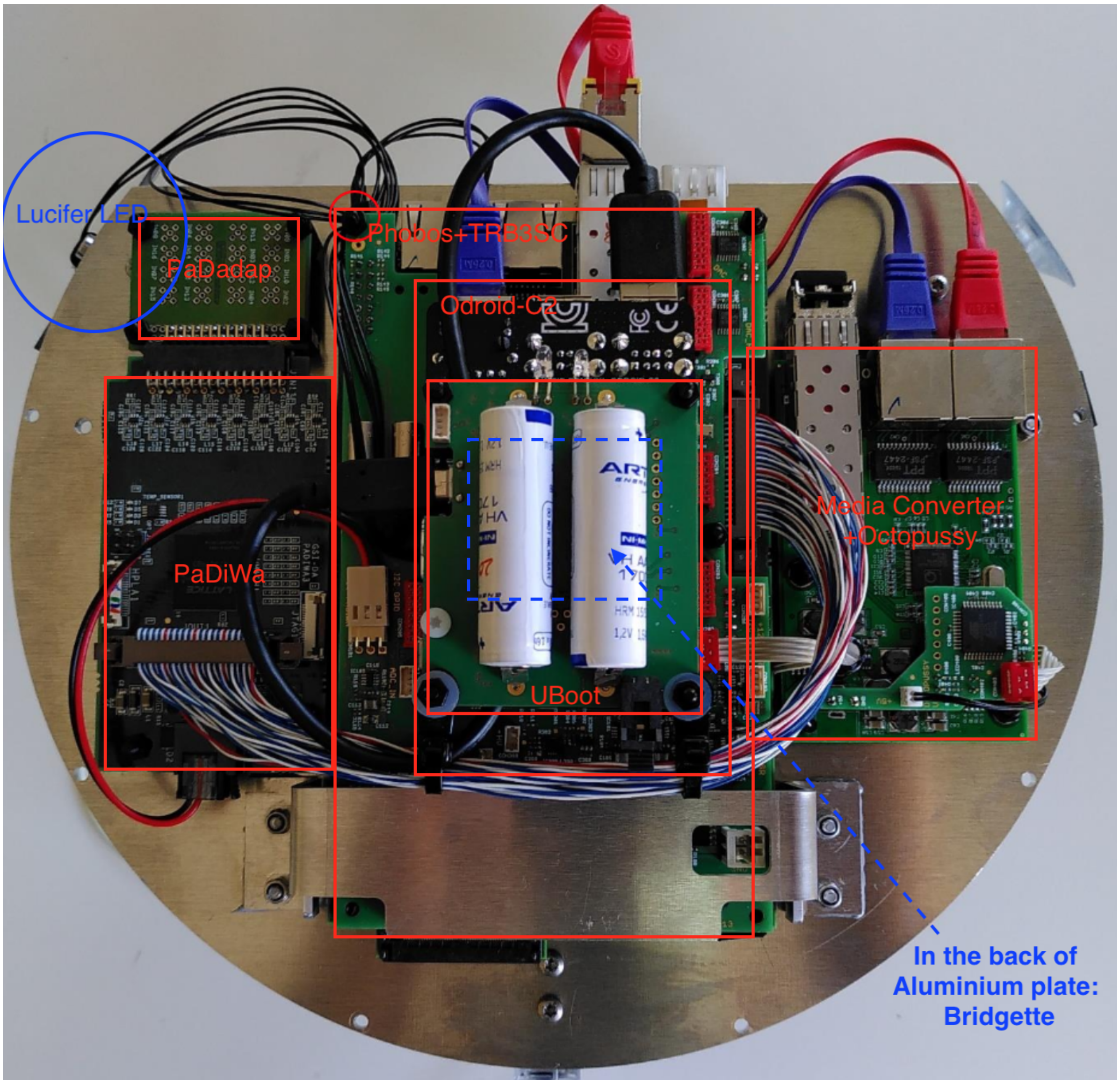

Figure 3.13: Above view of STRAW-b standard module. Electronics components mentioned in the text are fixed to aluminium plate together with thermal pad, heat sink metal bar and the necessary protection.

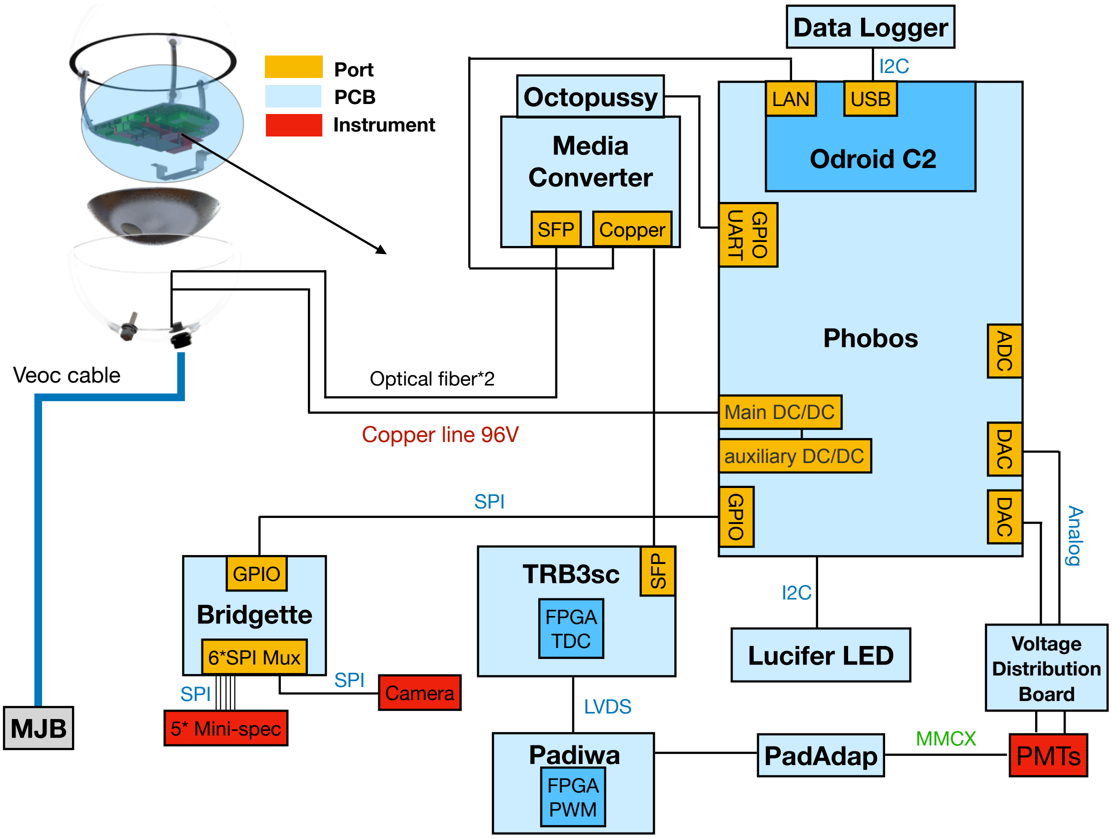

Figure 3.14: Sketch of the connections between STRAW-b electronics. Blue parts stand for PCB boards; red parts stand for external device; orange part stand for the ports on the board. Note beside the lines are protocols or connector type used at the port.

4 Design and Calibration of the PMT-Spectrometer Module

This chapter records the PMT-Spectrometer's development. The choosing of every single component, the decisions on design parameters, and the full characterisation of its behaviours—all the steps we have taken, aim to the final goal: having an informative and accurate measurement of the deep sea bioluminescent spectra via the PMT-spectrometers.

Before the assembly of the module, several measurements were performed to characterise individual components installed in the PMT-spectrometer.

4.1 Gain on single PMT

A total of 32 PMTs manufactured by Hamamatsu (16 with serial number R1924A, 16 with serial number 1925A) were characterised, aiming to find the ideal supply voltage (HV) for each of the PMT.

According to the datasheet, the maximum HV that can be applied to Hamamatsu R1924 and R1925 PMTs is 1250 V. Simple measurements have shown a significant amplification with supply as low as 750 V. Therefore, in actual experiments, we use a Hamamatsu HV amplifier to linearly scale supply voltage $3 - 5$ V up to $700 - 1250$ V. A Tektronix oscilloscope (MSO54) is used to measure the PMT's response.

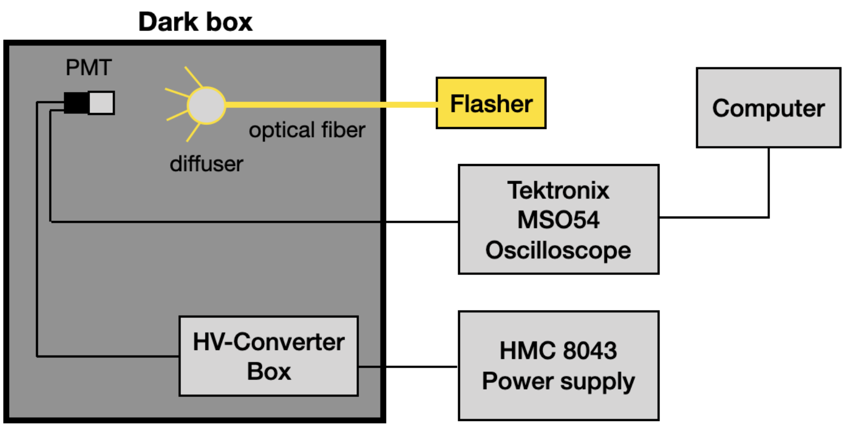

Figure 4.1: Experimental setup for the measurement of the PMT's gain.

The calibration measurements use an external flasher as a trigger. While the PMT is placed inside a dark box to shield it from the light in the environment, the flasher is placed outside in order to prevent its thermal noise from affecting the PMT. An optical fibre couples the light from the flasher to a diffuser inside the dark box. We scan the external voltage from 3 V to 5 V with a step of 0.5 V. For each step, we save the time trace of each PMT pulse voltage on the oscilloscope into a csv file.

We use the formula:

$$\text{Gain} = \frac{\text{Voltage}}{\text{e} \cdot 50\Omega \cdot t_{\text{record length}}} \tag{4.1.1}$$

where 50 Ohm is the oscilloscope's internal resistance, and $t_{\text{record length}}$ is the sampling period. In the case of the single-photon condition, this formula converts voltages into photoelectron counts. The photoelectron counts are plotted into a histogram (figure 4.2). The peak to the right is always the pedestal (environmental noise), which can be fitted with a gaussian and then subtracted. The peak to the left is caused by a single photonelectron. Sometimes (not shown in this figure), there will be multiple small peaks in the high-gain regime that can be attributed to afterpulse, which will also be subtracted. The weighted arithmetic mean of the remaining gain histogram is calculated. This gain is the data point to be collected for one supply voltage step. This procedure will be repeated for every voltage step.

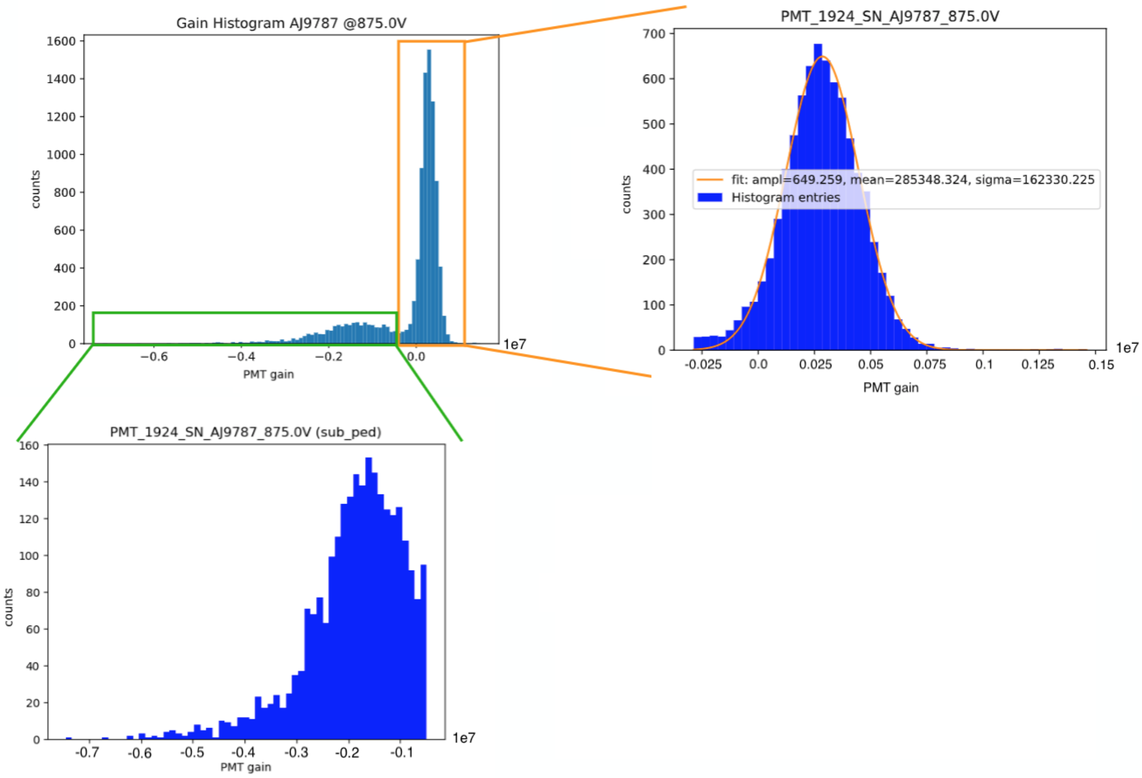

Figure 4.2: Calculation of the gain. Upper left is the counts histogram from original oscilloscope data. The Orange windows shows the gaussian fit for pedestal which need to be subtracted. The Green windows shows the peak from single photonelectron.

The gain-to-supply-voltage curves of R1925 and R1924 PMTs are separately shown in the figure 4.3. As one can see, the gain of R1924 series is generally higher than R1925, which makes the former PMTs superior.

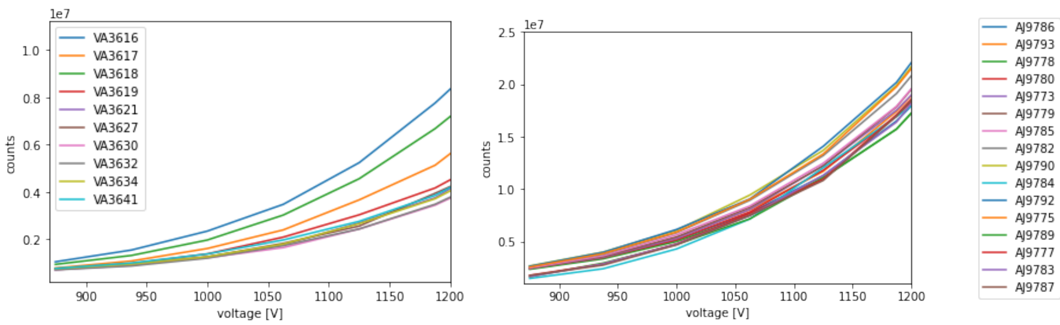

(a) Gain of R1925 PMTs

(b) Gain of R1924 PMTs

Figure 4.3: The gain curve of all PMTs, labeled with their serial number.

4.2 Quantum Efficiency of the single PMT

In order to evaluate the quantum efficiency (QE) of our PMTs, we illuminate them with different wavelength ranging from 300 to 600 nm and measure the output current as a function of the wavelength. We have a calibrated photodiode (PD) whose QE at certain current is known for wavelength from 200 to 800 nm. Since the current is proportional to the QE, we can calculate the QE of the PMT referring to the PD, if they are illuminated in the same way. A filter with adjustable wavelength combining with a white light source produces a light of varying wavelength. Moving the filter from left to right makes the wavelength of the light source changing from 300 to 800 nm.

As one can see in figure 4.4, each PMT is mounted via a socket on a PCB, which also has an HV and LEMO connector for the measurement of current; For calibration measurements, a reference PD is mounted on a second PCB with a LEMO connector.

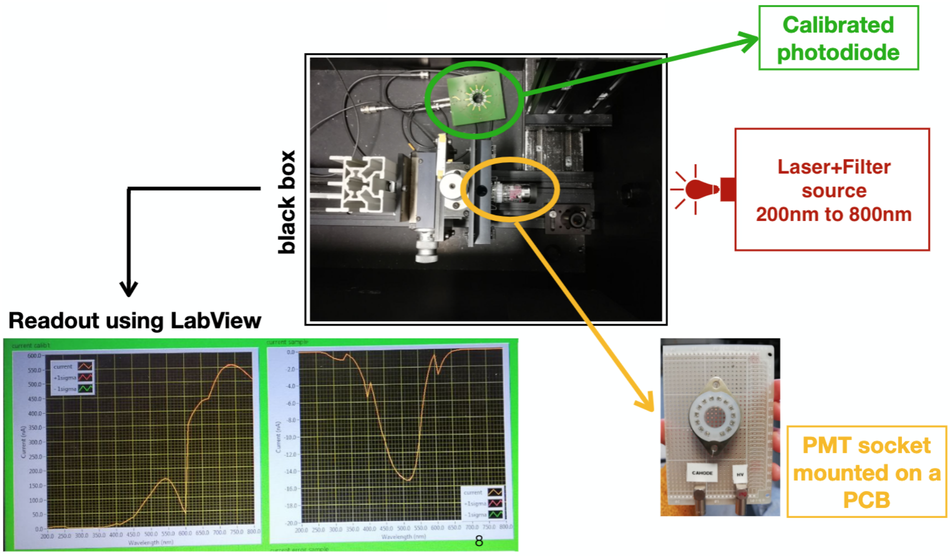

Figure 4.4: Photograph of QE measurement setup: The adjustable holding frame to fix PCB board; PMT socket PCB and calibrated photodiode and raw plot on LabView readout were highlighted.

For QE measurements, we do not need a high gain and consequently a high voltage in driving PMTs/PD, so that 230-V supply is actually used. Currents of both PMTs and the PD are recorded via a LabVIEW based software, which also controls the movement of the light source+filter system. We scan from 300 to 600 nm (range of interesting for STRAW-b) in a step of 10 nm, during which the dark current is measured ten times and averaged out. In the end, the pedestal of the current is measured in the dark.

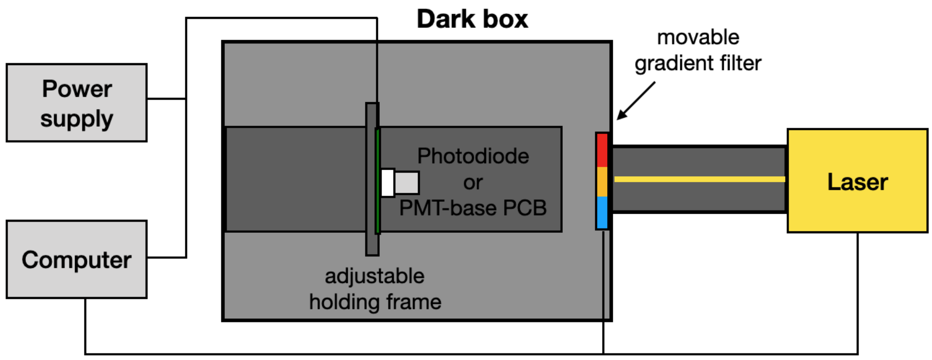

Figure 4.5: Experimental setup for QE measurement.

The light source might introduce some heating in the dark box, which might adversely affect the QE measurement. If the temperature increases, the QE value might be overestimated. To check the stability of the light intensity in time, we measured the PD current every half hour and interpolate the measurements in time (shown in figure 4.6). The result shows that the emission of the light source became stable after the first 5 minutes.

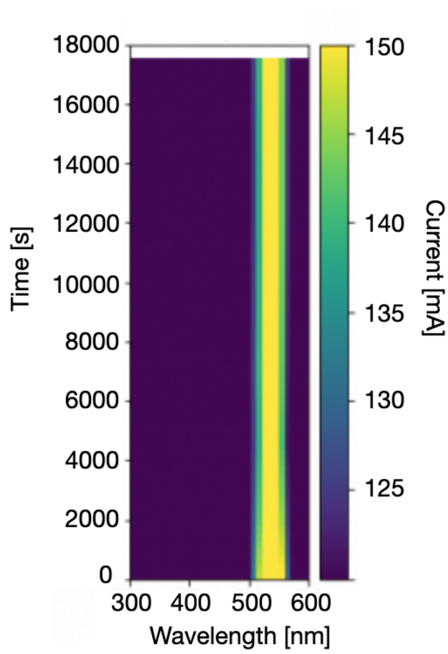

Figure 4.6: The interpolation function which starts at 0 second (first photodiode measurement) and ends after 5 hours (last photodiode measurement), shows only variations for the first few minutes, while each measurement lasted 10-15 minutes.

Then the QE of PMT can be calculated as:

$$QE_{PMT} = \frac{I_{PMT} - I_{Pedestal}}{I_{Diode} - I_{Pedestal}} \cdot QE_{Diode} \tag{4.2.1}$$

where QE_{Diode} is the QE data of the calibrated photodiode which we have already known.

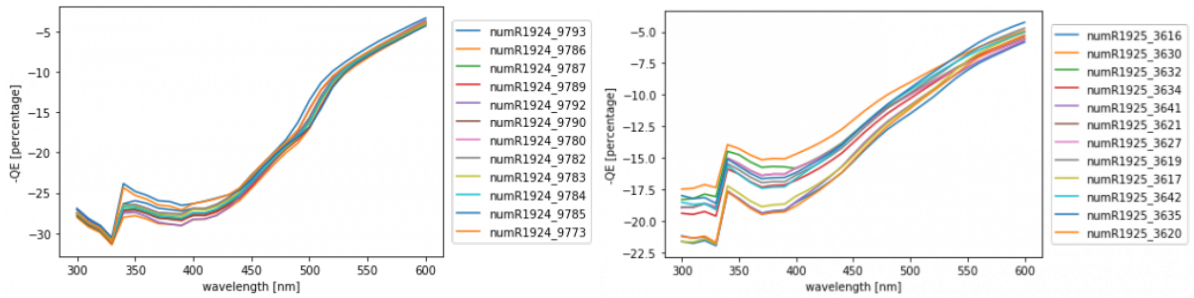

(a) QE of R1924 PMTs

(b) QE of R1925 PMTs

Figure 4.7: The QE curves of all PMTs, labeled with their serial number.

All R1924/R1925 PMTs show similar QE curve as expected (shown in figure 4.7). R1924 have better QE than R1925 series at all wavelength. The peak at 350 nm has been postulated that filter experienced a shake at 350 nm position. Due to technical difficulty, we can not disassemble this instrument to identify the cause.

4.3 Angular Acceptance on a single Filter

Hard-coated Bandpass Filters with different optical properties have been selected and placed in front of each PMT in final mounting. The most important parameters of the filters are the Centre Wavelength (CWL) and the Full Width-Half Maximum (FWHM). All available filters have different CWLs distribute in $350 - 575$ nm and FWHMs $10 - 50$ nm.

We use a tungsten lamp (white light source) and two UV LEDs (peak at 350nm and 375nm). The light from the source is collimated onto the PMT 3D-printed outer case. Inside the case, we have a removable ring to hold the filter. Behind the filter, another lens collimates the light. Following the lens, we have a piece of foamed plastic to simulate the diffusing effect of PMT glass surface. At the point where the PMT photocathode is supposed to be, we placed a HAMAMATSU mini-spectrometer which is driven by Odroid-C2 single-board computer to read out the light spectrum.

The PMT case is screwed on a motor that allows it to rotate respecting to the light source. In this way, we could vary the incident angle of the light to characterise our filters. The light source, the external focus lens, and the rotating system were aligned to the same centre axis and were placed at the position where the size of halo behind the external lens coincided with the filter size.

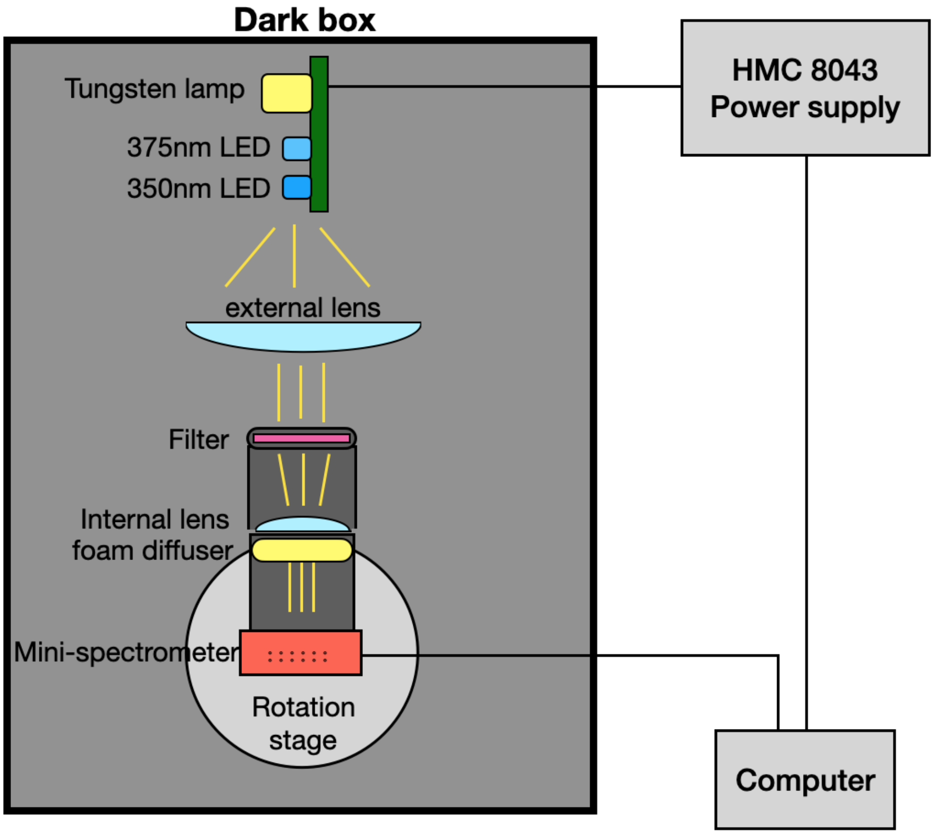

Figure 4.8: Experimental setup for the filter angular acceptance test.

As shown in figure 4.8, we measured the light transmission while rotating our 3D-printed case system from -20 to 20 degrees respecting to the normal light direction (0 degrees), with steps of 5 degrees. At each step, we recorded the light and the dark counts separately. Because the measured counts are the convolution of the filter transmission effect and the light spectrum distribution, we also recorded the light source spectrum in order to perform a deconvolution in later analysis, so that we obtain a pure filter transmission effect. The measured transmission spectrum (see fig.4.9) were fitted with a gaussian for each incident angle.

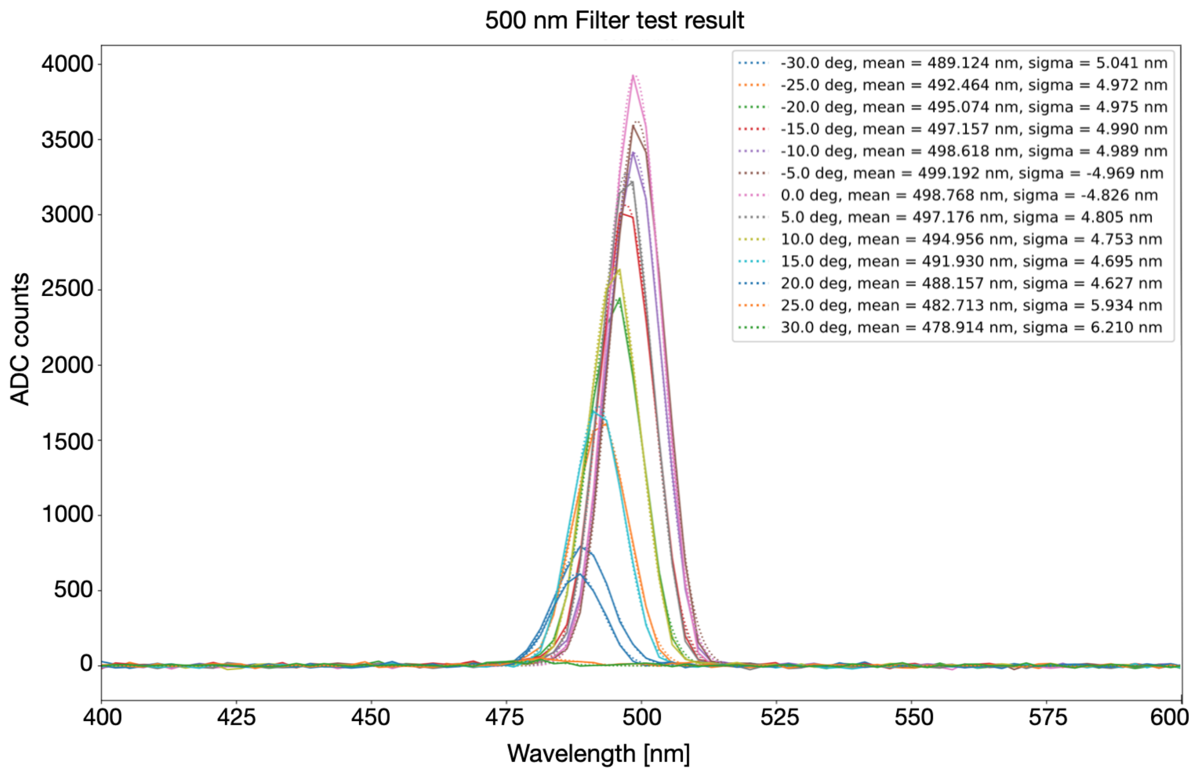

Figure 4.9: Readout from the mini-spectrometer under different rotation angle. Counts at each angle is fitted by a gaussian curve.

The gaussian distribution of intensity to the incident angle matches the theoretical expectation (which is explained in appendix A). All filters have similar transmission pattern. Because of the limitation of space, the evaluation plots of other filters will not be shown there. Data obtained here is essential for later Geant4 simulation.

4.4 Design of PMT-spectrometer Module

PMT-spectrometers are held in a rigid 3D-printed structure manufactured by Kilian Holzapfel (TUM). First, let us have an overall view of its design:

Figure 4.10: CAD design of PMT-spectrometer holding-structures. The structure is placed above the aluminium plate. A single detector unit consists of filter+Lens+PMT (upper). There are four almost identically configured substructures. Each substructure holds two HV-supply PCBs. The four substructures together fix a camera in their centre, realise the rotation symmetry(middle). According to different radial distance from centre to PMT, 12 detector units can be group by 3 difference tilt angle (lower).

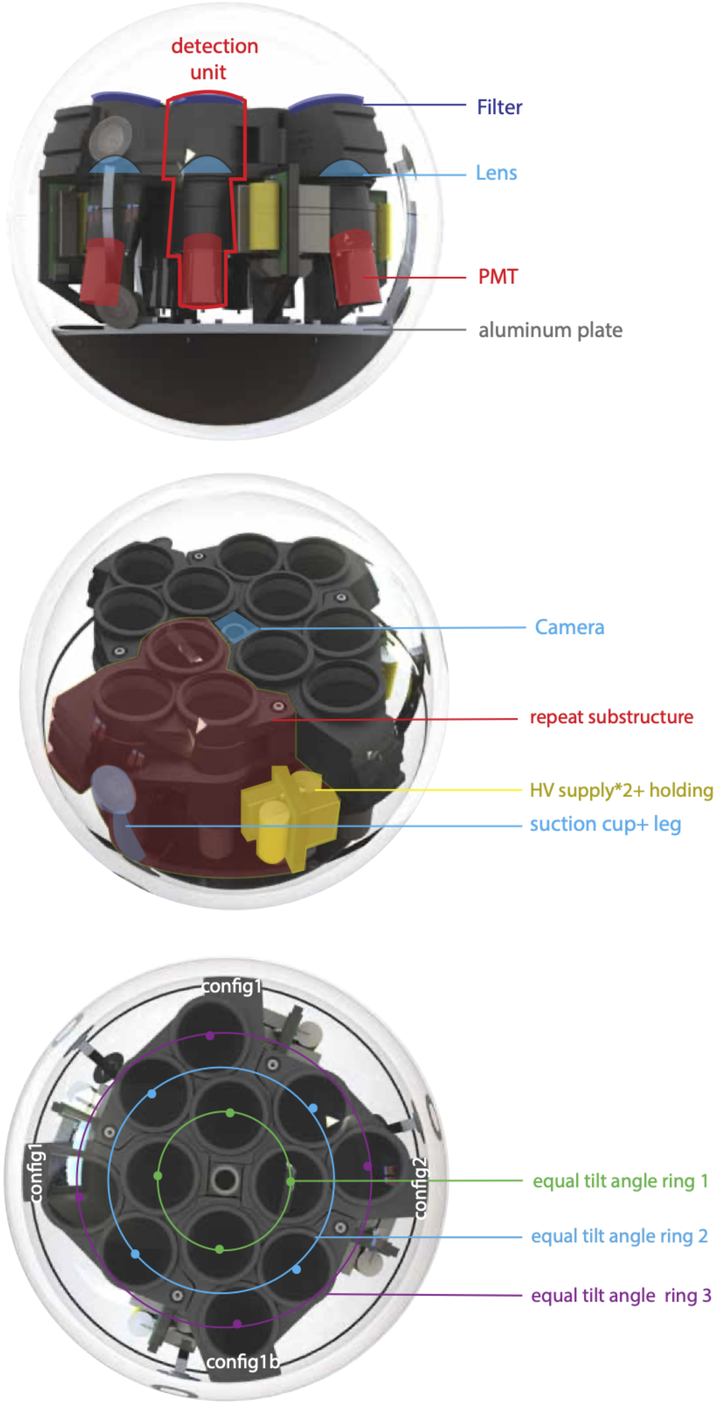

The holding-structure is designed to be symmetric. The whole holding structure consists of 4 equal sub-holding-structures, each substructure holds 3 PMTs+lenses+filters units and 2 HV-converter board (as is illustrated in 4.10, middle), so that the whole structure yields a rotational symmetry. Therefore, we have on each module 12 available positions for PMT+Lens+Filter detector units and 8 for HV-converter boards.

The PMTs are plugged in a socket[1] and connected to the ground, power supply and signal output (with MMCX connectors). The ground and the power supply wires were soldered on the HV-converter board while the signal output wires were connected to PaDaDap board for transmission to PADIWA.

On Phobos board, there is a 10-pins DAC_L (2nd to 9th-pins are DAC channels; 1st-pin is used for VCC and 10th-pin for GND) offering 0-5 V output (which will be converted to 0-1250V) and the ground. Besides, a current/power monitor can both provides a 12V supply.

We have eight High-voltage in four different positions, which makes grounding difficult as they have to share one ground connection. To solve this problem, we have designed a PCB which can distribute eight DAC channels to corresponding eight HV-boards and duplicate one single GND pin and 12 V power pin by eight-fold. Circuit schematic and its manufacturing details have been relegated to Appendix B.

The complexity of electrical connections within a PMT-spectrometer makes labelling especially important. To make distinguishable marks for every single PMT and the channel/-connector related to it, we use a label system according to the transmission sequence of the signal. There are three types of signal routes:

- Output signal: PMTs $\rightarrow$ PaDadap (input channel In0-In14) $\rightarrow$ PADIWA $\rightarrow$ TRB (TDC Website channel)
- 0-5 V control voltage: DAC_L (position 1-10, DAC channel 0-7) $\rightarrow$ HV-splitter board(position 2-9, DAC channel 0-7) $\rightarrow$ PMTs (number In0-In14)
- 12 V power supply: I2C $\rightarrow$ HV-splitter board(position 2-9) $\rightarrow$ PMTs (number In0-In14)

The expressions in each parenthesis above are the actual texts with which we label corresponding devices. To make it more clear, we have a schematic drawing of those ports and their numerical labels:

[1] Hamamatsu E2924D

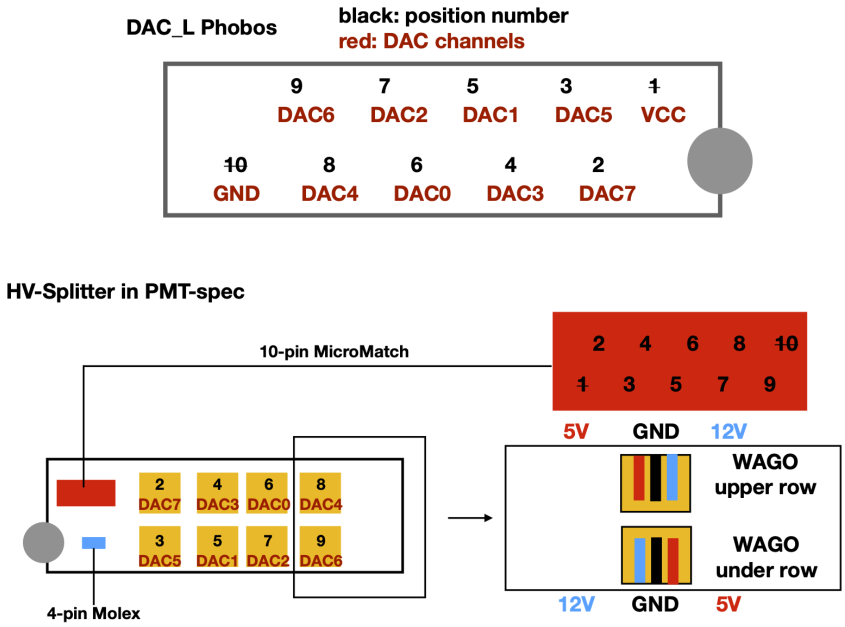

Figure 4.11: Upper diagram: DAC_L position number and corresponding DAC and GND channel numbers; Lower diagram: red square presents the pins on 10-pins MicroMatch connectors to DAC_L; the orange squares are 8 WAGO 233-503 connectors that distribute 5V+12V+GND line to each PMT, on the 233-503, we use three different colours to distinguish the position to connect 3 PMT socket wires; the blue square is 4-pin Molex connector that load 12V power; Grey circle is the visible mark that helps users easily recognise the orientation of connectors.

Each DAC channel has 12-bit storage for output value which corresponds to a resolution of 4096. The output range of voltage is 0-5V, then the accuracy of HV control on PMTs is $1250V/4096 \approx 0.3$V. In Ideal condition, all PMTs should work under the same gain and use as low as possible voltage supply to maintain low dark rate. To locate this operating condition, we plot the gain curves of the two PMT series from 4.1 together:

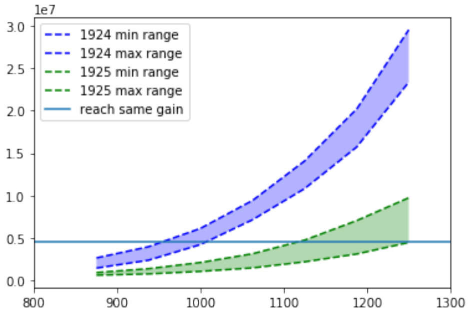

(a) Gain of R1924/R1925 PMTs, the minimal same gain values they can reach at 0.53e7

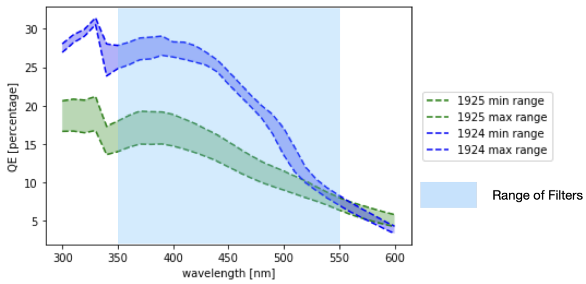

(b) QE of R1924/R1925 PMTs

Figure 4.12: For two different types of PMTs, we plot their ranges of gain (left) and ranges of QE (right) together. In order to find the lowest voltage they need to reach the same gain value.

There are two identical PMT-spectrometer modules. The voltage values of all PMTs where they each has a gain of 0.53e7 were recorded. We choose 24, out of 32, PMTs consisting of 16 R1924 PMTs and 8 R1925 PMTs with the highest gain. Those 24 PMTs need to go into $8 * 2 = 16$ HV-converter board. Therefore, 8 PMTs are stand-alone and other 16 PMTs need to be paired. Two PMTs working under similar voltages are paired. The choices of stand-alone and paired PMTs are listed here:

DAC channel	Module number	Serial number	Voltage[V] to reach 0.53e7 of Gain
0	1	AJ9780 AJ9785	989.5
0	2	AJ9777 AJ9779	995.6
2	1	AJ9787 AJ9778	1007.7
2	2	AJ9792 AJ9784	1022.3
6	1	AJ9775 VA3617	1191.9
6	2	AJ9793 VA3619	1128.5
7	1	VA3627 VA3616	1126.7
7	2	VA3621 VA3618	1147.0

Table 4.1: stand-alone PMTs and their DAC channel, Module number and serial number, voltage need to achieve 0.53e7 Gain.

DAC channel	Module number	Serial number	Voltage[V] to reach 0.53e7 of Gain
3	1	AJ9780	1003.4
		AJ9786	1004.4
3	2	AJ9777	1011.5
		AJ9783	1012.9
1	1	AJ9787	1014.1
		AJ9789	1015.2
1	2	AJ9792	975.9
		AJ9790	977.1
4	1	AJ9775	981.9
		AJ9782	983.5
4	2	AJ9793	998.7
		AJ9773	1000.2
5	1	VA3627	1247.2
		VA3634	1247.2
5	2	VA3621	1237.2
		VA3641	1241.9

Table 4.2: Paired PMTs and their DAC channel, Module number and serial number, voltage need to achieve 0.53e7 Gain.

We need 14 filters with different CWL/FWHM to completely cover wavelength in a range of $350-600$ nm, as shown in figure 4.13. To keep the symmetry of PMTs holding structure, we have 12 positions to fill in the detector units. We decide to keep one out of 12 PMTs operating without filter to get the integrated signal and check for the existence of light whose wavelength is outside of $350-600$ nm. Then 11 filter positions remain for each module, 11*2=22 filters from 14*2=28 filters (each type has two samples) need to be chosen. In other words, 6 filters need to be given up. We consider several factors that affect light transmission in $350-600$ nm:

i Absorption length in (pure) water.

ii Absorption length of BK7 glass sphere.

iii Quantum efficiency of PMTs.

iv FWHM of filters.

Then we have the following expected light distribution on all filters:

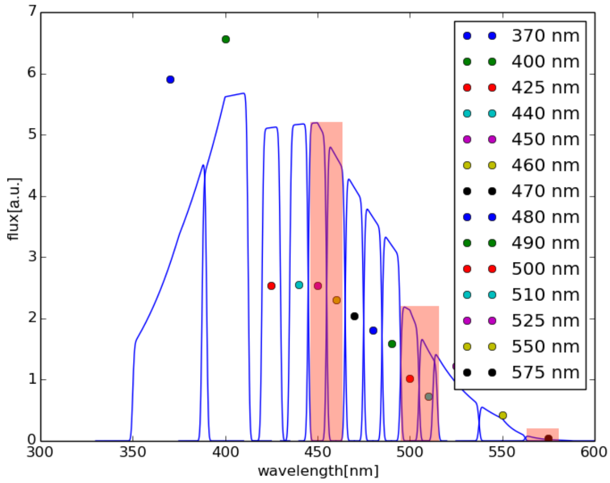

Figure 4.13: Expected light distribution on PMTs in the deep sea environment. The blue curve is the flux of light in arbitrary unit. The coloured spots are the integrated flux of corresponding filters. The red shadows cover the wavelength positions where we decide to leave out.

First, 575 nm filter should be totally left out because of light at this wavelength is too weak. We must keep 350 nm filter because UV-light is more common than red-light in Cherenkov emission, so it is important to have UV-emission data. Second, we see there is a small overlap between 500nm and 510nm, so we decide to use a 500 nm Filter in one of two PMT-spectrometer modules and use a 510 nm Filter in the other module. In accordance with the same rules, we use a 450 nm Filter in one module and a 460 nm Filter in the other. Since 450 and 460nm are in the middle (instead of beginning or end) of the spectrum, we can still recognise the spectrum's contour.

The next task is to decide how to combine PMTs with different gains/QE to the filters, and the position to place each PMT+lens+Filter unit on PMTs holding-structure. The decision follows the principles:

i At two symmetric positions, the CWLs of two filter should be similar. The whole CWL distribution on holding-structure should be as symmetric as possible.

ii The filters with similar CWLs should be placed as far as possible between each other.

iii filters with short CWL should be placed at the centre because intensity of Cherenkov light is strong in short wavelength and centre positions usually can receive most of light.

iv PMT without filter should be placed at edge.

v high-gain and high-QE PMTs should combine with those filters, whose CWL locates at low-intensity part of the spectrum in 4.13 for compensation. "No filter" position could use the "worst" PMT because of high counts on this channel.

After then, the schematic 2D-view of PMT-spectrometer looks like following (with a table of connections to DAC channel and PADIWA channel):

The configuration of all elements inside a PMT-spectrometer module is shown in figure 4.14:

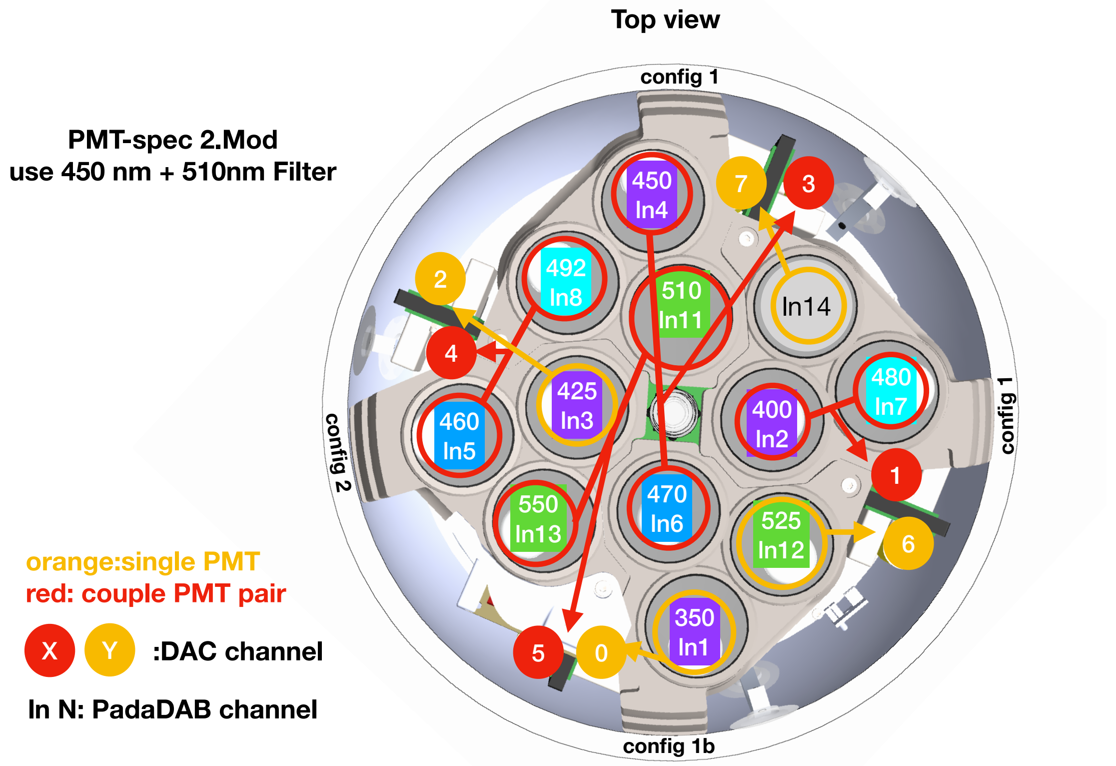

Figure 4.14: Viewing from the top of the module: PMTs, filters and HV boards in final configuration.

CWL of Filters	PMT Type	TRB Website channels	DAC_L Channels	PaDaAdap Channels	Serial number of PMTs in 1.Mod	Serial number of PMTs in 1.Mod	DAC_L input_value (real voltage)	DAC_L input_value (real voltage)
350 nm	1924	15	0	ln1	AJ9785	AJ9779	3957 (989V)	3980 (995V)
400 nm 480 nm	1924	13 3	1	ln2 ln7	AJ9787 AJ9789	AJ9792 AJ9790	3326 (1015V)	3908 (977V)
425 nm	1924	11	2	ln3	AJ9778	AJ9784	4061 (1007V)	4089 (1022V)
450 m, 470 nm	1924	9 5	3	ln4 ln6	AJ9780 AJ9786	AJ9777 AJ9783	4017 (1004V)	4048 (1012V)
460 nm 492 nm	1924	7 1	4	ln5 ln8	AJ9775 AJ9782	AJ9793 AJ9773	4055 (983V)	4001 (1000V)
510 nm 550 nm	1925	12 8	5	ln11 In13	VA3627 VA3634	VA3621 VA3641	4990 (1247V)	4966 (1241V)
525 nm	1925	10	6	In12	VA3617	VA3619	4765 (1192V)	4913 (1228V)
No Filter	1925	6	7	ln 14	VA3616	VA3618	4505 (1126V)	4590 (1147V)

Table 4.3: Table of all connection positions and Filter, PMTs, HV information at corresponding positions.

4.5 Geant4 Simulation of the PMT-spectrometer

Geant4[2] is a particle physics simulation toolkit developed by CERN. We use this tool as a ray-trace to simulate the optics of the whole PMT-Spectrometer. The details on the construction of geometry, materials of the detector, optical processes and primary particle source are defined as close as possible to reality, here we only mention the most important factors:

i Light source: Source position is placed at the edge of a 50 m radius water sphere. It generates photons in the wavelength range between $350-550$ nm following gaussian distribution with σ = 10 nm gaussian distribution. The photons propagate from the source position towards module with a specific pre-defined angle: zenith = 0.0/2.5/5.0/7.5 degree and azimuth = 0.0/10.0/20.0 degree.

ii Material: we adopt default G4Glass material for the filter, BK7 glass for the glass sphere and the lenses. Aluminium material is used for the aluminium plate and the electronics mounted on it, as well as for the PMT outer shields cases. We place then water as the outside global environment. Volumes of the filters are set as tracking volume to track photons' incident angle. Volumes of the PMTs are set as detect volume to determine the valid detection.

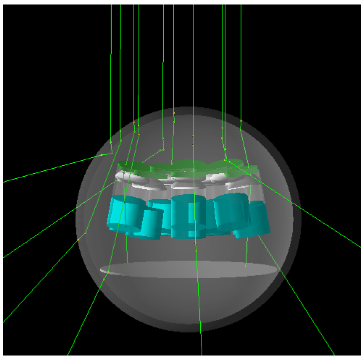

Figure 4.15: Visualisation of the PMT-module in OpenGL viewer, with 10 events. In the simulation we usually generate 10000 photons.

Only the photons hitting both on the filters and the PMTs will be recorded in the output file. For those events, the output file stores their hit position on PMTs, wavelength, incident angle(zenith/azimuth) on filters and other useful information.

Tilt angle of detector units (PMT+lens+Filter) is an adjustable parameter in the design. Because the glass sphere has focus effect, the light coming from directly above the module will hit on PMTs with a certain deflection angle. The tilt angle ensures that the PMTs can receive the maximum of light. To find this angle, we first placed all detector units straight upward, then generated 10000 photons.

[2]https://geant4.web.cern.ch/

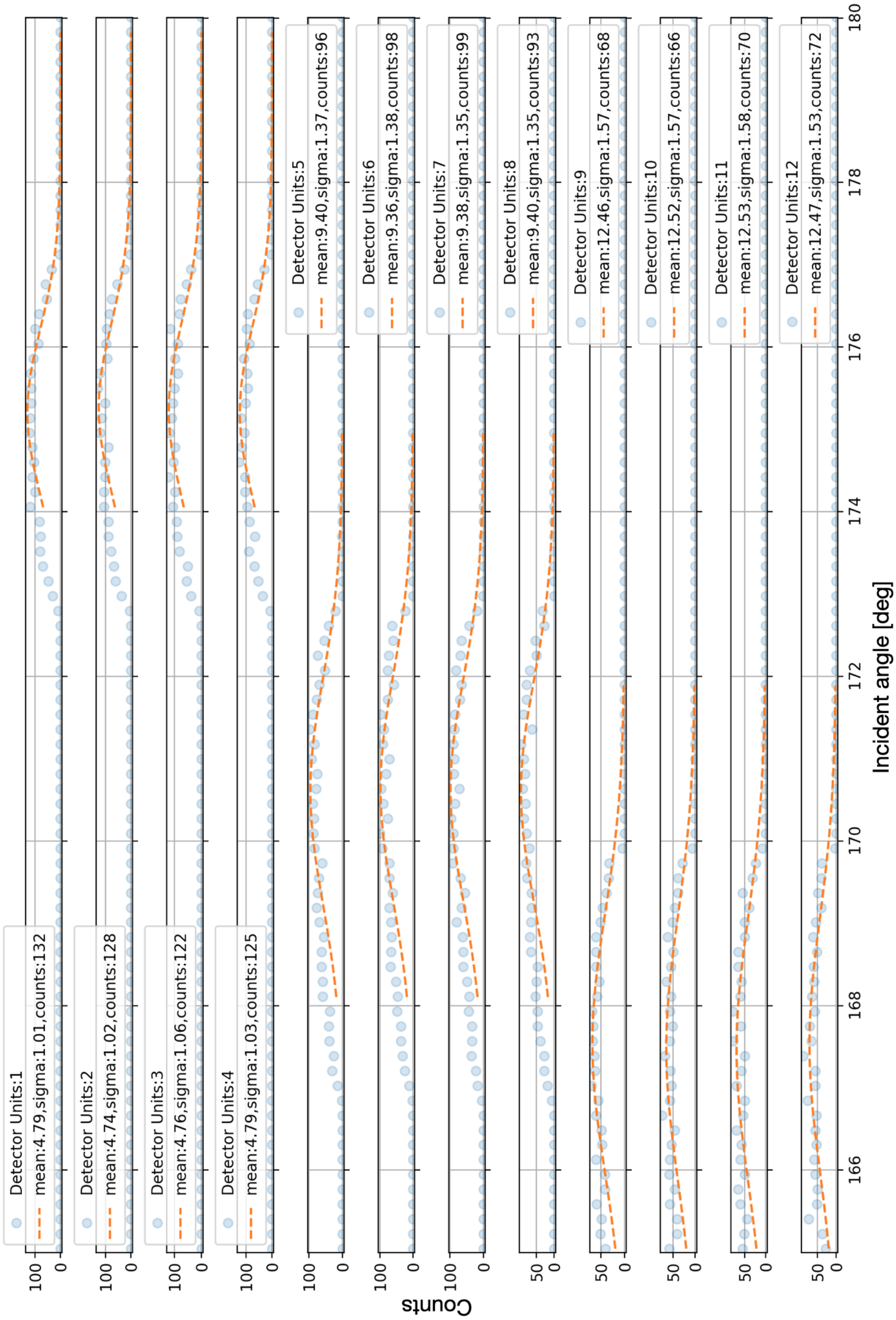

Figure 4.16: Hit-counts-to-angle distribution of all detector units obtained from the simulation. The 4 units belonging to inner/middle/outer group have same behaviours. light blue spots are counts at certain degree, orange lines are gaussian fit curve.

Detector units that have the smallest distance to the centre are located on the same ring (as shown in 4.10). These four detector units can be seen as an “inner group”. The 4 detector units having the largest distance to centre belong to “outer group”, while the rest 4 detector units belong to "middle group". The detector units in the same "group" should have the same tilt angle toward the centre.

From the counts-incidental-angle distribution of each detector unit in figure 4.16, we can see that the PMTs in the same group have the similar shape of gaussian distribution, and the peaks of gaussian are not at 0/180 degree. To obtain as many events as possible, the z-axis of the detector unit should tilt inward with the specific angular corrections, which corresponds to the peak position of each hit-counts-to-angle. Therefore, from simulation we fixed that “inner group” should tilt 4.75 inward, and 9.38 for the middle group, 12.50 for the outer group respectively.

The distance between the lenses and the PMTs is also an adjustable parameter. It can affect the size of “light spot” on the PMT’s glass surface. To study this effect, we plot the hit-counts-position distribution, keeping other parameters unchanged except the distance between the lenses and the PMTs. This distance is decided to be 30 mm to make sure that any “light spot” (see figure 4.17) will totally fall onto the PMT glass surface.

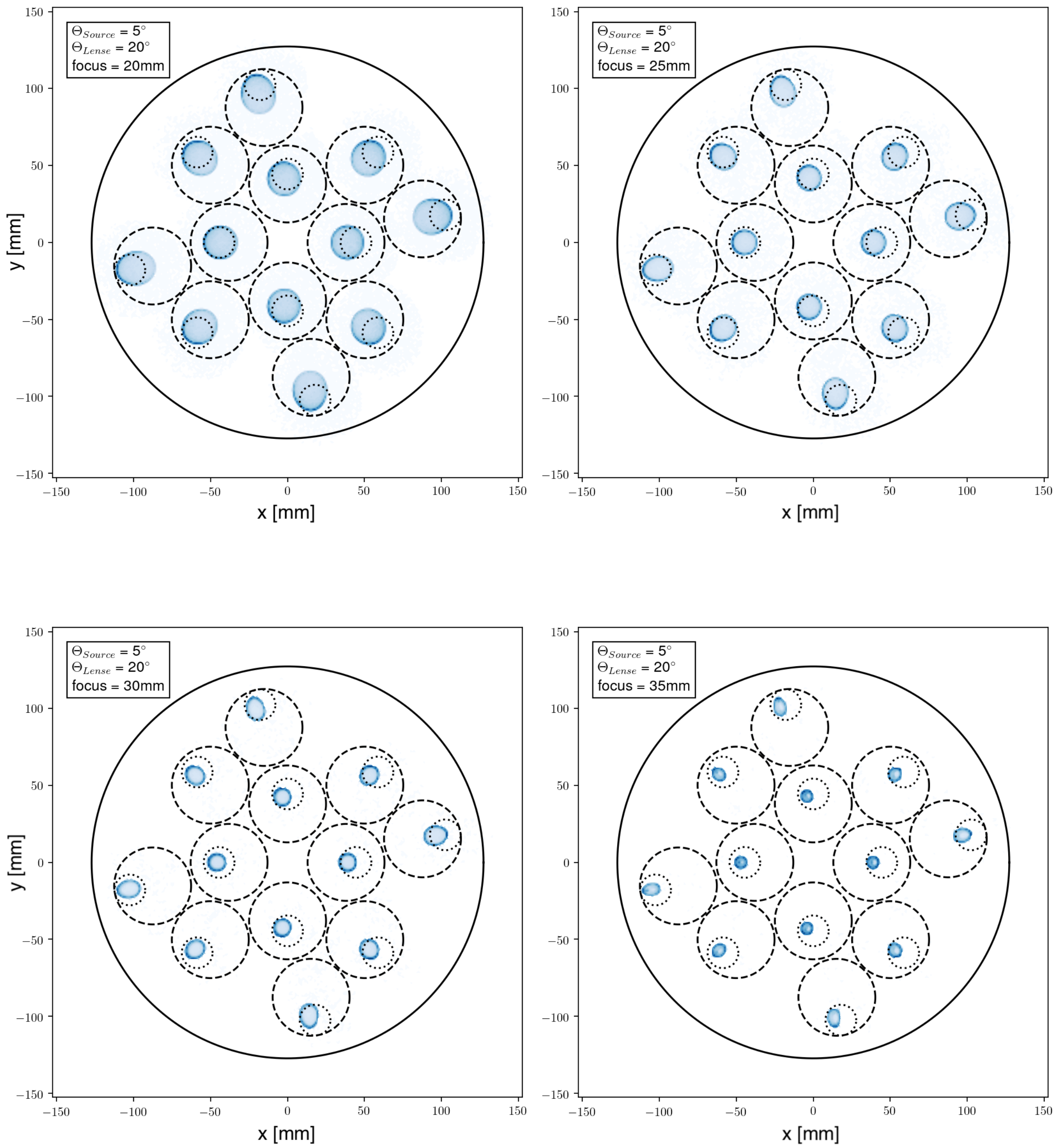

Figure 4.17: Source position and its zenith/azimuth angle keep unchanged. The distance between the lenses and the PMTs varies from 20 mm to 35 mm. The blue circles show "light spot" on the detectors. The colour gradient from light to dark stand for quantity of counts from more to less. Outer dashed circles are the areas of filters; Inner point-dashed circle are the areas of the PMT glass surfaces.

The expected count rate is an important number that need to be studied within the simulation. As we see in the filter test, the light intensity on a single filter decreases as the light incidental angle increases. Here we also plot the photon counts on each detector unit as a function of the source's zenith angle to examine if this effect is also visible for the whole module.

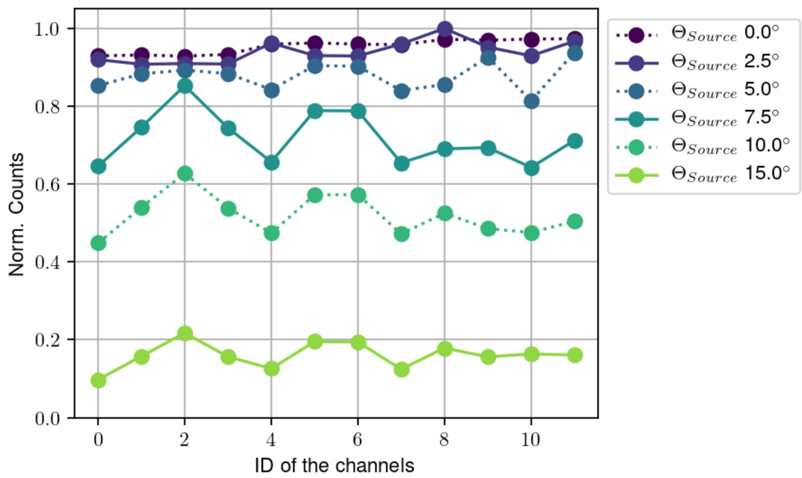

(a) Normalised counts (divided by maximum counts of single detector unit) on each detector unit to different zenith angle of source.

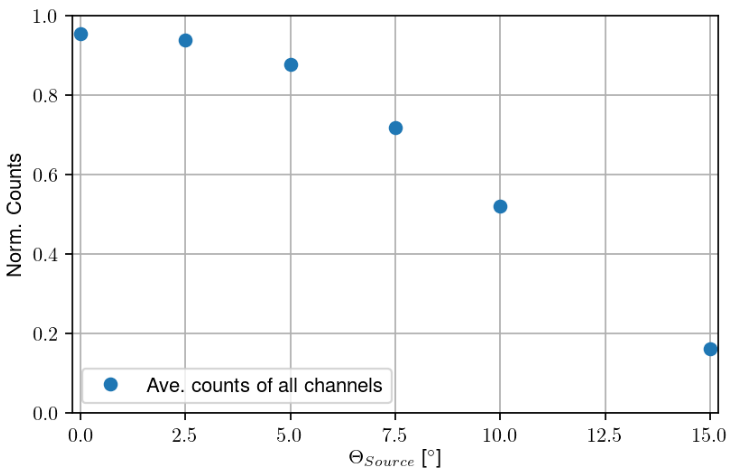

(b) 12 detector units averaged and normalised (divided by maximum counts on single detector unit) counts to different zenith angle of source.

Figure 4.18: Effects of the source's zenith angle (namely photon incident angle) on the number of hitting photons.

In figure 4.18 we see the detection efficiency remains above 60% for zenith angles smaller than 7.5 degrees. Then the detection efficiency decays rapidly and approaches zero for zenith angle larger than 15.0 degrees. Under the same zenith angle, the counts at each detector have only small fluctuations. The average count rate from the second plot shows that the count rate decreases with the increasing zenith angle and follows a gaussian distribution. The behaviours of the whole module are in our expectation.

4.6 Dark Box Rotation Measurement of the Module's Prototype

During this thesis we designed the PMT-Spectrometer holding structure according results of our simulation. We mounted the whole prototype to a rotation stage inside a long dark box with all filters pointing to the direction of a halogen light source, to examine the real behaviours of each detector units under rotation. A photodiode is mounted inside the dark box to monitor the possible light fluctuation.

We control the rotation stage to turn from -60 to 60 degrees (in zenith) with certain steps. For each step, we monitored PMTs'count. The test procedure is:

i First, we assemble the module without filters or lenses but only PMTs. Then we scan rapidly from -60 to 60 degree in a step of 1 degree. For every step, we measure PMT counts once.

ii We assemble the module with lenses and PMTs but no filters, repeating the rapid scan as described above to check the effects of lenses.

iii Finally, we assemble the module completely (PMT+lenses+filters) and scan from -60 to 60 in a step of 1 degree. Every step we take PMT counts measurement 60 times, temperature/pressure/humidity sensor once, photodiode once. These final measurements will repeat for 0/45/90 degrees of azimuth angle.

iv For later crosstalk check, change to the LED light source.

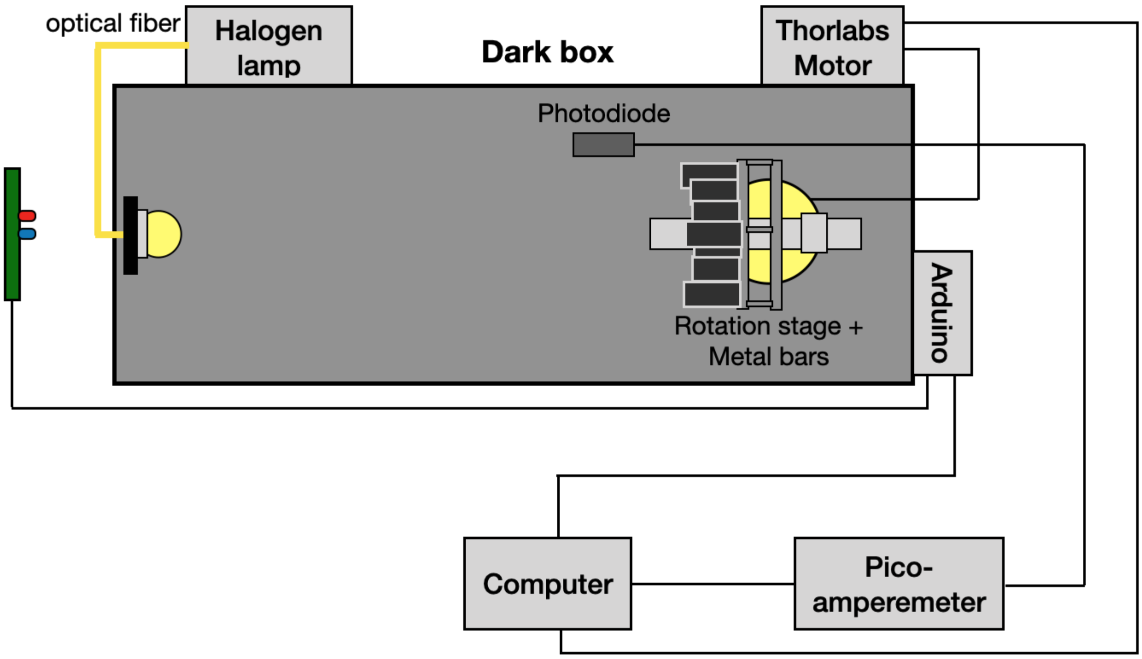

Figure 4.19: Experimental setup of the dark box rotation test

It is worth mentioning that both halogen light and the LED are too bright and the PMTs saturate. To reduce the intensity and diffuse the light, we placed one layer of 0.5% transmission foil in front of the halogen light source and two layers of this foil in front of the LED light source. Because the relative magnitude of counts instead of the absolute counts is interested in the measurements, there is no need to consider the effect of the foils in the data analysis.

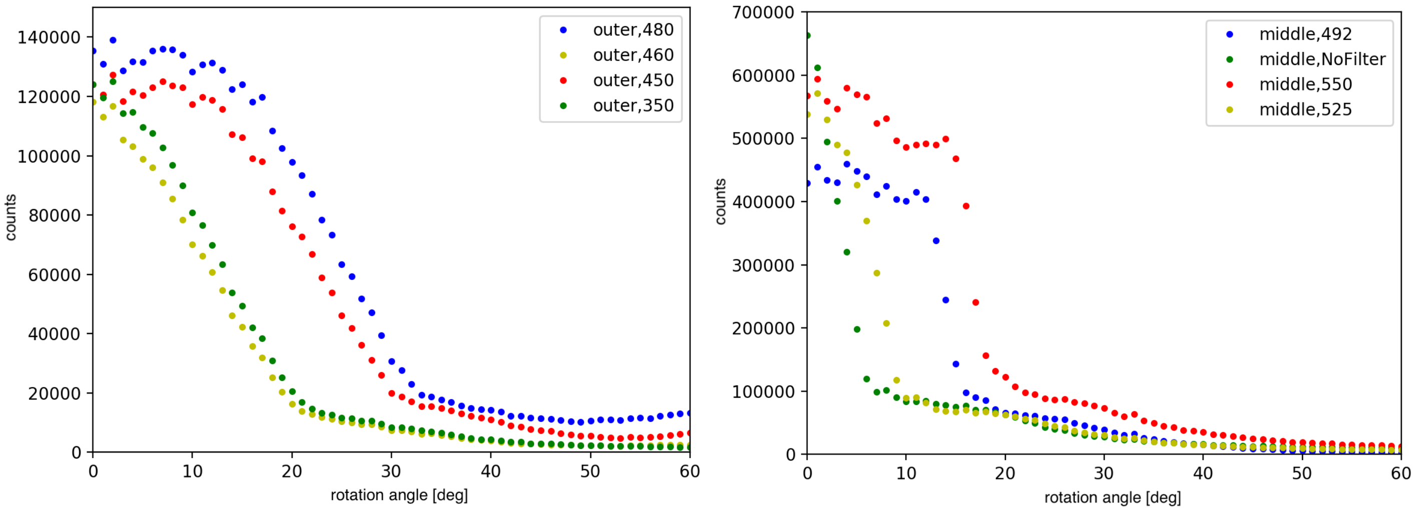

(a) only bare PMTs

(b) PMTs combined with lenses

Figure 4.20: Angular distribution of counts shows effect of lenses.

In figure 4.20, we expected the bare PMTs condition, intensity-to-rotation angle curve is a quasi gaussian distribution and we observed they gaussian distributed. After adding lenses, gaussian distribution drops rapidly at 15 degrees because the focus effect of the lenses cut down the photons outside its acceptance. This behaviour is already confirmed by Geant4 simulation.

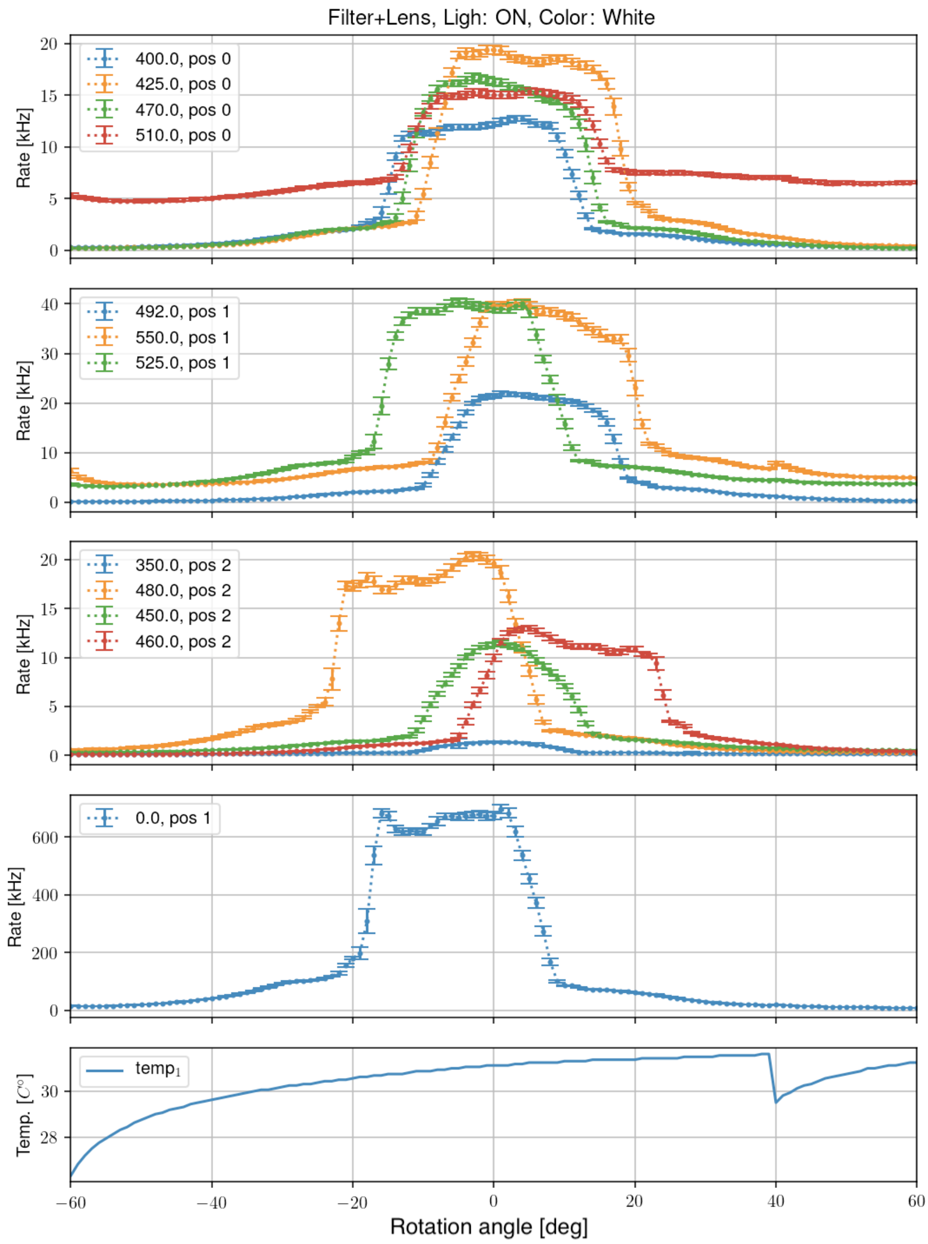

Figure 4.21: Angular distribution of PMT counts after integrating filters. From the first to third rows, which have the labels of Pos 0/1/2, the results of detector units on inner/middle/outer ring are presented. The detector unit has no filter stands alone in the fourth row because of its high counts. The last row presents the records of temperature sensor records stuck to a PMT. It drops at 40 because measurement has a pause at this time. In general, rising of temperature did not has a big effect on dark counts.

After the integrating of the filters, as shown in figure 4.21, the light distribution was

reshaped to quasi-uniform distribution. All filters have an open window around 20 degrees. The counts distribution of the inner group are almost symmetric to zero degree, while the distributions of middle and outer group move away from zero position. The empty (without filter) position has 30 times more counts than the position with filter because of the optical density of filters.
This measurement was also done for the second PMT-spectrometer module, and its behaviours are as same as the first module. The behaviours of whole modules are within our expectation.

4.7 Crosstalk Check

The crosstalk effect happens more possibly when various PMTs are operated very closely and have a high gain[38]. We studied if the crosstalk is presenting in the PMT-spectrometer module and how it could potentially reduce the measurement accuracy. Therefore we test PMTs' behaviours under a monochromatic LED emission. The reason why we use this light source is that the crosstalk could be easily seen if only one channel responds strongly.

Everything, except for a change of light source into the blue/red LED, is identical to those used in the previous dark box rotation test. LEDs are remotely controlled by Arduino, which will first switch on red LED (CWL 650nm, FWHM 100nm) for 10 seconds, then blue LED (CWL 480nm, FWHM 20nm) for other 10s, finally followed by power down of all LEDs for 10s. For all three lighting conditions, we recorded HLD data and repeated this measurement 5 times.

The nanosecond precise time information is recorded in HLD data. Fo every single photoelectron, its received channel, timestamp of rising/falling can be extracted. Usually a single photoelectron signal will have a length of 10 ns ($= t_{rising} - t_{falling}$), so in the analysis we delete those events whose $t_{rising} - t_{falling}$ is larger than 100 ns. We count the rising edges number for each channel and plot them in histograms of 5 ns bin-width.

The channel with largest counts is the main channel (used for time reference in analysis), which could lead to crosstalk in other channels. We pick up every position of gaussian peak in the main channel as a start point. Aligning to this start point, we divide time-axis of all other channels into intervals of 200 ns (in this time interval, crosstalk should have happened).

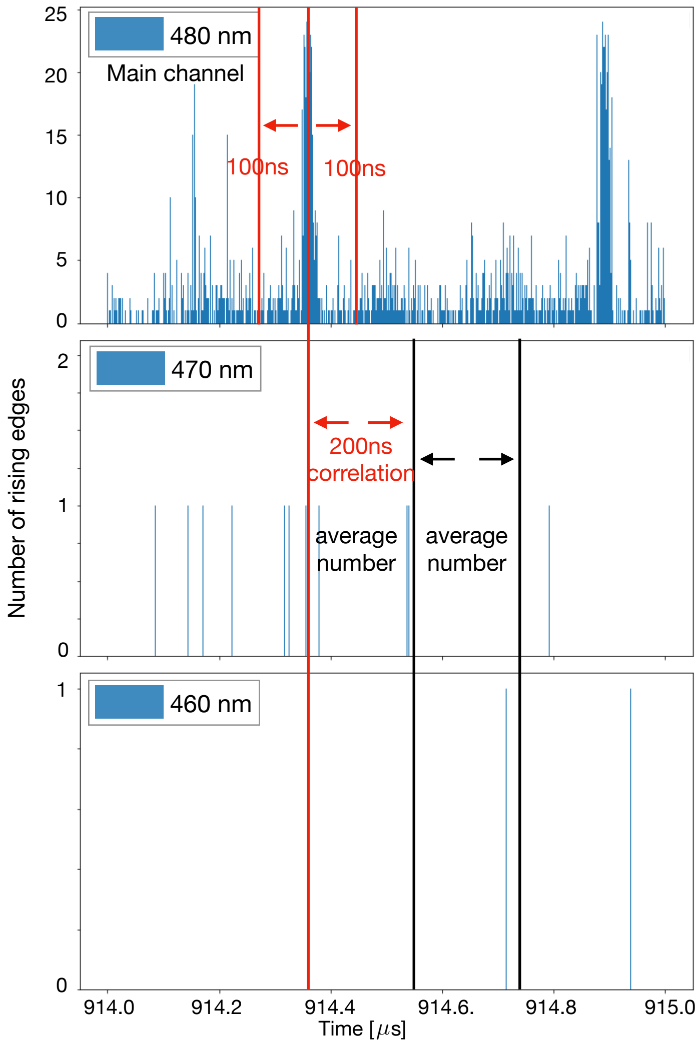

Figure 4.22: Number of rising edge - time interval histogram. Here only several milliseconds for blue LED are shown figure while seconds long data were analysed. Main channel and two channels that have similar CWLs to the main channel are shown. Upper left labels present the CWL of filters. Red lines select the first 200 ns interval starting at a peak in the main channel, where both correlations between channels and average number are calculated. Black lines select the second 200 ns intervals, where only average is calculated.

There are two signs indicating the existence of crosstalk to be check (which is illustrated in figure 4.22): 1. In other channels, event number average inside first or second 200 ns is higher than overall average 2. There is a strong correlation between ± 100 ns interval in the main channel and the first following 200 ns interval in other channels.

To check this, we calculate the average number inside 200 ns interval and compare them with the overall average. If it is higher than overall average, then we calculate the pairwise correlation r-value between all channels. The results were listed in table 4.4. Since r-values are overall smaller than 0.1, we could ensure there is no crosstalk between the PMTs. Because there is no previous measurement on multi-PMTs' crosstalk, we take crosstalk between SiPM as a reference. Crosstalk events happened between SiPM pixels has a typical probability higher than 10% [39] (once crosstalk event of every ten single photoelectron events). The signal causing by crosstalk can reach 1-2 times of single photoelectron amplitude. None of the two features was observed in measurements.

Channel	1	3	5	6	7	8	9	10	11	12	13	15
1	1	0.061	0.038	-0.014	0.0062	-0.040	0.030	-0.09	-0.04	-0.002	-0.008	0.0002
3		1	-0.008	-0.014	-0.033	0.017	0.008	0.045	-0.068	-0.047	-0.017	-0.034
5			1	-0.006	-0.001	-0.024	0.013	0.013	0.037	-0.018	-0.007	-0.030
6				1	0.001	-0.023	-0.007	0.035	-0.018	0.003	0.021	0.006
7					1	0.038	-0.014	0.003	-0.008	0.007	-0.004	-0.012
8						1	-0.059	0.001	0.027	-0.022	-0.002	0.025
9							1	0.024	-0.002	-0.010	0.017	-0.038
10								1	-0.015	0.025	0.014	-0.002
11									1	0.038	0.037	0.043
12										1	0.051	0.022
13											1	-0.005
15												1

Table 4.4: Correlation table for all channels. The correlations between every channel calculated by **scipy.stats.stats** function **pearsonr(channel X, channel)**, are too small and can be ignored. In the SiPM array typical crosstalk efficiency varies between 10% to 60%.

4.8 Simulation of Dark Box Rotation

A Geant4 simulation was also done for the dark box setup to compare with the real experiment. Besides, if Geant4 simulation can well reproduce the dark box behaviours, it demonstrates the reliability of in-water simulation.

In this simulation, we use a light source generating 10000 photons, which distribute uniformly in $350-600$ nm; an aluminium dark box shell and an air world. We also take reflections at dark box shell into account.

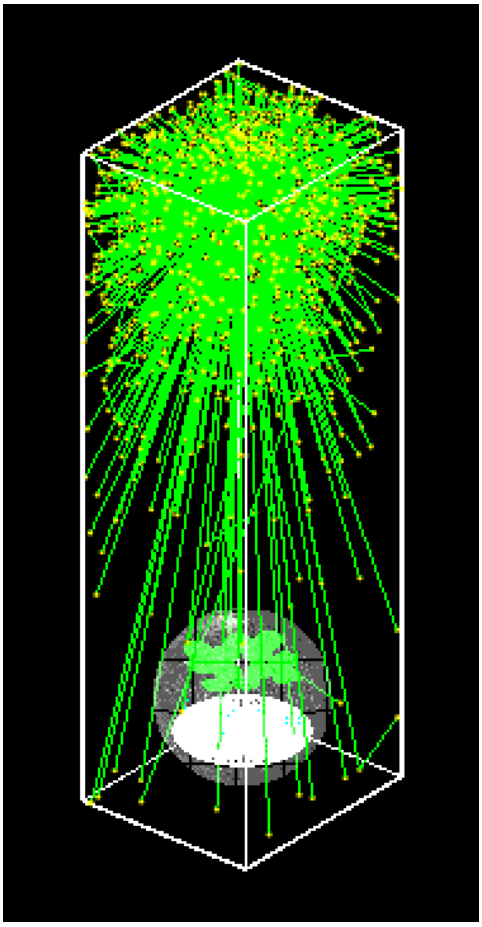

Figure 4.23: Geant4 dark box geometry with 100 photon events. The size of the box is 140cm×45cm×45cm. The position of the light source is as same as in reality. From visualisation we can see most photons were absorbed and a few were reflected by the dark box shell.

The centre of the whole simulation space is located in the centre of the glass sphere. The z-axis of rotation space is as well as the z-rotation-axis of glass sphere. We run the simulation 121 times. Each run corresponds to a one-degree step of scanning through the rotation angle -60 to 60 degrees. In each run, the dark box-light source system rotates in z-x-plane with this rotation angle while glass sphere-module system stays fixed. The photon incident angles on filter have been converted into the glass sphere's frame of reference.

It is hard to integrate the effects of the filters into Geant4. Therefore, we modified on filter registered counts in Python analysis. According to measurements in section 4.3, we know the CWL and FWHM of the filters, as well as how the intensity of photons is weakened at certain incidental angle. After introducing those effects, the results of the dark box rotation simulation are shown in figure 4.24:

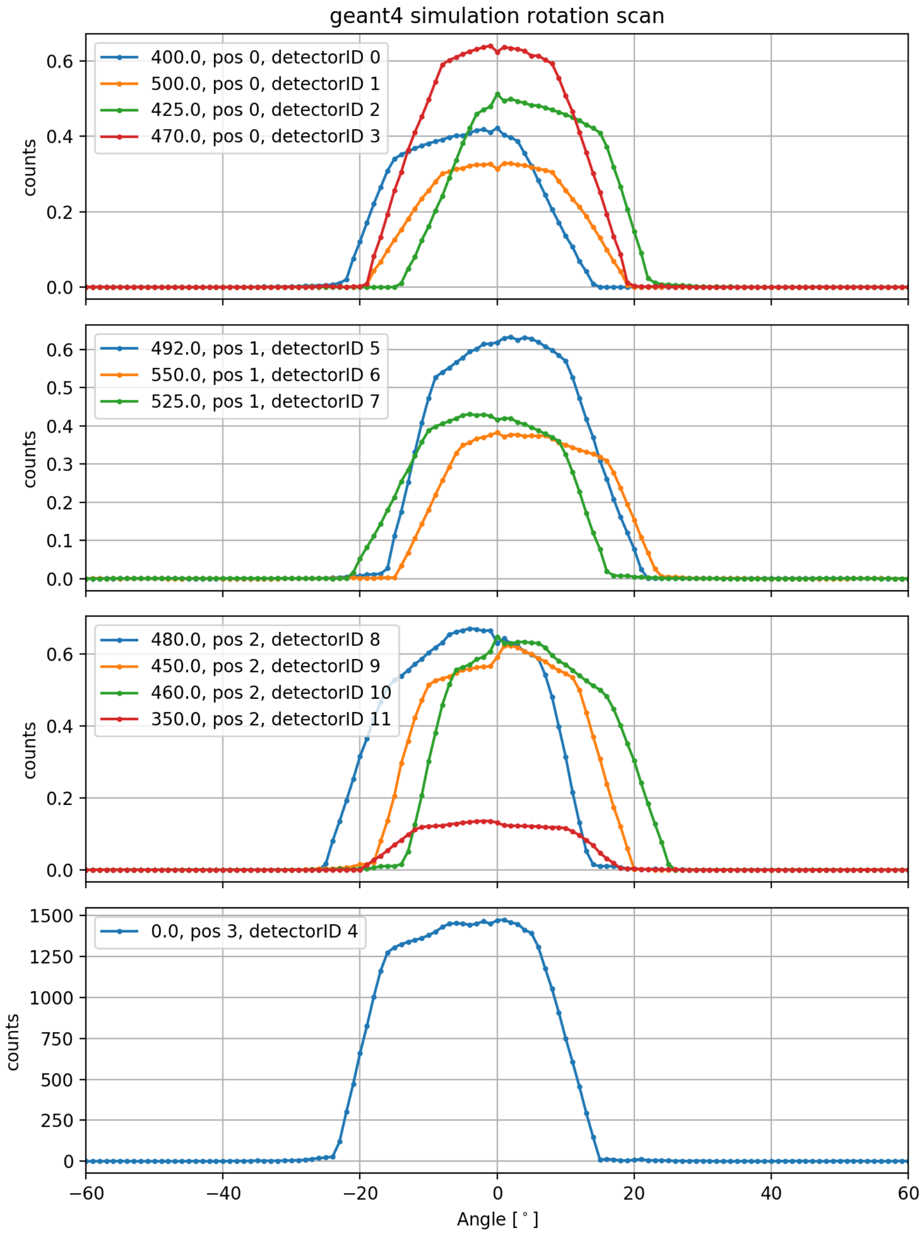

Figure 4.24: After considering all factors that can affect the intensity, all filters show a "uniform windows" distribution. The unit of counts is arbitrary since only the ratio between the counts is important. Detectors 0-3/4-7/8-11 are on inner/middle/outer ring. All detectors have similar counts except no-filter one. The result is reasonable.

The 10000 photon number in simulation is far below the real scale. To properly compare with real measurement, simulation counts were modified. It first multiplies by the shape of the halogen lamp spectrum and then by the rescale factor of N_{real_max}/N_{sim_max} in each channel, so they have comparable height on the y-axis. After modification of number, we plot simulation and measurement in the same figure 4.25:

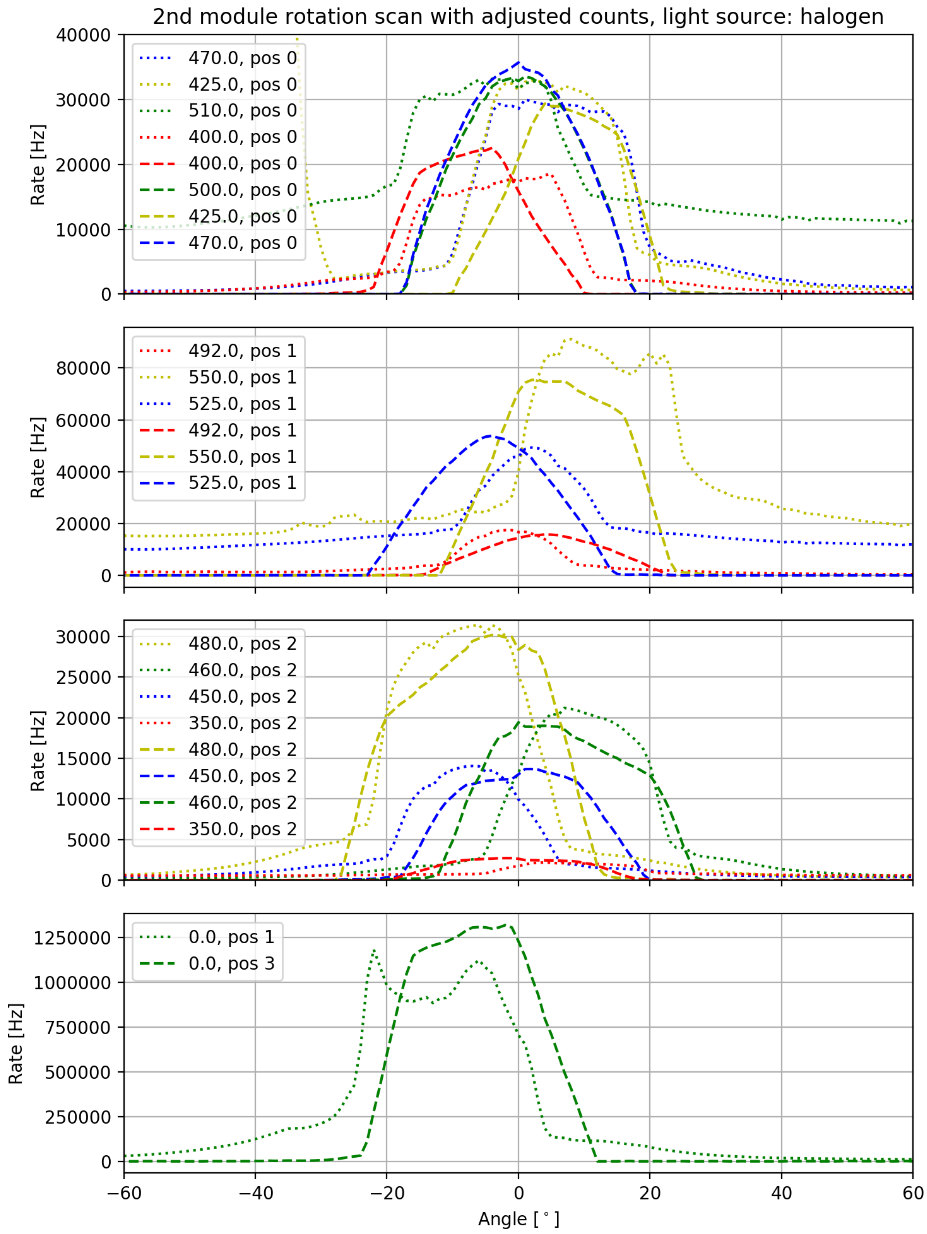

Figure 4.25: Combine Geant4 simulation with experimental measurements. Dashed curves are results from the experimental setup; Dotted curved are simulated results with modified counts.

In the combined plot, the simulation and measurement at some filter's positions are matched perfectly (400/425/460/480/492/525/550/0), some of them have either position mismatch (350/450) or shape mismatch (470/510). The reason for those mismatches is because in both geometry and optics reconstruction, we can only approach the reality but not totally reproduce it. For example, we use a simple cylinder for the 3D-printed holding structure for the PMT, but in reality, it has a hyperbolic section. However, the compatibility between measurements and simulations is already good.

4.9 Mini-spectrometer and Camera integrated within the PMT-spectrometer

A mini-spectrometer is mounted at the same height as the filters just beside HV-supply-board 0&5. An astronomy camera is held in the centre of PMT-holding-structure. We have taken several measurements of these two devices within the same setup in figure 4.19. As explained earlier, Mini-spectrometer and Camera are expected to complement PMT at high intensity, in which PMT will saturate, but Mini-spectrometer and Camera will not. Mini-spectrometer was illuminated with the same blue and red LED as those in section 4.7. The measurement shows a sensitivity of Mini-spectrometer 10^3 times lower than that of PMTs, because we can only see significant LED signal without any 0.5% foil (while PMTs need 2-layer of foil to avoid saturation).

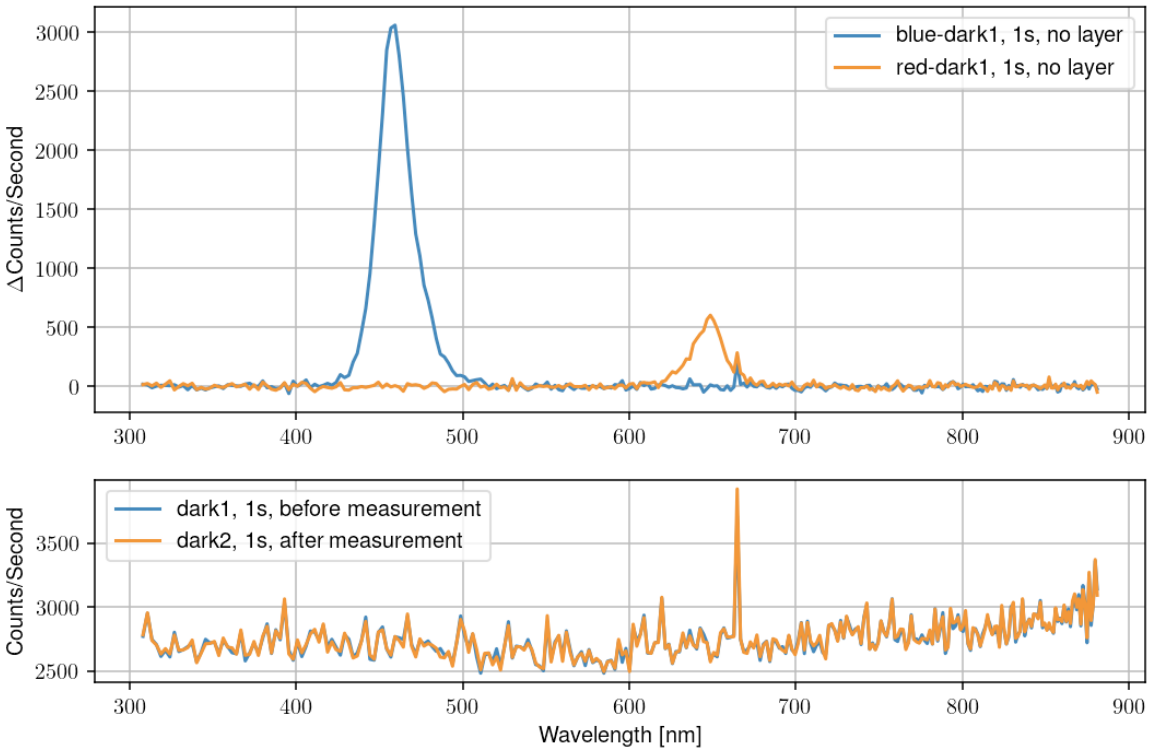

Figure 4.26: Lower plot is the dark record at the very beginning and at the end of the LED measurement. Upper plot is the measurement with the blue LED and the red LED together illuminated and subtracted by the dark counts. The integration time is 10ms.

Camera's sensitivity is halfway between those of Mini-spectrometer and PMTs. It can see faint LED light with one layer of foil.

4.10 Dark Counts' Level in Dependence on Temperature

Most photodetectors suffer from crosstalk, a phenomenon in which a pixel responds to an activity of its neighbours regardless of whether it is illuminated; and dark currents, where thermal activities can spontaneously induce photoelectrons. The current density of photoelectric emission depends on temperature [40]:

$$J_{thermal} \propto T^2 exp(-W/k_B T) \tag{4.10.1}$$

where W is the electronic work function of metal material inside detect area. The current density increases linearly at low temperature and logarithmically at high temperature. The demarcation between low and high depends on work function. Therefore, for every single device, even every single pixel, their dark count's temperature dependence should be measured.

Inside the PMT-spectrometer there are three kinds of photodetectors: the PMT, the camera and the mini-spectrometer. We measured the dark counts of all three devices in a dark, thermally controllable environment to observe the effect of temperature. The temperature starts from $25C^{\circ}$ then gradually reduces to $0C^{\circ}$. We record the dark counts of PMTs, Mini-spectrometer and Camera very 5 min. For future measurement in the ocean, with these pre-measured dark counts, we can do "subtract dark counts" operation respect to environment temperature. The results of PMTs shows trivial constant, which will not be shown here. Results of Mini-spectrometer shows expected non-linearity:

Figure 4.27: Mini-spectrometer measurements inside a freezer. The environment could be regarded as dark. The plots present counts rate (counts per millisecond) with 3 different integration time: 10 ms, 100 ms and 1000 ms. The measurements were down every 5 minutes. There are 150 temperature steps between 0C° to 25C°, but only 6 were shown in plots. When temperature > 10C° and integration time equals 1000 ms, we can see the dark counts are significantly higher than 1900 (average number of lower temperature or shorter integration time). That means rising temperature and long integration time make dark counters non-linearly increasing.

After we have done the measurement shown in figure 4.27, we know that non-linearity occurs within second-scale of integration time. More measurements on second-scale have been done to interpolate ADC counts on of time-temperature space:

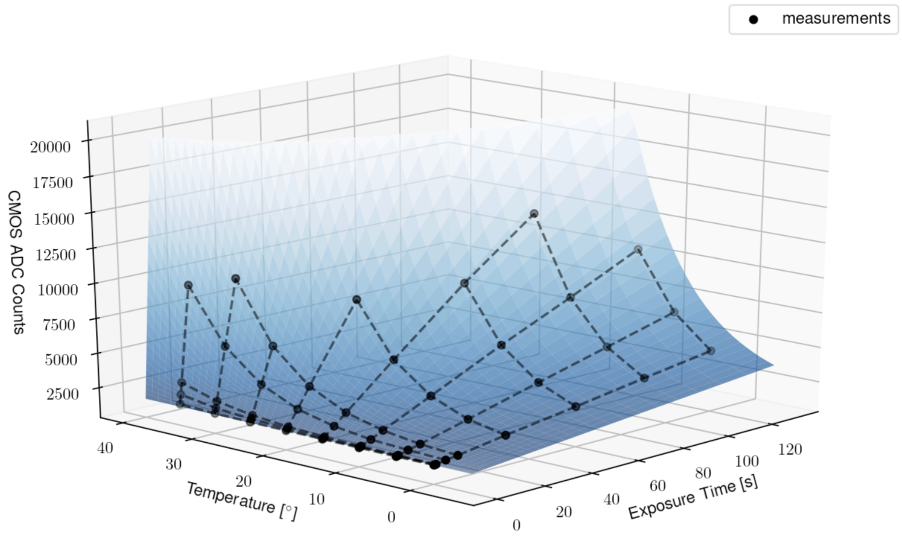

Figure 4.28: Measured behaviour of the mini-spectrometer with serial number 19I00091 (total number of pixels is 288, only one is shown here). After interpolating dark counts as a function of time and temperature, we see that all measurements are located on the same curved surface. In the future analysis, we can extract the dark counts directly from this interpolation according to environmental parameters. The figure is courtesy of Kilian Holzapfel.

5 Data Acquisition and Control Software of the PMT-spectrometer

5.1 Read-out Electronics

This section will explain how the read-out exactly works, a topic that was briefly mentioned in STRAW-b conception section 3.2 but not treated in due detail.

The PMT read-out is jointly handled by a Trigger Read-out Board (TRB3sc) and a PaDiWa3. This system first splits the signal into four channels of different gain by resistive splitter, as shown in figure 5.1, then amplifies raw signals to increase the overall dynamic range.

A time-digital converter (TDC) then measures the event duration by detecting the time it lapses between a signal's rising and lowering edges, enabling nanosecond precision time measurement. The total charge contained in a pulse is reconstructed from the integrated signals via time-over-threshold (ToT) method. The voltage threshold is crucial to the working of ToT method, are made adjustable through PWM and a low pass filter inside TDC. Therefore, one can set a suitable threshold value that retains 90% height of pulse, which is verified by practice as the best choice to keep signal and filter out the background.

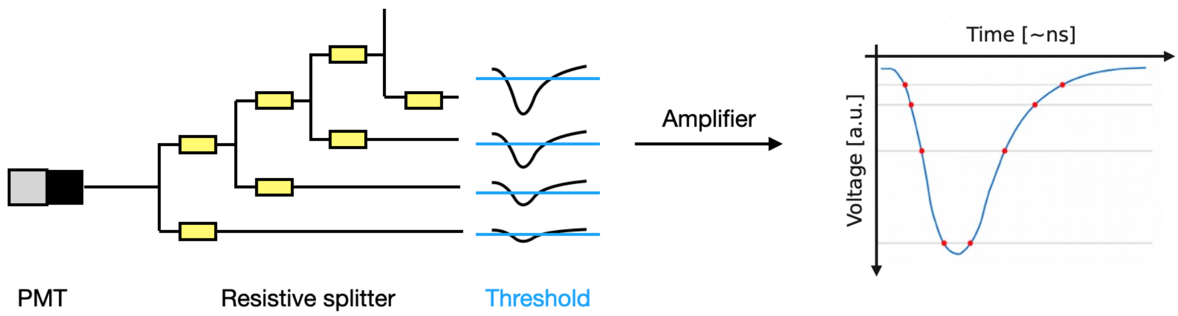

Figure 5.1: Schematic drawing of the PMT's signal procedure.

The TDC time determination is realised by so-called tapped delay line—an array of D-flip-flop. A physically significant pulse consists of a rising and a lowering edge, signalling the STRAT and the STOP of an event. As shown in Figure 5.2 (a), the START signal will propagate into each through a delay line where each element causes a delay of τ, and gives C-port a high (1). As long as the STOP signal has not arrived, D-ports of all D-flip-flop are low (0), so that Q-ports output is 0. As soon as the STOP arrived, all D-ports will become high (1), and the signal outputs on Q-ports become high (1). Therefore Q-ports records the timestamp of rising and lowering edge. They resembled a pattern shown in 5.2 (b), while lines from top to bottom represent the change of values on Q_1 to Q_2. The duration of high is correlated to the deposited charge inside pulse.

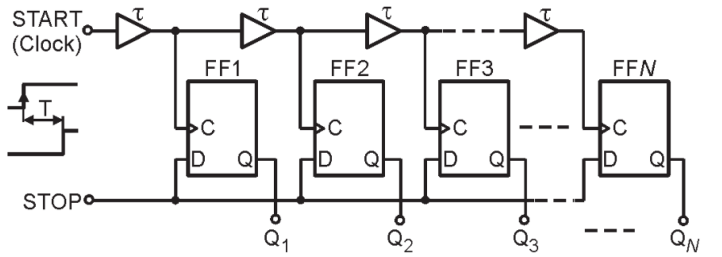

(a) The electronics components of a tapped delay line: a line of D-flip-flop unit, each unit give a delay τ.

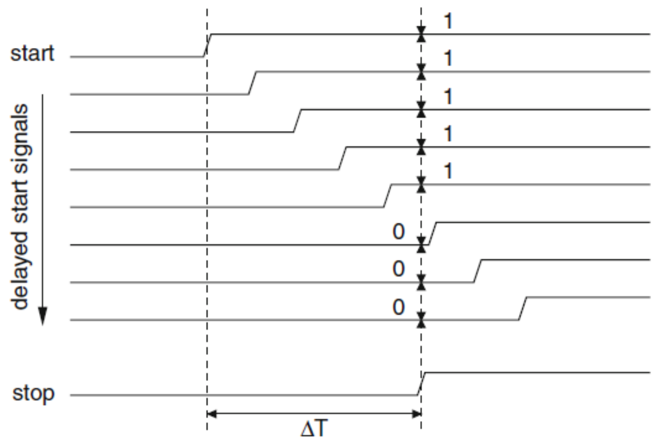

(b) The timestamps of start signal(with delay) and stop signal.

Figure 5.2: Work principle of precise time measurement [41].

One can use well-developed online tools to monitor and control data acquisition, as shown in the following screenshots. With these, one can monitor counts on each channel, set up the mode of triggering (internal/external), triggering pulse frequency, thresholds and their offset, and finally do some basic data analysis:

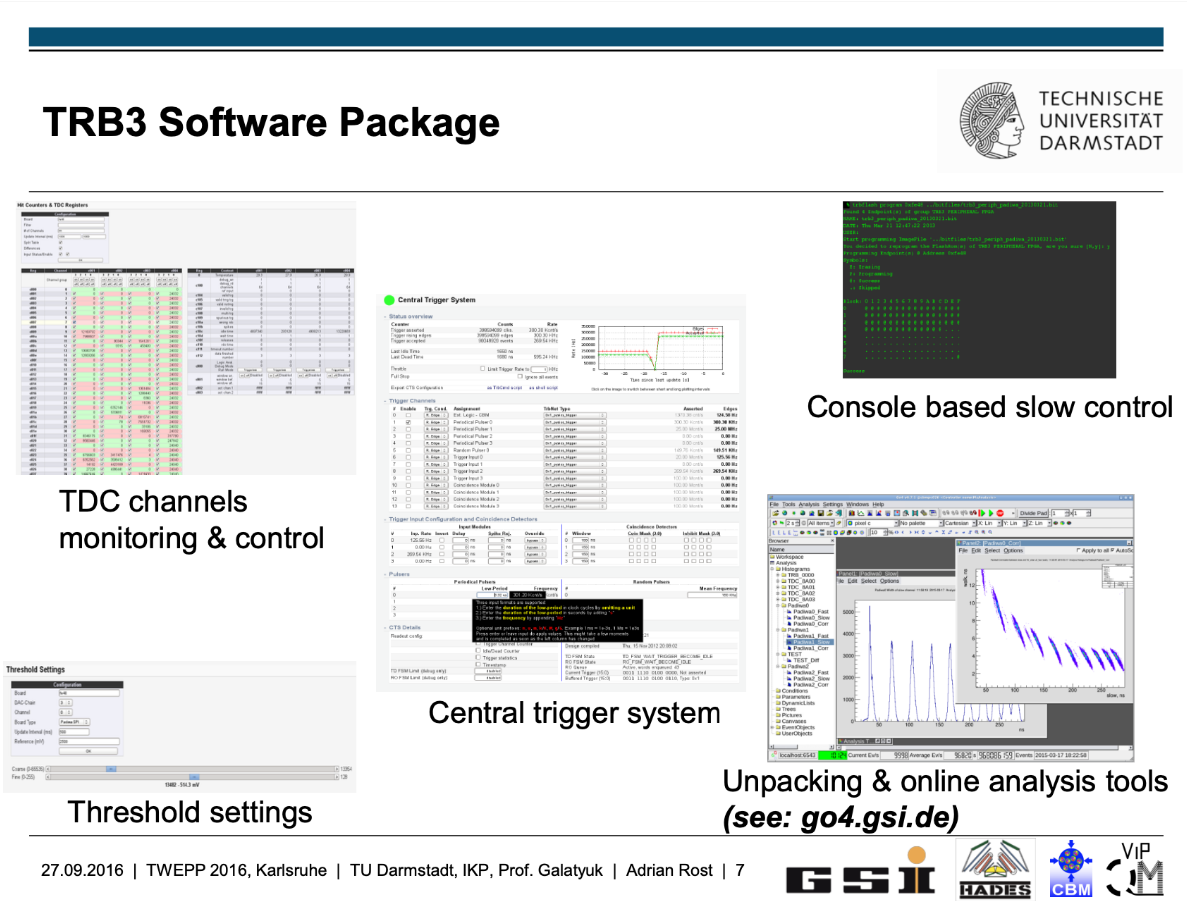

Figure 5.3: Software Package of TRB3, including command-line monitors, website monitors and setups, data unpacking and analysis tools [42].

During PMT-spectrometer's operation, Odroid-C2 will continually read and store PMT counts, while a Mini-spectrometer and camera only become active when PMTs receive a strong signal. Despite being user friendly, online tools usually suffer from a sizeable computational overhead when one loads the website. Besides, data transfers through the website are slow. Rather than using online tools, one can directly access the hexadecimal form of counts stored inside a TRB by calling pre-installed **trbcmd** command in Odroid-C2 terminal, which will significantly speed up the data read-out.

As a result, for PMT counts read-out, we use online tools only for non-critical monitoring situations, while taking and storing data in the long run via **trbcmd** command. **trbcmd** command returns two columns of hexadecimal numbers (see figure 5.4), containing channels and accumulative counts, respectively. The first row 0x1500 of the returned data is always "channel of internal readout trigger" (the externally connected channel start from 0xc000). The first row defines the starting time relative to which all later data will be referenced. The counts on the internal trigger channel will increments by 1 after every period of internal periodical pulser.

```
odroid@odroidc2:~
  trbcmd rm 0x1500 0xc000 0x11 0
H: 0x1500  0x0011
0xc000  0x000d3c5a
0xc001  0x80000557
0xc002  0x80000001
0xc003  0x80000e65
0xc004  0x80000001
0xc005  0x80002b0f
0xc006  0x80000063
0xc007  0x80000ee8
0xc008  0x80001a13
0xc009  0x80000f56
0xc00a  0x80000123
0xc00b  0x80002733
0xc00c  0x80000e30
0xc00d  0x80000edf
0xc00e  0x80000001
0xc00f  0x80001ca1
0xc010  0x80000001
```

Figure 5.4: Hexadecimal output in terminal after calling trbcmd readout command.

We are interested in a count rate, instead of an accumulative count. In other words, if N_1 and N_2 are photon counts at two instances of time spaced 1 second apart, it is the $N_1 - N_2$ (in Hz) that matters here. It is worth mentioning that every channel has only a 31-bits of storage, which corresponds to a maximum photon count of $2^{31} \approx 2 \cdot 10^9$. When an accumulative count reaches its upper limit, it will reset to 0. This must be considered in analysis when we calculate the difference between two counts.

5.2 Master Control Software: mctl

The communication between Odroid-C2 and readout electronics is achieved by different types of serial interfaces (I2C, SPI, RS-232, etc.), which mediates between machine-level commands and high-level language C. In addition to the accessibility of underlying code, which would prove useful for those who intend to perform calibrations and electronic testing, we also need a user-friendly interface that simplifies the data acquisition process for the non-experts. Therefore, we developed **mctl** (short for "master control") software [**mctl**].

All mctl commands share the following structure:

$$\underbrace{\text{mctl}}_{\text{first call mctl program}} \quad \underbrace{\text{pmtspec}}_{\text{then specify module}} \quad \underbrace{\text{hv}}_{\text{specify subsystem}} \quad \underbrace{\text{setValue}}_{\text{specify function}} \quad \underbrace{\text{default}}_{\text{possible parameter for function input}} \tag{5.2.1}$$

As an example, if one wants to set voltage values for PMT-spectrometer according to 4.3, one can call **mctl pmtspec hv setValue default** command in Odroid- C2 terminal. The mctl parser will find "hv" class in "pmtspec" package, and call "setValue" function with parameter "default". This function reads the default values from a text file and then invokes a compiled C program, which sends converted hexadecimal numbers to DAC using I2C protocol. In this way, we can set the default high voltage values for PMT-spectrometer.

mctl is written in object-oriented Python. Each Python sub-package corresponds to a specific real-life module, to the extent that each class within the corresponding sub-package maps uniquely to a functionality of its corresponding module. Modular functions were implemented by inheritance, where additional functionalities are added if required. Inheritance-based programming offers the advantage of allowing us to carry out identical changes on multiple modules simultaneously.

As examples, LiDAR, PMT-spectrometer and muon tracker all use the TRB data acquisition system, thereby motivating the use of a base class for all three. LiDAR has two active channels, whereas PMT-spectrometer has 16, so their respective classes differ in the default parameter of "readout channels" function. Furthermore, because muon tracker has a readout frequency that is different from that of the other two modules, the "set readout frequency" function of its class is extended.

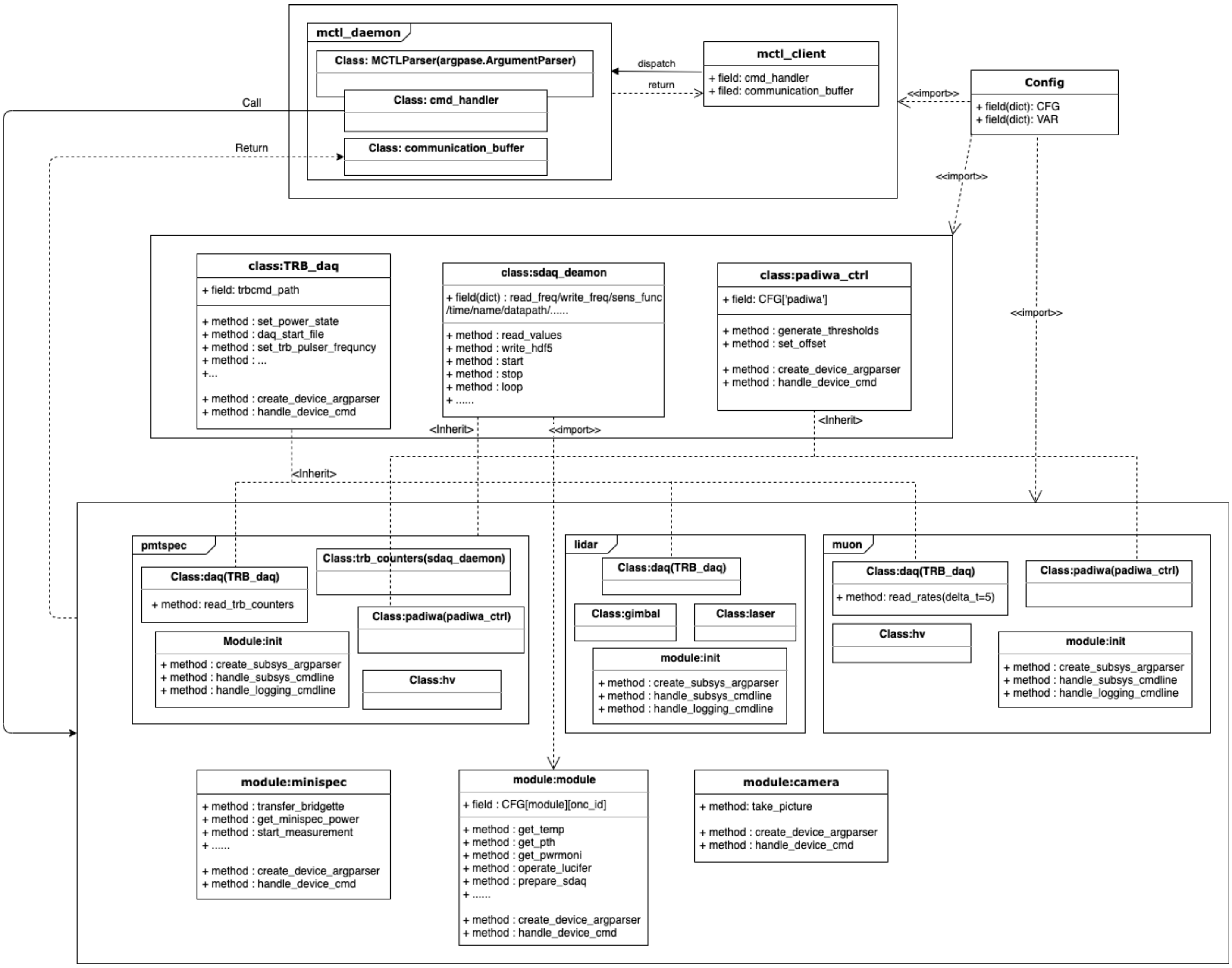

Figure 5.5: Structure of mctl software

We want to avoid parsing mctl commands in terminal around the clock, since this will keep the whole program active in the meantime and could conflict with other terminal processes. To resolve this difficulty, we use a Pyro (Python remote object) package, which works as follows. Pyro can generate two types of objects–daemon and client. The client object's only purpose is to send the command to daemon, which, when invoked, will be initialised. One can publish a regular Python object to Pyro daemon so that it became a remote object. After that, daemon could start processing it. A communication buffer function is defined in daemon and reachable for client, keep the communication (sending commands and collecting returned results) between server and client. The command handler in daemon can identify from which remote object made the request it has received originate, and, as a response, create only objects that are compatible with the module's hardware. For example, if we send a mctl command from LiDAR, camera class of the base class won't assign any object to LiDAR because it doesn't obtain any camera.

5.3 Data Format

PMT-spectrometer has two data-recording modes: 1. By calling command **mctl pmtspec daq rates show**, all 16 channels rates are displayed and stored only once. 2. By calling **mctl pmtspec daq rates start**, all 16 channels rates are continuously written into an HDF5 file. This recording will keep running in daemon until **mctl pmtspec daq rates stop** is called. The output data format of PMT-spectrometer and mini-spectrometer is HDF5.[1] It consumes less memory and can be loaded faster than csv-based data format.

[1](A High-performance data management and storage suite. It is widely used in fields such as astronomy, where huge amounts of heterogeneous data need to be stored and classified in a user-defined data structure.

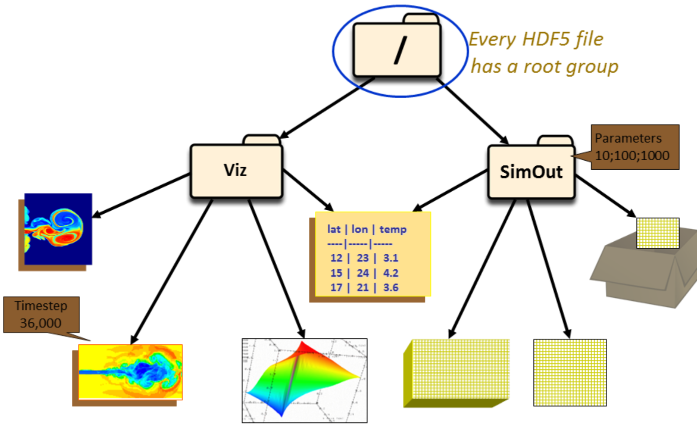

(a) user can create arbitrary groups under the root group, inside group arbitrary dataset can be created and linked to other groups.

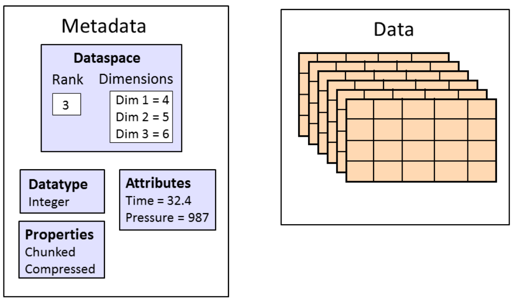

(b) Metadata define type and dimensions of elementary data, it also include "attributes", namely environment parameter when data were taken

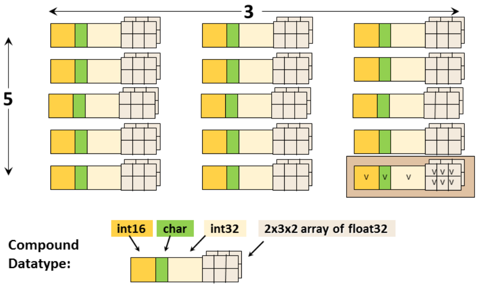

(c) the elementary data could be arbitrary combination of pre-defined data types.

Figure 5.6: Example of user defined HDF5 data format [43].

For example, mini-spectrometer's HDF5 output attributes include time, temperature, and its calibration parameters. Under the root group, 5 subgroups were created, corresponding to 5 SPI ports connected to mini-spectrometers. Inside each subgroup, **ADC counts** and **wavelength** datasets are created. All auxiliary helper functions, such as data import or print, are built-in. Values in every dataset can be easily accessed by calling their labels.

Camera returns a two-dimensional matrix of light counts in accordance with its pixel grids. The raw matrix can be converted to JPEG format in later analysis, when dark counts can be subtracted.

TRB built-in data acquisition script saves raw timestamps of edge crossings (rising, falling) for a threshold set in the PADIWA, with a nanoseconds precision. The format of this file is a binary HLD [44]. PMT-spectrometer normally does not use this data format, except in circumstances where very precise loggings of timestamps are required. In contrast, modules such as laser reflection logger in LiDAR and Muon tracker timestamp logger save data in HLD format due to a demand for precise time measurement for attenuation length calculation.

The binary HLD file could be converted to decimal numbers by a ROOT-based unpacking software [42]. The unpacked data of STRAW multi-channel PMTs has a structure shown in figure 5.7. However, the structure of unpacked data can be modified by rewriting the unpacking script. How we are going to unpack the HLD file for STRAW-b single-channel PMTs is relatively open.

```
Channel                    Absolute timestamp   Rising   Falling  Rising   Falling  Rising   Falling
000001 -50697.25000 21249302.75000 0.00000 3.54297 0.00000 0.00000 0.00000 0.00000  ...  ...
000002 -37134.71094 21262865.28906 0.00000 8.96094 1.98438 10.0312 0.00000 0.00000  ...  ...
  ...      ...
```

(a) In STRAW every PMT has four channels. All obtainable information are stored. Arrival time of rising and falling edges for a channel listed alternatively in a row.

```
Channel, Rising, Falling
03, 21249302.75000, 21249305.54297
12, 21262865.28906, 21262873.41609
..., ..., ...
```

(b) In STRAW-b, every PMT has one channel, one module has 12 channels altogether. The provisionally unpack structure maintains only the necessary information: channel, rising and falling timestamp. Every single pulse is in a single row.

Figure 5.7: Example of unpacked HLD data in decimal text.

6 Simulation of the Water Current-Induced Bioluminescence

In section 3.1.2, we mentioned that the water current at Cascadia Basin in Pacific ocean has a strong correlation (r=0.62) with the ambient bioluminescence measured in STRAW. This correlation is shown in figure 6.1. To understand the mechanism behind the correlation, we have prepared a novel simulation. The construction of the simulation mainly depends on four input data:

i Water current modelling. Movements of water current determine the direction, momentum and stress of bioluminescent animal impinging on STRAW-b.

ii PDFs of bioluminescence emission. They are currently adapted from literature and will be replaced by measured spectra once we obtain useful data from the STRAW-b spectrometer.

iii Attenuation properties of water. Currently we use values from literature [45]. It will soon be replaced by the results of STRAW attenuation analysis in chapter 3.1.1.

iv Detector properties such as quantum efficiency, which are already known.

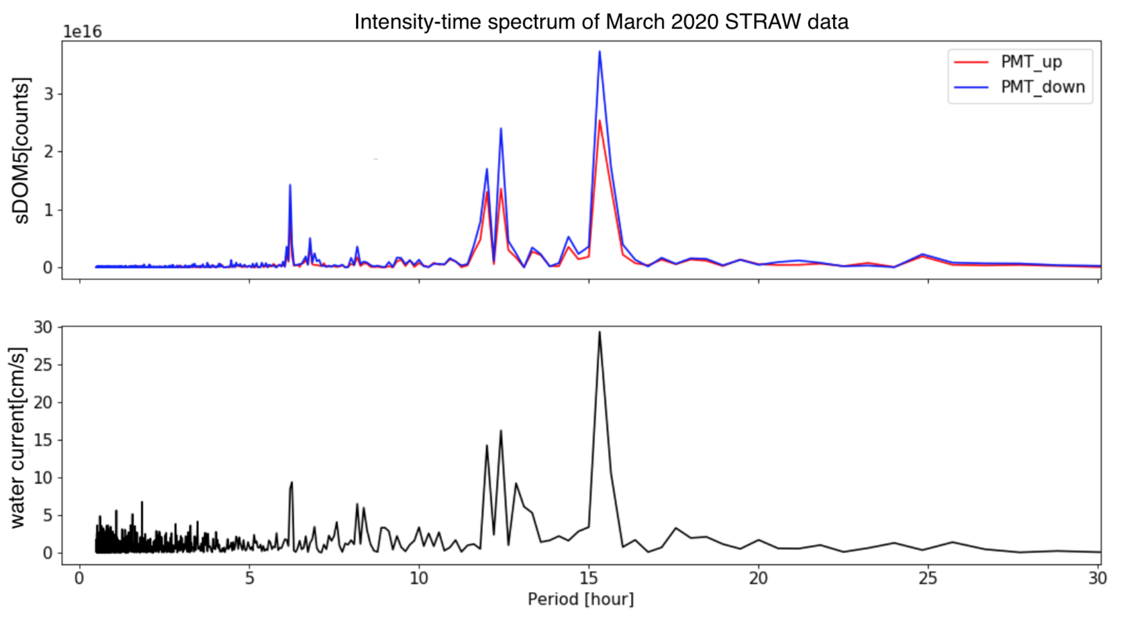

Figure 6.1: Water current speed and photons number detected by both up- and down-ward PMT on sDOM5 in STRAW, shows synchronous patterns. The figure is courtesy of I.C Rea.

6.1 Structure and Working Principle of the Simulation

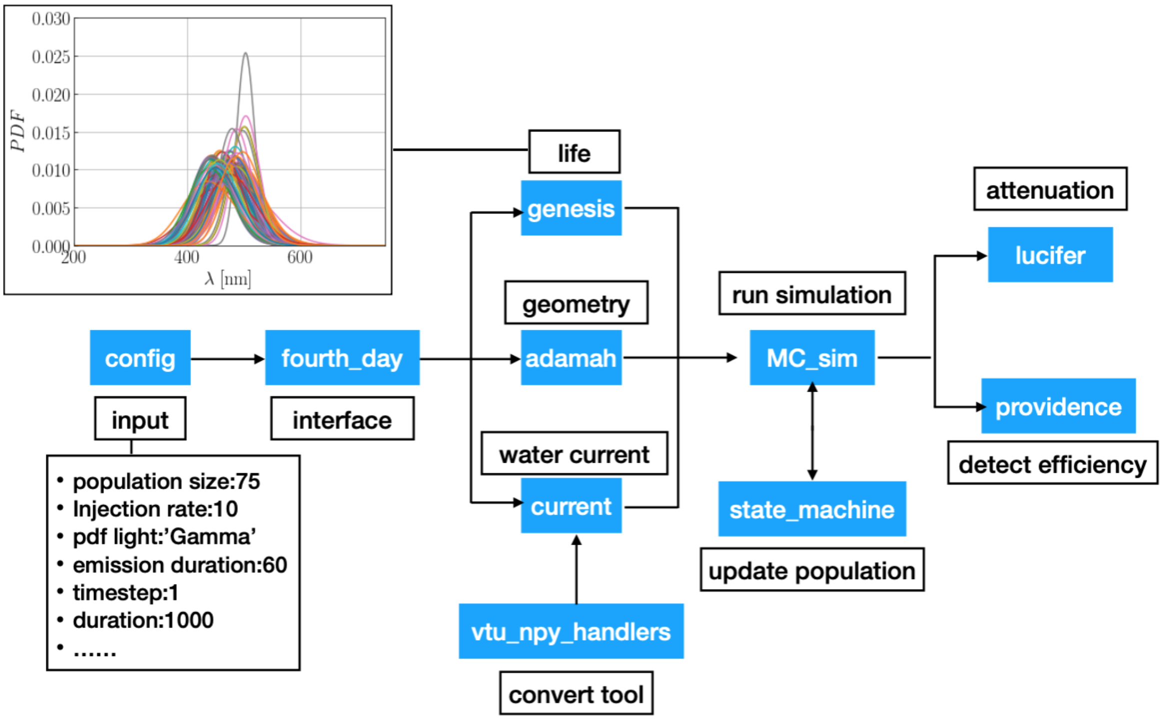

Figure 6.2: The simulation software flow chart. Every blue square stands for a single Python module. The white squares beside each blue square give a short explaination of the function of this module. A part of the config file input data and light spectra of one phylum are given as examples.

Figure 6.2 shows the structure of the simulation software. Genesis, Current and Adamah are three modules providing basic construction of the real environment. **Genesis** loads and parses bioluminescence data (name, maximum emission, most possible photon emission counts, FWHM) from literature [46]. Then it generates light emission and movement distribution functions of every bioluminescent species. **Adamah** constructs a virtual rectangular container and STRAW-b detector-like spherical volume inside the container. It also provides a function to examine whether a point is inside the detectable range. **Current** constructs water current properties by dividing the whole volume into a user-defined number of triangular grids. Each grid contains the information of its defined velocity and gradient. The simulation mode of water current could be static, homogeneous (constant speed on y-axis), or cylindrical [47]. The last is the most appropriate choice for water around STRAW-b's spherical cross-section.

Fourth_day can generate a random state seed and define a run time. It invokes **MC_sim** to do the major jobs of simulation and keeps a log of every run step. In **MC_sim**, pre-defined populations of species will be distributed into the environment according to given properties in Genesis, Current and Geometry. **State_machine**, as an auxiliary module, helps **MC_sim** on numerical calculations of every iteration. In each iteration, it masks organisms which are outside the observation volume to reduce the calculation time, updates movements of organisms and injects new organisms. The most important function of **State_machine** is to give every organism a binomially distributed emission probability. All useful properties of every single organism will be stored in a dictionary, as shown in figure 6.3.

	species	pos_x	pos_y	velocity	angle	radius	energy	observed	max_emission	emission fraction	regeneration	is_emitting	emission_duration
0	Paraphyllina ransoni Russell	12.056651	8.126339	0.0	0.000000	0.001357	1.0	True	10.877831	0.1	0.0001	False	-1000.0
1	Aeginura grimaldii Maas	35.335847	17.992581	0.0	1.275677	0.001191	1.0	False	1.135903	0.1	0.0001	False	0.0
2	Praya dubia (Quoy and Gaimard)	11.518483	13.313078	0.0	1.003611	0.001422	1.0	False	7.875777	0.1	0.0001	False	0.0
3	Nectopyramis natans (Bigelow)	20.351772	14.689393	0.0	0.148222	0.001231	1.0	False	4.946962	0.1	0.0001	False	0.0
4	Periphyllopsis braueri Vanhoeffen	5.867822	0.858568	0.0	4.555514	0.001364	1.0	False	7.745598	0.1	0.0001	False	0.0
...	...	...	...	...	...	...	...	...	...	...	...	...	...
95	Apolemia sp. 1	23.236617	9.945163	0.0	0.000000	0.001066	1.0	True	25.933412	0.1	0.0001	False	-1000.0
96	Halistemma sp. nov.a	23.775387	18.168985	0.0	1.793675	0.000400	1.0	False	10.393219	0.1	0.0001	False	0.0
97	Aulacoctena acuminata Mortensen	33.328005	2.446869	0.0	5.346992	0.001117	1.0	False	12.367799	0.1	0.0001	False	0.0
98	Mertensiidae gen. nov. B sp. nov. Dad	4.686522	9.713101	0.0	0.000000	0.000918	1.0	True	0.852034	0.1	0.0001	False	-1000.0
99	Photobacterium phosphoreum ANT-2200	27.875176	12.802740	0.0	1.917915	0.001106	1.0	False	19.231270	0.1	0.0001	False	0.0

Figure 6.3: The simulation software results table. All organisms are listed by their species name. It contains the state(its position, velocity) of every organism at the end of the simulation, as well as the important messages during the simulation (whether it has been detected, observed, or emitted). To simplify the later calculations, some pre-defined properties, such as maximum emission energy, are also listed.

Finally, **lucifer** handles the optical process of light propagation in water, while **providence** takes the detector's efficiency into account.

6.2 Simulation Results

We use a population size of N=100, a simulation duration of t=1000 s, and a new population injection rate of 10^{-3}/s. By examining the distance between every single organism and detector, we can determine if they are encountering the detector. If they are, we give them a bounce-back movement and their encounter state will be recorded. Whether the encountered species would emit light is a yes-or-no choice, namely binomial. Besides a pure binomial distribution, we must take another condition into account: only species having enough energy and already recovered from last emission, can emit. Therefore, we check whether their energy is larger than a user-defined threshold and set their burst duration as 60 s. Figure 6.4 shows a 1000-second simulation in these scenarios.

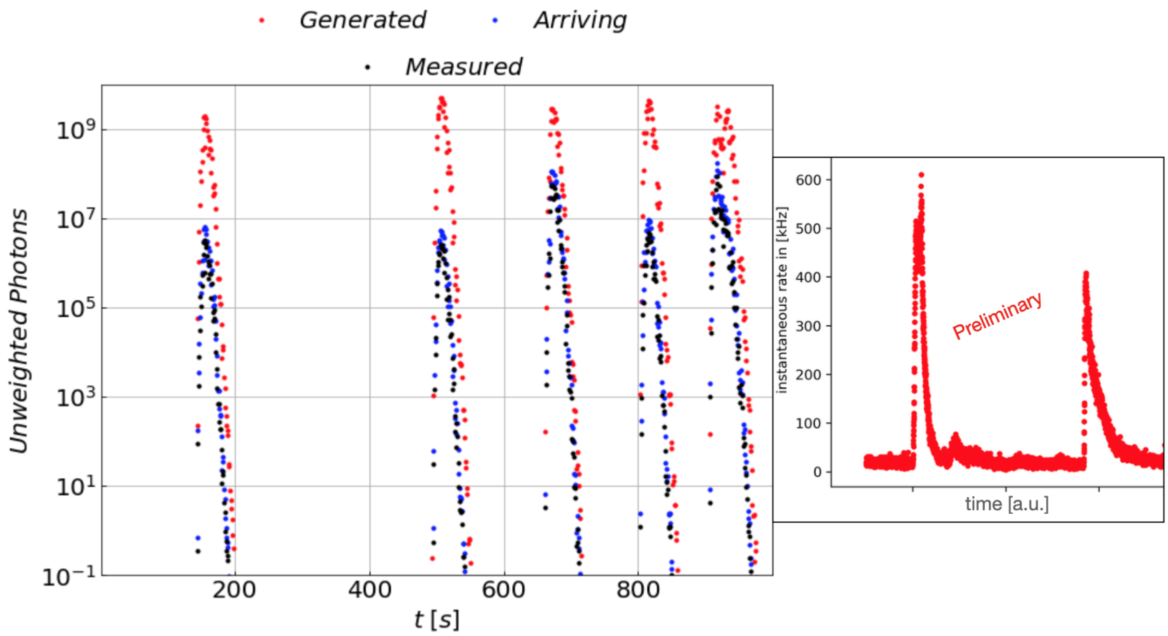

Figure 6.4: Left: 1000 s simulation of bioluminescence background. Red dotted lines are photons generated by species, which are gamma-distributed and decay within time. Blue dotted lines are photons that have reached the detector. Black dotted lines are photons that are finally detected when considering the detector efficiency. Right: A plot of STRAW-b measured bioluminescence pulses is attached here as a compare. (This data is preliminary. The timer inside this module still needs some calibration and therefore gives an inaccuracy time unit.) We can see beside the dark counts, which is not included in our simulation, the measured pulses and simulated pulses have the same gamma distribution.

We run the same simulations 300 times and average their measured photon number on every time step for frequency analysis. Then, we use discrete fast-Fourier transformation to convert counts-to-time into counts-to frequency space. The result is shown in figure 6.5:

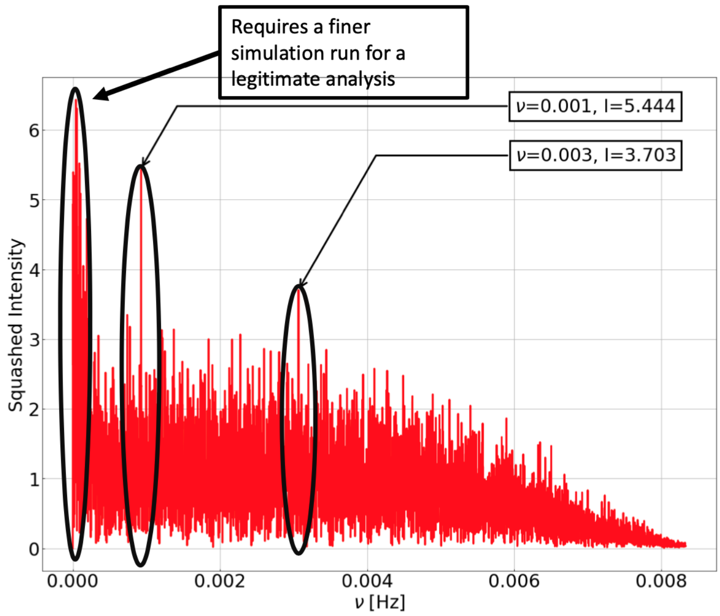

Figure 6.5: The simulation shows three significant peaks in the frequency spectrum. The suspected reason for the last two peaks could be turbulence caused by the string line and glass sphere, respectively. To find the possible reason for the third peak with the smallest frequency, we need a finer simulation. The figure is courtesy of Stephan Meighen-Berger.

In fluid mechanics, the dimensionless Strouhal number (St), which describes oscillating flow mechanisms, is a function of the Reynolds number (see figure 6.6). The Reynolds number (Re), which predicts flow patterns in different scenarios, fully depends on the characteristics of the fluid [48].

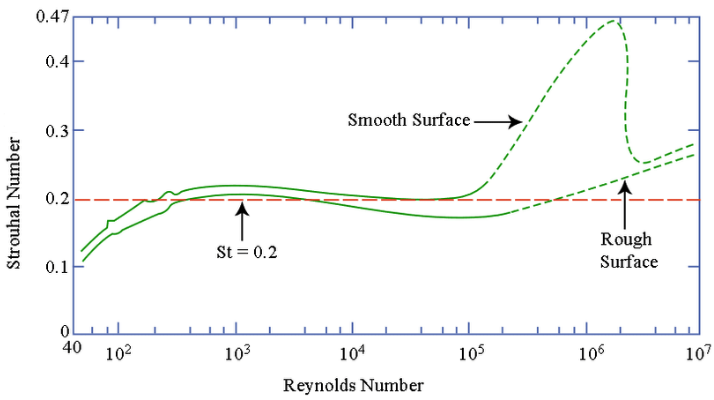

Figure 6.6: Relationship between Strouhal Number and Reynolds number for vortex shedding in a uniform stream. Graph by MIT Open Course Ware fluid mechanics.

In our situation, the variation of the water current speed over virtual volume is within the same magnitude, while viscosity and density of water are relatively stable. Therefore, the Reynolds number and related Strouhal number would not have a large variation. The Strouhal number is often calculated by:

$$St = \frac{fL}{U} \tag{6.2.1}$$

Where f is the frequency of vortex shedding, which is unknown and variable in our situation. L is the characteristic length and U is the flow velocity. Therefore, if we change detector geometry, changing L will lead to changing f. This effect is verified since we have seen a change of peak positions in frequency spectrum with changing geometry in simulation. Therefore, we are sure that these peaks are caused by water current past the circular cylinder section. Ideally, in STRAW's frequency spectrum, we should also see three peak values in the low-frequency regime.
The cross-check analysis in STRAW data is ongoing. We have seen the three peaks in data. Due to very high uncertainty of radioactive backgrounds and electrical noise, after subtracting those backgrounds, the remaining signal is too weak to be convincing. We can refine the simulation step to locate those peaks more accurately (currently we only know there must exist three peaks in a specific range of frequency). Or we can develop a better algorithm to separate radioactive background from bioluminescent signal.

7 Conclusion and Outlook

Preliminary results of STRAW's attenuation length and background have classified the Cascadia Basin as a suitable site for a neutrino telescope. Ocean scientists will review the results, and an analysis paper is in preparation. As planned, STRAW-b was deployed on the first of October. It will obtain additional data to verify and extend STRAW results.

Comparing to STRAW, STRAW-b has improved in many respects. After a successful deployment and operation of STRAW-b at 1. October, we are a step closer to the success of P-ONE. The experiences we gained from the PMT-spectrometer design will be further applied to the upcoming P-ONE optical module design. The deployment strategy and the design of the modules have still room for improvement. We obviously need a more gentle installation strategy to reduce the impact on modules and more protection to stabilise the connection between electronics.

In contrast to already finished hardware works, the development of auxiliary software is an open task. In the future, we will continuously improve the data structure and operation mode for the STRAW-b experiment. The final goal is to have an integrated software system which can automate data taking and essential analysis. We will adopt a more accurate water current and bioluminescence model on simulation to reconstruct reality as closely as possible.

A Wavelength Shift in Medium

The light passed through the ideal Hard-coated Filter has a uniform wavelength distribution function. Suppose we vary the incident angle of the light on the filter. In that case, the constructive interference condition is matched at a wavelength slightly differing from the nominal one (incident angle equals 0 degree). That is because of the existence of two different optical paths (see the sketch below).

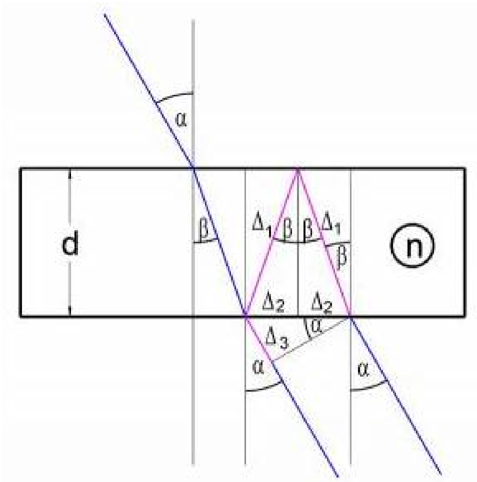

Figure A.1: Light transmission path(blue) and twice-reflexion-path(purple) in a medium of reflex index n.

At $\alpha = 0°$, assuming air has reflection index 1, the constructive wavelength λ_0 has relation with filter sickness d (k_2 are arbitrary integers):

$$k_1 \frac{\lambda_0}{n_{filter}} = 2d \tag{A.0.1}$$

At $\alpha = 10°$, light can take path Δ3 or 2Δ1, light on path Δ3 has phase shift $\Delta\phi$:

$$\Delta\phi_1 = \frac{2d \sin\beta \sin\alpha}{\lambda'} \cdot 2\pi \tag{A.0.2}$$

Light on path 2Δ1 has phase shift:

$$\Delta\phi_2 = \frac{2d/\cos\beta}{\lambda'} \cdot 2\pi = \frac{2dn_{filter}}{\lambda' \sqrt{1 - \sin^2\alpha \frac{1}{n_{filter}^2}}} \cdot 2\pi \tag{A.0.3}$$

where $\sin\alpha = n_{filter} \sin\beta$ according to Fresnel equations. The constructive interference happens when $k_2 \cdot \Delta\phi_1 = \Delta\phi_2$, ($k_2$ are arbitrary integers), there for we have:

$$k_2 = 2d \cdot \frac{\frac{n}{\sqrt{1-\sin^2\alpha \frac{1}{n^2_{filter}}}} - \frac{\sin^2\alpha}{n_{filter}}}{\lambda'} \tag{A.0.4}$$

combining B.0.1 and B.0.4 we have relationship between original wavelength λ_0 and shifted wavelength $\lambda^{'}$:

$$\frac{\lambda_0}{\lambda'} = \left(\frac{1}{\sqrt{1-\sin^2\alpha \frac{1}{n^2_{filter}}}} - \frac{\sin^2\alpha}{n^2_{filter}} \right) = \frac{k_1}{k_2} = 1, \quad \Longrightarrow n_{filter} = 1.95 \tag{A.0.5}$$

If we insert the measurement value λ_0, $\lambda^{'}$ and α according to Figure **??**, we can get the result that hard-coated filter has wavelength shifted effect as a homogeneous medium of $n = 1.95$. If we adopt $n = 1.95$, α and λ_0 to other filters, they give the values of $\lambda^{'}$ which are corresponding to the measurement.

B Electronics inside the PMT-spectrometer

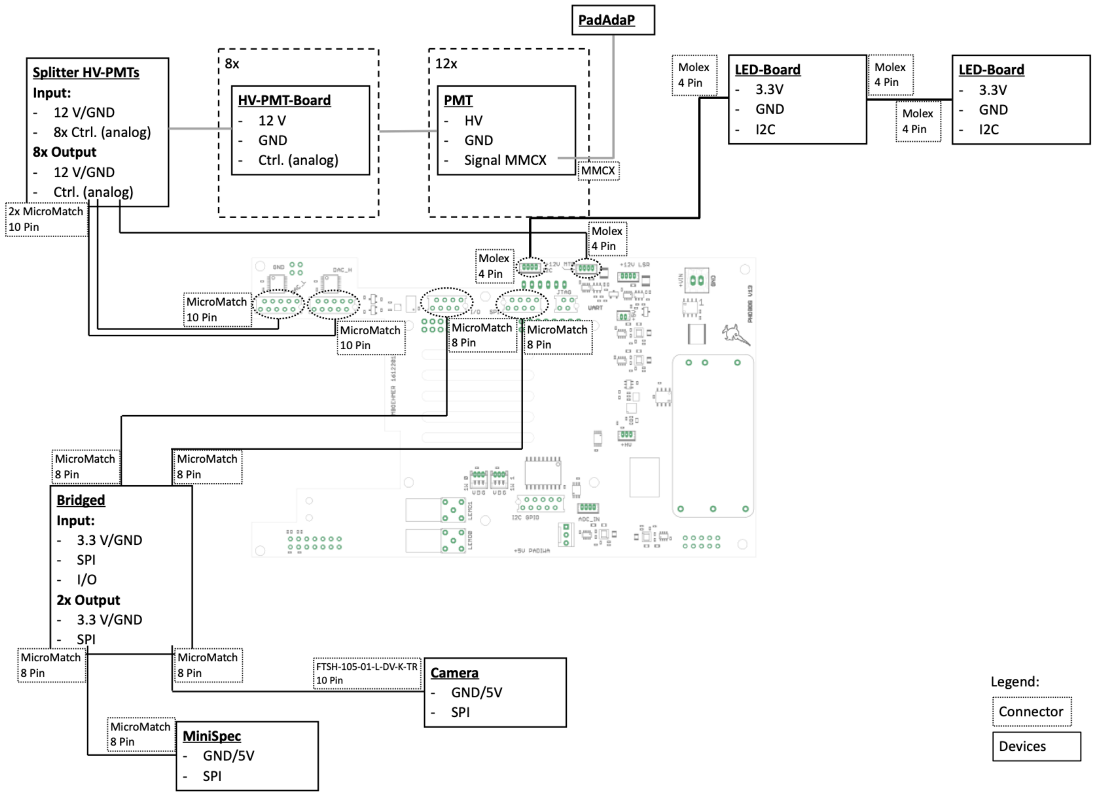

Figure B.1: Positions that PMT-spectrometer occupied on Phobos board and type of connectors used on each position.

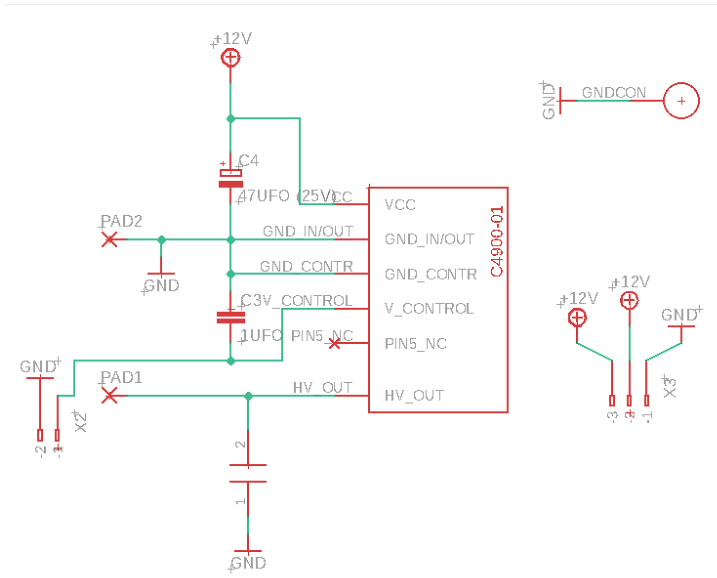

Figure B.2: Schematic of HV converter PCB.

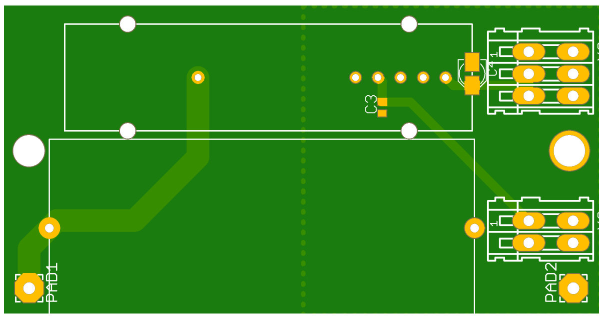

Figure B.3: Manufacture of HV converter PCB. Diagram courtesy to Tobias Pertl.

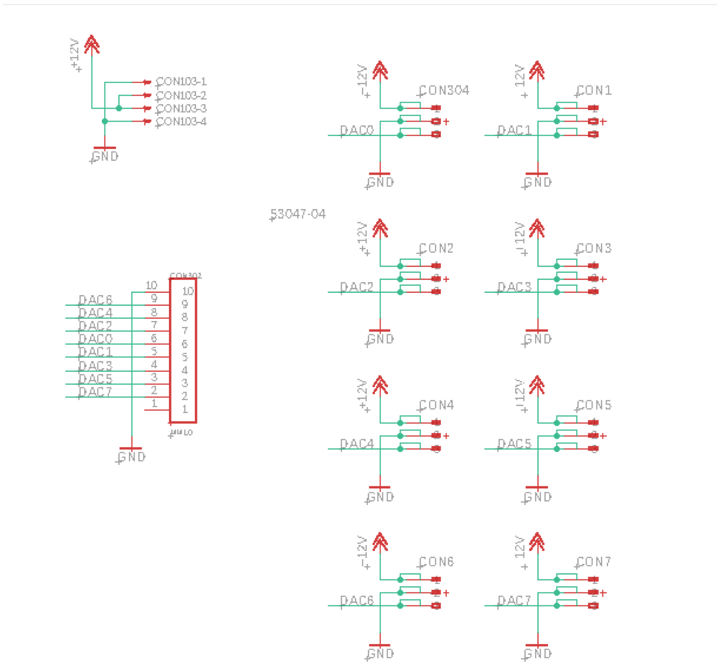

Figure B.4: Schematic of HV splitter PCB.

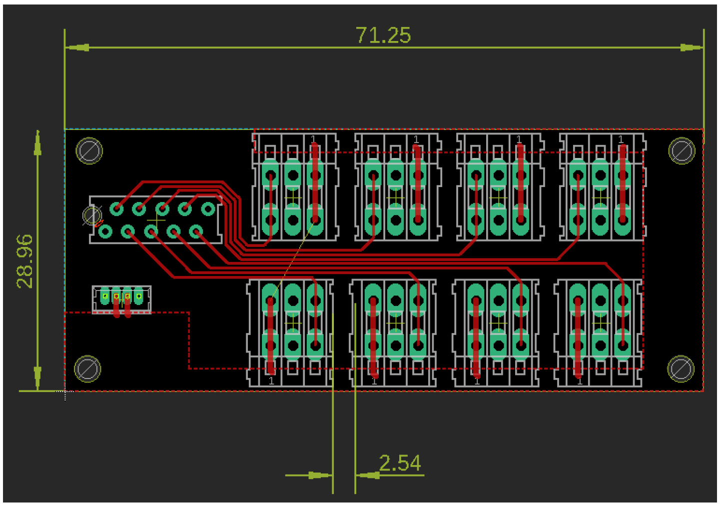

Figure B.5: Manufacture of HV splitter PCB.

C Deployment in Canada

Figure C.1: Preparing tray for pool test. Mounting modules and coiling the VEOC cable on tray. Placing position markers.

Figure C.2: Modules submerged in pool. Preparing for underwater pressure and humidity test.

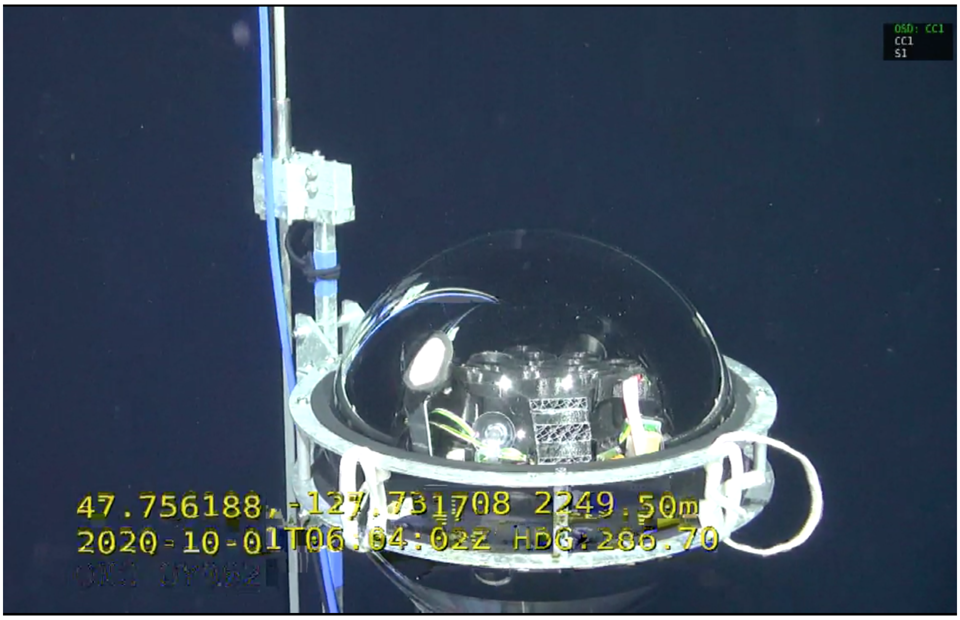

Figure C.3: Since 1.October, PMT-spectrometer modules are operating in deep sea.

Acknowledgments

First of all, I would like to thank professor Elisa Resconi who gives me the opportunity to be involved in the STRAW-b project and opens the door for me to astro-particle physics. She always offers encouragement and creates a harmonious atmosphere in the group. I'm also very grateful to Dr. Alexander Mann, who is willing to be my supervisor in LMU. Thanks for his enthusiastic response to my reports and the patience every time we meet, which is encouraging.

Designing, building and eventually deploying the STRAW detector highly demands team work. Here I would like to express my appreciation to my friendly and experienced colleagues, the preliminary success of project can't be achieved without them: Thank Dr. Christian Fruck, Kilian Holzapfel, Stephan Meighen-Berger, Dr. Michael Böhmer and Christian Spannfellner for their expert supervision. Thank the colleagues with whom we spent time of inspiring cooperation together: Felix Henningsen, Martina Karl, and the rest of STRAW-b group: Dr. D. Vivolo, I.C Rea, Dr. M.Wolf, C.Bellenghi.

Finally, a special thank to my boyfriend Renhao Tao, who took his valuable time in proof-reading the manuscript and contributing helpful comments. Thanks for all your supporting during my physics study.

-Ruohan Li

Erklärung:

Hiermit erkläre ich, die vorliegende Arbeit selbständig verfasst zu haben und keine anderen als die in der Arbeit angegebenen Quellen und Hilfsmittel benutzt zu haben.

Munich, 12.October 2020
Ruohan Li

List of Figures

List of Tables

Glossary

ADC analog-to-digital converter. 26

CTS central timing system. 14

CWL centre wavelength. 35

DAC digital-to-analog converter. 26

DAQ data acquisition. 14

DOM ditigal optical module. 9

FPGA field-programmable gate array. It is an integrated circuit designed to be configured by a customer or a designer after manufacturing. 14

FWHM Full Width-Half Maximum. 35

GPIO General-purpose input/output (GPIO). Digital signal pins on an integrated circuit or electronic circuit board whose behaviour is controllable by the user.. 26

GZK Due to interaction between high energy particle and microwave background radiation, Greisen-Zatsepin-Kuzmin (GZK) limit is a theoretical upper limit on the energy of cosmic ray protons traveling from other galaxies through the intergalactic medium to our galaxy. The limit is 50 EeV). 6

HDF Hierarchical Data Format. 73

HLD Heavy Light Decomposition. A method of decomposing the vertices of the data tree into disjoint chains.. 56

HV high voltage. 30

I2C A serial protocol for two-wire interface to connect low-speed devices like microcontrollers, EEPROMs, A/D and D/A converters, I/O interfaces and other similar peripherals in embedded systems.. 27

MJB mini junction box. 14, 91

ONC Ocean Network Canada. 13

PD photodiode. 33

PMT photomultiplier tube. 8

POCAM Precision Optical Calibration Module. 14, 91

PWM Pulse-width modulation. A method of reducing the average power delivered by an electrical signal, by effectively chopping it up into discrete parts. 67

QE quantum efficiency. 33

SiPM Silicon Photomultipliers. 25

SPI The Serial Peripheral Interface (SPI) is a synchronous serial communication interface specification used for short-distance communication, primarily in embedded systems.. 27

STRAW The Strings for absorption length in Water. 13

TDC time-to-digital converter. 14

ToT Time over threshold. 67

TRB TDC-Readout-Board, Triggered-Readout-Board and Triggerless-Readout-Board. 14

VEOC vertical electrical optical cable. 26

Bibliography

[1] C. L. Cowan, F. Reines, F. B. Harrison, H. W. Kruse, and A. D. McGuire. "Detection of the Free Neutrino: a Confirmation". In: *Science* 124.3212 (1956), pp. 103–104. ISSN: 0036-8075. DOI: 10.1126/science.124.3212.103. eprint: https://science.sciencemag.org/content/124/3212/103.full.pdf. URL: https://science.sciencemag.org/content/124/3212/103.

[2] G. Danby, J.-M. Gaillard, K. Goulianos, L. M. Lederman, N. Mistry, M. Schwartz, and J. Steinberger. "Observation of High-Energy Neutrino Reactions and the Existence of Two Kinds of Neutrinos". In: *Phys. Rev. Lett.* 9 (1 July 1962), pp. 36–44. DOI: 10.1103/PhysRevLett.9.36. URL: https://link.aps.org/doi/10.1103/PhysRevLett.9.36.

[3] K. Kodama, N. Ushida, C. Andreopoulos, N. Saoulidou, G. Tzanakos, P. Yager, B. Baller, D. Boehnlein, W. Freeman, B. Lundberg, and et al. "Observation of tau neutrino interactions". In: *Physics Letters B* 504.3 (Apr. 2001), pp. 218–224. ISSN: 0370-2693. DOI: 10.1016/s0370-2693(01)00307-0. URL: http://dx.doi.org/10.1016/S0370-2693(01)00307-0.

[4] C. Patrignani and P. D. G. 2. C. Phys. "Review of Particle Physics". In: *Chinese Phys. C 40 100001* 40.10 (2016).

[5] T. K. Gaisser, R. Engel, and E. Resconi. *Cosmic Rays and Particle Physics*. 2nd ed. Cambridge University Press, 2016. DOI: 10.1017/CBO9781139192194.

[6] R. Mirzoyan. "Light Sensing Detectors: Human Eyes, PMTs and SiPM". In: Max-Planck-Institute for Physics Munich, Germany, 30 May 2016.

[7] A. L. Coke. *The Detection of Neutrinos in IceCube*. URL: https://masterclass.icecube.wisc.edu/en/learn/detecting-neutrinos.

[8] J. N. Bahcall and R. Davis. "Solar Neutrinos: A Scientific Puzzle". In: *Science* 191.4224 (1976), pp. 264–267. ISSN: 0036-8075. DOI: 10.1126/science.191.4224.264. eprint: https://science.sciencemag.org/content/191/4224/264.full.pdf. URL: https://science.sciencemag.org/content/191/4224/264.

[9] K. Scholberg. "Supernova Neutrino Detection". In: *Annual Review of Nuclear and Particle Science* 62.1 (2012), pp. 81–103. DOI: 10.1146/annurev-nucl-102711-095006. eprint: https://doi.org/10.1146/annurev-nucl-102711-095006. URL: https://doi.org/10.1146/annurev-nucl-102711-095006.

[10] W. D. Arnett, J. N. Bahcall, R. P. Kirshner, and S. E. Woosley. "Supernova 1987A". In: *Annual Review of Astronomy and Astrophysics* 27.1 (1989), pp. 629–700. DOI: 10.1146/annurev.aa.27.090189.003213. eprint: https://doi.org/10.1146/annurev.aa.27.090189.003213. URL: https://doi.org/10.1146/annurev.aa.27.090189.003213.

[11] C. Giunti and C. W. Kim. *Fundamentals of Neutrino Physics and Astrophysics*. Oxford Scholarship, 2007.

[12] K. Greisen. "End to the Cosmic-Ray Spectrum?" In: *Phys. Rev. Lett.* 16 (17 Apr. 1966), pp. 748–750. DOI: 10.1103/PhysRevLett.16.748. URL: https://link.aps.org/doi/10.1103/PhysRevLett.16.748.

[13] M. G. Aartsen, R. Abbasi, M. Ackermann, et al. "Probing the origin of cosmic rays with extremely high energy neutrinos using the IceCube Observatory". In: *Phys. Rev. D* 88 (11 Dec. 2013), p. 112008. DOI: 10.1103/PhysRevD.88.112008. URL: https://link.aps.org/doi/10.1103/PhysRevD.88.112008.

[14] C. Spiering. "Towards High-Energy Neutrino Astronomy". In: *The European Physical Journal H* 37 (25 July 2012), pp. 515–565.

[15] T. M. Venters et al. "Energetic Particles of Cosmic Accelerators I: Galactic Accelerators". In: (Mar. 2019). arXiv: 1903.04634 [astro-ph.HE].

[16] T. M. Venters and et al. *Energetic Particles of Cosmic Accelerators I: Galactic Accelerators*. 2019. arXiv: 1903.04634 [astro-ph.HE].

[17] M. Spurio. *Particles and Astrophysics: A Multi-Messenger Approach*. Springer International Publishing, 2015.

[18] *Learn About IceCube Neutrinos*. URL: https://masterclass.icecube.wisc.edu/en/learn/learn-about-neutrinos.

[19] M. Aartsen et al. "IceCube-Gen2: A Vision for the Future of Neutrino Astronomy in Antarctica". In: (Dec. 2014). arXiv: 1412.5106 [astro-ph.HE].

[20] M. Aartsen et al. "First observation of PeV-energy neutrinos with IceCube". In: *Phys. Rev. Lett.* 111 (2013), p. 021103. DOI: 10.1103/PhysRevLett.111.021103. arXiv: 1304.5356 [astro-ph.HE].

[21] M. Aartsen et al. "Neutrino emission from the direction of the blazar TXS 0506+056 prior to the IceCube-170922A alert". In: *Science* 361.6398 (2018), pp. 147–151. DOI: 10.1126/science.aat2890. arXiv: 1807.08794 [astro-ph.HE].

[22] E. Resconi. *PLEvM - TOWARDS A PLANETARY NEUTRINO MONITORING SYSTEM*. Oct. 2019. DOI: 10.5281/zenodo.3520454. URL: https://doi.org/10.5281/zenodo.3520454.

[23] S. Adrian-Martinez et al. "Letter of intent for KM3NeT 2.0". In: *J. Phys. G* 43.8 (2016), p. 084001. DOI: 10.1088/0954-3899/43/8/084001. arXiv: 1601.07459 [astro-ph.IM].

[24] V. A. et al. "The prototype string for the km3-scale Baikal neutrino telescope". In: *Nuclear Instruments and Methods in Physics Research Section A: Accelerators, Spectrometers, Detectors and Associated Equipment* 602.1 (2009), pp. 227–234. ISSN: 0168-9002. DOI: https://doi.org/10.1016/j.nima.2008.12.149.

[25] *Ocean Networks Canada, Cascadia Basin*. Aug. 2020. URL: https://www.oceannetworks.ca/observatories/pacific/cascadia-basin.

[26] M. Agostini et al. “The Pacific Ocean Neutrino Experiment”. In: (May 2020). arXiv: 2005.09493 [astro-ph.HE].

[27] S. H. Haddock, M. A. Moline, and J. F. Case. “Bioluminescence in the Sea”. In: *Annual Review of Marine Science* 2.1 (2010). PMID: 21141672, pp. 443–493. DOI: 10.1146/annurev-marine-120308-081028. eprint: https://doi.org/10.1146/annurev-marine-120308-081028. URL: https://doi.org/10.1146/annurev-marine-120308-081028.

[28] I. Priede, A. Jamieson, A. Heger, J. Craig, and A. Zuur. “The potential influence of bioluminescence from marine animals on a deep-sea underwater neutrino telescope array in the Mediterranean Sea”. In: *Deep Sea Research Part I: Oceanographic Research Papers* 55 (Nov. 2008), pp. 1474–1483. DOI: 10.1016/j.dsr.2008.07.001.

[29] J. Bedard et al. “STRAW (STRings for Absorption length in Water): pathfinder for a neutrino telescope in the deep Pacific Ocean”. In: *JINST* 14.02 (2019), P02013. DOI: 10.1088/1748-0221/14/02/P02013. arXiv: 1810.13265 [astro-ph.IM].

[30] F. Henningsen. “Optical Characterization of the Deep Pacific Ocean: Development of an Optical Sensor Array for a Future Neutrino Telescope”. MA thesis. Munich, Tech. U., 2019-07-19. URL: https://www.cosmic-particles.ph.tum.de/fileadmin/w00bkl/www/Thesis/Master_Thesis_compressed.pdf.

[31] E. Resconi, K. Krings, and K. K. M. Rongen. “The Precision Optical CAlibration Module for IceCube-Gen2: First Prototype”. In: *PoS* ICRC2017 (2018), p. 934. DOI: 10.22323/1.301.0934.

[32] B. Lubsandorzhiev and Y. Vyatchin. “Studies of 'Kapustinsky's' light pulser timing characteristics”. In: *JINST* 1 (2006), T06001. DOI: 10.1088/1748-0221/1/06/T06001. arXiv: physics/0410281.

[33] M. Boehmer and et al. “STRAW (STRings for Absorption length in Water): pathfinder for a neutrino telescope in the deep Pacific Ocean”. In: *Journal of Instrumentation* 14.02 (2019). DOI: 10.1088/1748-0221/14/02/p02013.

[34] C. Fruck. “STRAW- attenuation length”. In: with support of Ocean Networks Canada and the The University of Alberta. Apr. 2020.

[35] R. C. Smith and K. S. Baker. “Optical properties of the clearest natural waters (200–800 nm)”. In: *Appl. Opt.* 20.2 (Jan. 1981), pp. 177–184. DOI: 10.1364/AO.20.000177.

[36] C. Fruck. “The Galactic Center resolved with MAGIC and a new technique for Atmospheric Calibration”. PhD thesis. Max-Planck-Institut of Physik, 2015.

[37] J. Babson et al. “Cosmic ray muons in the deep ocean”. In: *Nucl. Phys. B Proc. Suppl.* 14A (1990), pp. 157–161. DOI: 10.1016/0920-5632(90)90413-O.

[38] A. N. et al. “A comparison of photon detection efficiency and optical crosstalk of various SiPM devices”. In: (Feb. 2019).

[39] O. Girard, G. Haefeli, A. Kuonen, L. Pescatore, O. Schneider, and M. E. Stramaglia. *Characterisation of silicon photomultipliers based on statistical analysis of pulse-shape and time distributions*. 2018. arXiv: 1808.05775 [physics.ins-det].

[40] P. D. B. R.K. Pathria. "Statistical Mechanics," in: 3rd Edition. Elsevier Ltd., 2011. Chap. Ideal Fermi Systems.

[41] J. Kalisz. "Review of methods for time interval measurements with picosecond resolution". In: *Metrologia* 41.1 (2004).

[42] *The Go4 Project page*. Oct. 2019. URL: `https://www.gsi.de/en/work/research/experiment_electronics/data_processing/data_analysis/the_go4_home_page.htm`.

[43] *INTRODUCTION TO HDF5*. URL: `https://portal.hdfgroup.org/display/HDF5/Introduction+to+HDF5`.

[44] G. Korcyl, L. Maier, J. Michel, A. Neiser, M. Palka, M. Penschuck, P. Strzempek, M. Traxler, and C. Ugur. *A Users Guide to the TRB3 and FPGA-TDC Based Platforms*. Tech. rep. Darmstadt: GSI Helmholtzzentrum, Aug. 2020.

[45] H. Bradner, E. Hazen, and et al. "Attenuation of light in clear deep ocean water". In: *Geology* (1992).

[46] M. I. Latz, T. M. Frank, and J. F. Case. "Spectral composition of bioluminescence of epipelagic organisms from the Sargasso Sea". In: *Marine Biology* 98.3 (1988), pp. 441–446. DOI: `10.1007/BF00391120`. URL: `https://doi.org/10.1007/BF00391120`.

[47] S. Dong, G. Karniadakes, and N. Karonis. "Cross-Site Computations on the TeraGrid". In: *Computing in Science and Engineering* 7 (Oct. 2005), pp. 14–23. DOI: `10.1109/MCSE.2005.92`.

[48] J. H. LIENHARD. *Synopsis of lift, drag, and vortex frequency data for rigid circular cylinders.* Pullman, Wash. : Technical Extension Service, Washington State University, 1966., 1966.